Investigation of Vibrating-Hydrogen Based Ultrashort Molecular Phase Modulator

Andrea Schiavi
University College, Oxford

Submitted for the degree of Doctor of Philosophy
Michelmas Term 2015

Supervised by
Prof. Ian A. Walmsley
Dr. Adam S. Wyatt

Clarendon Laboratory
University of Oxford
United Kingdom

Investigation of Vibrating-Hydrogen Based Ultrashort Molecular Phase Modulator

Andrea Schiavi
University College, Oxford

Submitted for the degree of Doctor of Philosophy
Michelmas Term 2015

Abstract

This thesis investigates the coherent phase modulation of ultrashort pulses using vibrating hydrogen as a molecular medium.

Self-phase modulation in a gas-filled hollow core capillary allows the generation of high-power few-cycle pulses in the NIR. Such pulses can be used to drive high harmonic generation (HHG) to deliver attosecond duration pulses in the extreme ultraviolet and soft X-ray spectral region. While reaching unrivalled pulse durations (down to 67 as), these sources have characteristically low efficiencies. The pump-probe spectroscopy community would greatly benefit from brighter short wavelength sources with sub-5 fs duration.

In this work I apply Amplified RamaN Impulsive Excitation for Molecular Phase Modulation (ARNIEMPM), a multiple pulse scheme, to coherently prepare vibrating hydrogen molecules and exploit them for the phase modulation of ultrashort pulses. The preparation of the molecular motion is performed via impulsive stimulated Raman scattering and transient stimulated Raman scattering. The generated in-phase motion of molecules creates an oscillating optical polarizability in the medium which can be exploited by a probe pulse propagating through it, acting as a $125THz$ frequency phase modulator, the fastest among molecular media. This technique has the potential to provide bright, isolated sub-femtosecond duration ultra-violet (UV) pulses via spectral broadening of broadband pulses. I experimentally investigate the preparation of the molecular motion against multiple experimental parameters. I then demonstrate the molecular phase modulation of ultrashort broadband probes in the near-infrared (NIR) and UV via a degenerate interferometric scheme. I used a waveguide to increase the interaction length of the process and reduce the energy requirements for the medium preparation. This allowed the use of a single laser system to generate all the required pulses, which are largely diverse in terms of wavelength, duration and power.

Additionally, I present a novel technique named Attosecond Resolved Interferometric Electric-field Sampling (ARIES), which is capable of directly measuring the waveform of arbitrary pulses with attosecond resolution. This technique is based on high-harmonic generation (HHG) acting as a temporal gate for an applied secondary field, and tracking its electric field amplitude as a shift in the HHG cut-off frequency. I present experimental demonstration of a pulse waveform measurement by accurately retrieving a know inserted variation in dispersion and carrier-envelope-phase. A theoretical calculation of the technique applicability over a wide spectral range is also presented.

To my family

Acknowledgements

Firstly I would like to thank Prof. Ian A. Walmsley and Dr. Adam S. Wyatt for their constant supervision and friendship over these long years, which proved full of interesting research challenges and fun moments. I would also like to thank Prof. Marangos and Prof. Tisch from Imperial College, together with Dr. Dane Austin and Dr. Tobias Witting for the time I spent collaborating with them, from which I learned a lot. Thanks in particular for all their support in helping with my recalcitrant hollow.core fibre system. In this regard, I would like to acknowledge Dr. Pete Moseley for very kindly providing me with a constant stream of new hollow-core fibre capillaries, which I seemed to have the ability to damage in multiple and creative ways. Special thanks to Dr. Philip Bustard, whose work formed the basis of my thesis research. Thanks to him for the knowledge and expertise I was able to gain from him during our few months of collaboration at the start of my DPhil and for the support and extremely useful insight on the ARNIEMPM and its subtleties.

I would like to thank the whole Ultrafast group (the many generations I was lucky to meet) for being wonderful people and a constant source of motivation and friendly support during my rants about the laser/lab/neverending DPhil/rowing/*insert anything*. Having such a diverse and interesting group to work with was a real pleasure and taught me a lot beyond the purely academical level. I met some very good friends that I will never forget. I would like to thank in particular Dr. Marco Barbieri and Dr. Patrick Anderson for pushing me through the line over the last two years and in particular during the preparation of this thesis, providing invaluable help and support without which I would still be stuck in the lab. Thanks to the whole West Side crew: Matthias, Ilaria, Patrick, Brian, Michal, Christoph, Merlin, Alex and especially Laura for their friendship the fun times. You all made it much more enjoyable.

And thanks obviously to UCBC and Univ, which have been my second family (and absorbed all my spare time for four long, cold and wet years of rowing and suffering... but it was worth it). You may have to stop joking about me being still around... I'll miss you all. Thanks to the Animal House, one of the best years in my life, and the whole MD crew. 'nuff said.

And finally, thanks to my parents and the rest of my family, for the constant help and support and for resisting to the urge to kill me during this last months of stress and panic. Thanks, really. If this thesis exists it's because you made it possible.

Author's publications

Journal publications

1. A. Schiavi, P. Anderson, M. Barbieri, A. S. Wyatt, and I. A. Walmsley. "**Impulsive Raman phase modulation of ultrashort pulses in vibrating hydrogen**" *In preparation*, (2016).
2. A. S. Wyatt, T. Witting, A. Schiavi, D. Fabris, P. Matia-Hernando, I. A. Walmsley, J. P. Marangos, and J. W. G. Tisch. "**Attosecond sampling of arbitrary waveform**" *Optica - Submitted*, (2015).
3. O. Raz, O. Schwartz, D. Austin, A. S. Wyatt, A. Schiavi, O. Smirnova, B. Nadler, I. A. Walmsley, D. Oron, and N. Dudovich. "**Vectorial phase retrieval for linear characterization of attosecond pulses**" *Physical Review Letters*, **13**, 107 (2010).

List of abbreviations

Abbreviation	**Description**
ARIES	Attosecond Resolved Interferometric Electric-field Sampling
ARNIEMPM	Amplified RamaN Impulsive Excitation for Molecular Phase Modulation
AS1	anti-Stokes 1
BBO	β-barium borate
BS	beam splitter
CCD	charged coupled device
CEO	carrier envelope offset
CEP	carrier envelope phase
CMOS	complementary metaloxidesemiconductor
CPA	chirped pulse amplification
CW	continuous wave
FROG	frequency-resolved optical gating
FTL	Fourier-transform limited
FWHM	full width half maximum
GD	group dispersion
GDD	group delay dispersion
GV	group velocity
GVD	group velocity dispersion
HCF	hollow-core fibre

Abbreviation	**Description**
HHG	high harmonic generation
HWHM	half width half maximum
ISRS	impulsive stimulated Raman scattering
IWE	inhomogeneous wave equation
MPM	molecular phase modulation
ND	neutral density
NIR	near infrared
PID	proportional-integral-derivative
RWE	reduced wave equation
S1	Stokes 1
SEA-	spatially encoded arrangement
SFA	strong field approximation
SFG	sum frequency generation
SHG	second harmonic generation
SNR	signal to noise ratio
SPIDER	spectral phase interferometry for direct electric-field reconstruction
SRS	stimulated Raman scattering
TDSE	time-dependent Schrödinger equation
Ti:Sapph	titanium sapphire
UV	ultraviolet
VIS	visible
XUV	extreme ultraviolet

Contents

List of Figures

List of Tables

Chapter 1

Introduction

The development of the laser by Maiman in 1960[1] enabled the investigation of the properties of matter by delivering well controlled amounts of energy to very specific locations in the form of coherent monochromatic light beams. Laser technology has been advancing ever since, refining and extending the capability to generate laser probes to investigate an ever expanding range of physical phenomena. A fundamental milestone was achieved with the development of pulsed lasers, which enable the study of dynamical systems in their natural time scale. The advent of mode-locking[2,3] in particular allowed the generation of femtosecond-duration laser pulses. Such experiments are typically performed in a pump-probe configuration, where a dynamical system is driven by a pump (usually a laser pulse) and then probed by a short pulse after a certain time. Varying the time delay allows a *movie* to be reconstructed of the dynamics induced by the pump, and how the systems returns to equilibrium. The duration of the probe pulse defines the time gate, and hence the resolution, at which the dynamical process that can be studied. Many ultrafast physical processes occurring at a molecular level were discovered by the use of such techniques, giving birth to the field of femto-chemistry[4].

The push for a shorter laser probes, and thus shorter temporal resolution for the study of material dynamics, reached another milestone when it was demonstrated that self-phase modulation (SPM) in a gas-filled hollow core capillary allows the generation of high-power few-cycle (sub-5 fs) pulses in the near-infrared (NIR)[5,6]. This technique's relative ease of implementation made it the mainstay approach for the generation of such pulses and the ultrafast dynamical processes that could be accessed within this energy and duration range.

The shortest pulse duration achievable is limited by the central wavelength of the pulse, as theory requires the pulse to contain at least one full oscillation of the electric field. For 800 nm this is equivalent to approximatively 2.67 fs. It is thus necessary to move to shorter wavelengths to obtain pulses with a shorter duration.

Several approaches to the generation of few-cycle pulses in the UV, such as self-compression through filamentation[7] and cross-phase modulation in a gas filled hollow-core capillary between a broadband NIR pulse and a UV source[8], managed to provide UV pulses in the 5 fs regime, but a massive step forward was achieved with the generation of attosecond pulses via high harmonic generation (HHG).

This approach exploits the aforementioned SPM-based compression technique in a hollow-core capillary as a driving field to generate extremely broad spectra of isolated harmonics of the input spectrum and deliver laser probes as short as 67 as[9]. The generated sidebands reach energies up to the extreme ultra-violet (XUV) and soft X-ray region of the electromagnetic spectrum[10–12]. Impressive results have been achieved when investigating electronic dynamics with attosecond resolution, revitalizing the field of atomic physics by the development of new theoretical and experimental approaches. An exquisite example of this is the real-time study of electron tunneling in Ne atoms[13]. Molecular and solid-state dynamics have been studied in this novel temporal regime, often triggering an intense theoretical activity following the experimental results.

The temporal durations achievable through HHG are still unrivalled, as generating bandwidths large enough (several hundreds of THz) to support such pulse durations is rather challenging. These sources do however have issues which limit their usefulness as efficient probes. The most limiting of these is their low energy, due to the inefficiency of the HHG process ($< 10^{-6}$). The weakness of these sources limits the range of processes that can be studied with a pump-probe approach, while their very broad spectrum limits the accessible energy range to the XUV, which is not ideal for the study of many electronic resonances in molecular media. A second limiting factor is the lack of many types of optics in the XUV/soft X-ray wavelength range, which puts tight constraints on the experimental schemes that can be exploited. In particular, nonlinear media in this regime are still unavailable at this day, while even simple reflection of XUV light requires a very narrow angle of incidence and/or carefully engineered multi-layer optics.

The field of pump-probe spectroscopy would greatly benefit from the availability of brighter sources in the few-fs and attosecond regime. In particular, the UV range is lacking an equivalent to the SPM-based compressors available to the NIR to access isolated, bright pulses with few-cycle durations ($0.5 - 4\,\mathrm{fs}$ range). I will refer to these as UV few-cycle pulses throughout this chapter. Few-cycle pulses in the UV could also provide better probes as they will possess a larger cross-section than the XUV light generated via HHG in accessing electron dynamics. The availability of pulses with these specifications would enable experimental studies of molecular dynamics which access electronic resonances directly. This wavelength regime will also overcome the second problem associated with HHG as optics are more widely available.

In this framework, molecular phase modulation, based on Raman scattering, has the potential to fill the gap between the available 5 fs UV laser probes and XUV sources obtained via HHG. Initially regarded as a competitor to HHG towards the synthesis of the first attosecond duration pulse, this technique is now considered a strong candidate for the delivery of bright, isolated, UV few-cycle pulses. This technique could also overcome the limitations of HHG-based sources, thus providing a very powerful tool to the ultrafast laser community.[14]

1.1 The role of Raman scattering phase modulators

Within the quest for bright UV few-cycle pulse, approaches based on Raman scattering[15,16] have been under development for several years and are showing promising results. The Raman effect is an inelastic two-photon scattering process where the difference in input and scattered photon energy corresponds to a molecular transition. For historical reasons, red-shifted photons are termed Stokes (S) photons, while blue-shifted ones are anti-Stokes (AS) photons. The process can cascade, and such techniques aim at obtaining sufficient bandwidths to support UV few-cycle pulses by coherently stimulating sidebands over a broad range of frequencies, where each component is separated by the molecular energy level spacing.

Raman-based techniques possess the following advantages with respect to HHG-based sources[14]:

- an operating wavelength range spanning from UV to NIR, with the capability of synthetizing fields covering this entire range;
- the potential to generate bright pulses as the efficiency is orders of magnitude higher than that of HHG;
- pulse trains with sub-fs duration can be obtained by controlling the phase of the individual spectral components generated;
- isolated sub-fs pulses can be obtained by using initial pulses with a large enough bandwidth to overlap with the generated sidebands, creating a continuous spectrum.

The preparation of a coherent molecular excitation can lead to a time dependent refractive index which oscillates with the molecular motion and can be exploited for the phase modulation of ultrashort pulses at very high frequencies ($\sim 100\,\mathrm{THz}$). Experimental realization of this preparation can happen in various configurations, ranging from purely impulsive[17] to the fully adiabatic regime[18]. These opposing approaches have realized impressive results, but thus far have failed to achieve all the elements necessary to generate few-cycle UV pulses.

Hybrid approaches have shown a huge potential, combining the strengths of these multiple concepts and overcoming the respective limitations, making this an ideal candidate to achieve the goal of bright, isolated, few-cycle UV pulses.

1.2 The ARNIEMPM approach

Amplification of RamaN Impulsive Excitation for Molecular Phase Modulation (ARNIEMPM), introduced by Bustard[19], demonstrated the ability to coherently prepare a molecular medium in a rotational superposition and utilize this to phase modulate an ultrashort pulse, resulting in the generation of coherent sidebands overlapping with the original spectrum.

In this thesis I will present the research work I performed investigating vibrating hydrogen-based phase modulators prepared using the ARNIEMPM technique as a possible source of bright, isolated, UV few-cycle pulses.

ARNIEMPM is a three-pulse approach that simultaneously exploits the strength of impulsive and adiabatic schemes to obtain coherent preparation of the material.

Two fundamental concepts are used: stimulated Raman scattering (SRS)[20] and impulsively stimulated Raman scattering (ISRS). In SRS the presence of Stokes photons stimulates the otherwise spontaneous Raman scattering process, so that the phases of the emitted photons are not randomly initiated by quantum mechanical zero-point effects[21] but defined by the phase of the incident fields. The role of the initial Stokes photons can be played by anti-Stokes photons or even molecular phonons, resulting in the same effect. Stokes SRS is usually preferred due to its higher efficiency, which is a function of the initial population of the molecular states. ISRS refers to the use of broadband pulses with a duration comparable to the molecular motion period, such that $\Delta t \sim 2\pi/\Omega$, where $\hbar\Omega$ is the energy separation of the molecular levels. The pulse contains both the pump and Stokes fields for the Raman transition as its spectrum spans the molecular energy gap. The phase of the material excitation is therefore set by the phase of the input pulse. The pulse's short duration results in an impulsive kick to the molecules, which are left in long-lived (*ns* duration) coherent superposition state of their ro-vibrational levels, as they cannot respond fast enough to the applied field.

Figure 1.1 illustrates the ARNIEMPM concept by showing a schematic of the effect each of the three pulses has on the molecular system. First, a weak impulsive seed pulse initiates the molecular motion, locking the phase of the stimulated molecular motion to the laser via ISRS and creating an initial coherence among the molecular levels. A second longer and more powerful pulse amplifies the existing coherent motion via SRS from the already present molecular phonon excitation, transferring more population to the excited level and increasing the molecular coherence. The coherence prepared by these two steps creates a temporally oscillating refracting index in the material at the period of the molecular motion, which is in phase with the initial seed pulse. A third impulsive probe pulse, coherent with the seed (derived from the same source to maintain the phase relation with the material) travels through the molecular medium and experiences phase modulation, causing the stimulation of Raman sidebands which are coherent with the probe pulse, leading to spectral broadening. I will commonly refer to these three pulses respectively as the "seed", "pump" and "probe" throughout this thesis.

I decided to investigate the feasibility of this approach using vibrating hydrogen as it provides the fastest molecular modulator available, with a motion period of 8 fs. The corresponding 125 THz frequency shift provides dramatic spectral broadening making this a logical choice of medium.

As was demonstrated in the first implementation of ARNIEMPM[19] the pump can be

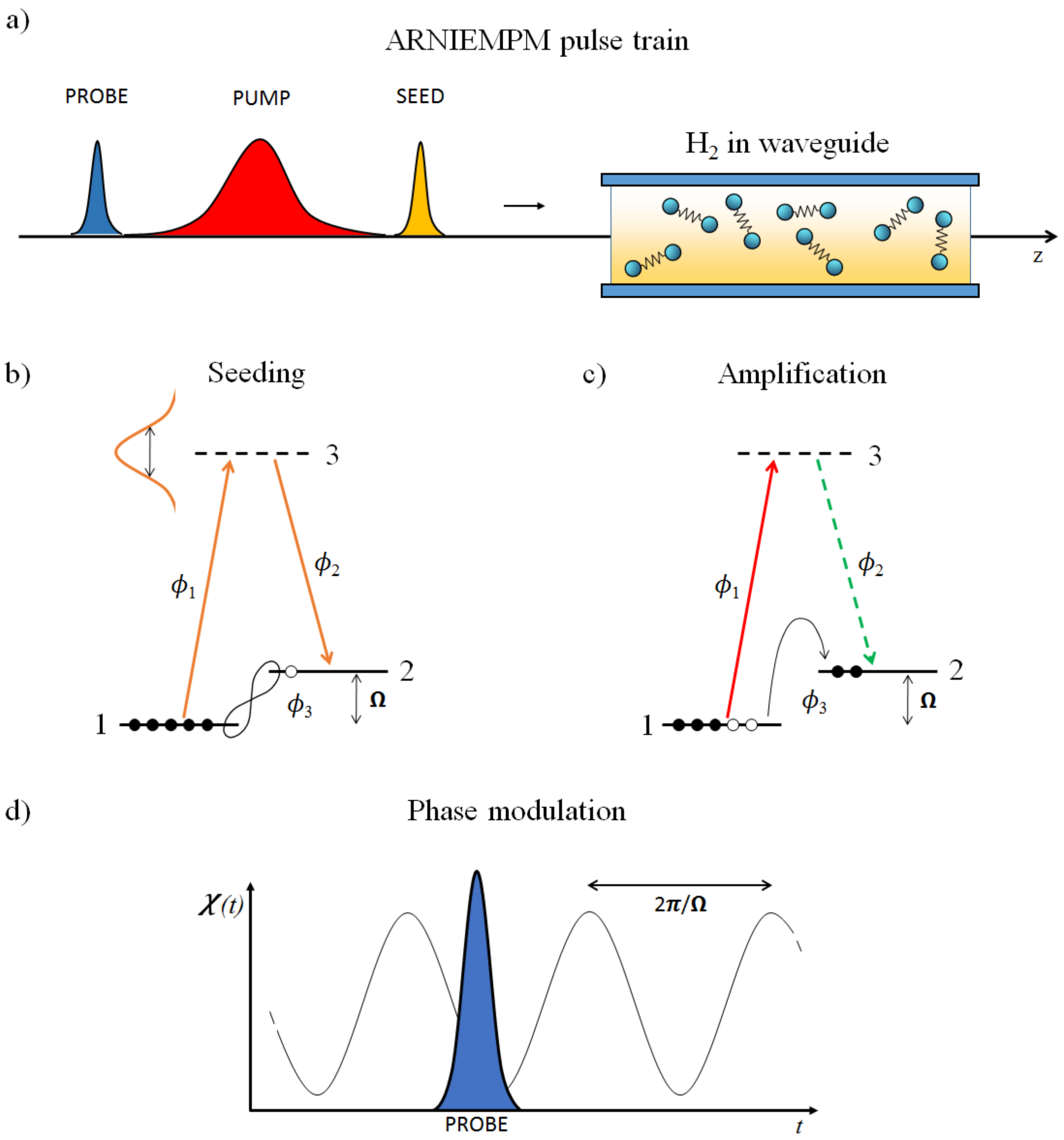

Figure 1.1: ARNIEMPM concept: a) the seed, pulse, and probe pulses propagate through a hydrogen-filled hollow-core waveguide in this order. **b)** the seed pulse possess a bandwidth large enough to span the molecular energy shift; it commences the coherence ISRS. Both the pump and Stokes fields in the transition belong to the same laser, thus the phase ϕ_3 of the excitation is fixed and not randomly initiated. **c)** the longer and more energetic pump pulse transfers population to the excited level by transient SRS thanks to the already present molecular phonons. The phase of the excitation is maintained coherent with the seed pulse. **d)** the coherence prepared by seed and pump causes the refractive index to oscillate in time with a period equal to that of the molecular motion. This results in phase modulation of a UV probe and spectral broadening via the coherent sideband generation.

derived from an independent source, as the phase of the molecular motion is defined by the seed pulse only. This makes it possible to use powerful long pulse lasers to achieve a high degree of amplification. Considering the power-scaling of ultrafast Ti:Sapph-based sources in recent years, I decided to utilize a single commercial laser source (a chirped-pulse amplifier with an output energy up to 3 mJ) to synthetize all three pulses. This has the advantage of reducing the resources required to implement ARNIEMPM effectively, but does have the disadvantage of limiting the overall available power.

As a solution to this I decided to develop a waveguide geometry to increase the interaction length by a factor of ~ 10 with respect to Bustard's work. Here, the three pulses required for ARNIEMPM propagate in a hydrogen-filled hollow-core capillary of length 1 m. As it will be shown in chapter 2 the Raman gain of the process depends linearly on the length of the interaction, thus the waveguide contribution will mitigate the power limitation and allow the probe phase modulation to occur within the experimentally available parameter space.

1.3 The ARIES pulse measurement technique

Developing the most suitable light sources to access ultrafast dynamics relies heavily on the ability to fully characterize them before and after their interaction with a dynamic system. The constant requirement for shorter pulses has recently been matched by the need for complex waveforms to optimize nonlinear processes, achieve coherent control over dynamical processes and investigate the dynamics of complex systems. An emblematic example is research that focusses on increasing the efficiency of the HHG process[22–24]. A theoretical work presented by Chipperfield *et al.*[25] indicated how a pulse consisting of an electric field with a linear ramp and an abrupt switch off (commonly known as the “perfect wave”) may be used to increase the HHG efficiency manifold.

Commonly used indirect characterization techniques rely on the measurement of spectral intensity and phase to reconstruct the temporal structure of the pulse, but the synthesis of complex waveforms requires extremely large bandwidths and features which cause these techniques to fail. In this thesis I present the work performed in collaboration with Imperial College to experimentally test a novel collinear interferometric technique based on HHG gating, capable of directly measuring the electric field of any pulse with attosecond resolution within a broad range of frequencies, directly overcoming the problems encountered by most of the existing approaches. Such a technique is perfectly suited to characterizing the output of Raman based frequency modulators similar to the one presented in this thesis, which can exhibit very large bandwidths, large spectral gaps and waveforms with a high degree of complexity[26].

1.4 Organization of the thesis

Chapter 2 illustrates the theoretical derivation of the ARNIEMPM approach, providing the basic notation and tools necessary to understand the laser-matter interaction via Raman scattering. This model relies on a semi-classical approach, utilizing Von Neumann’s density matrix notation to quantum mechanically represent the evolution of the molecular system and the inhomogeneous wave equation to account for the classical field propagation.

Chapter 3 presents the full experimental system design, detailing the different elements of the complex laser chain utilized to derive the required laser probes and the capillary-based Raman interaction cell. The layout of the optical systems employed in the measurements will be presented, together with the necessary diagnostic and characterization tools.

Chapter 4 illustrates the experimental investigation of the effect of the seed and pump on the coherence preparation. The effective impulsive seeding and amplification is tested against various parameters, such as the pulse delays, pump power and the seed bandwidth. The pump output spectrum, containing the fundamental spectrum and the generated Raman sidebands is used as the main diagnostic to assess the degree of vibrational coherence preparation.

Chapter 5 presents the experimental results of the ARNIEMPM approach with broadband probe pulses centred at 800 nm and 400 nm. A degenerate detection technique is presented, which exploits a chirped probe pulse to enhance the detection of vibrational phase modulation.

Chapter 6 introduces a novel technique based on HHG which allows the direct measurement of arbitrary optical waveforms with attosecond resolution. A theoretical introduction to HHG and the mechanism's underlying technique is presented, together with experimental and numerical results demonstrating the capabilities of this approach.

Chapter 7 concludes the thesis with a summary of what has been achieved and what future developments might be.

Chapter 2

Theoretical description of ARNIEMPM

In this chapter I present the semi-classical model used to describe the basic principle of ARNIEMPM. The Raman interaction between light and matter is derived from the molecular polarizability model in the case of off-resonant fields. The interaction representation is used to identify a Raman interaction Hamiltonian and the Von Neumann density matrix formalism is used to derive the dynamic evolution of the generated coherence. The interaction between the individual pulses (seed, pump and probe) and the molecular medium is calculated via the evolution of a generalized Raman interaction density matrix for a specific set of pulse parameters with respect to the molecular response, providing a more rigorous description of ARNIEMPM.

2.1 Basic theoretical definitions

In this section I will present the basic framework and notation used to define electromagnetic fields. Maxwell's theory forms the basis of the general understanding of electromagnetism and optical phenomena. From Maxwell equations the wave equation is derived, which governs the propagation of electromagnetic fields and plays a pivotal role in understanding the Raman interaction between light and matter.

2.1.1 The inhomogeneous wave equation

Maxwell's equations in differential form appear as:

$$\nabla \cdot \boldsymbol{D} = \rho \tag{2.1}$$

$$\nabla \cdot \boldsymbol{H} = 0 \tag{2.2}$$

$$\nabla \times \boldsymbol{E} = -\partial_t \boldsymbol{B} \tag{2.3}$$

$$\nabla \times \boldsymbol{H} = \boldsymbol{J} + \partial_t \boldsymbol{D}, \tag{2.4}$$

with $\boldsymbol{E}$ denoting the electric field, $\boldsymbol{B}$ the magnetic field, $\boldsymbol{H}$ the magnetic field strength and $\boldsymbol{D}$ the displacement field. ρ and $\boldsymbol{J}$ refer to the charge and current density respectively. ϵ_0 and μ_0 are the dielectric and magnetic permeability in free space. The bold notation denotes vectors and will be used throughout the thesis. The constitutive relations between the field quantities are defined as

$$\boldsymbol{D} = \epsilon_0 \boldsymbol{E} + \boldsymbol{P} \tag{2.5}$$

$$\boldsymbol{H} = \frac{\boldsymbol{B}}{\mu_0} - \boldsymbol{M} \tag{2.6}$$

where $\boldsymbol{M}$ is the magnetization and $\boldsymbol{P}$ the electric polarization density inside a material medium.

If we consider a pulse propagating in an isotropic medium with no free charges or currents such that $\rho = 0$, $\boldsymbol{J} = 0$ and we neglect magnetic effects so that $\boldsymbol{M} = 0$ (as in the molecular medium we want to model), one obtains

$$\nabla \times (\nabla \times \boldsymbol{E}) = -\mu_0 \epsilon_0 \partial_t^2 \boldsymbol{E} - \mu_0 \partial_t^2 \boldsymbol{P} \tag{2.7}$$

by taking the curl of 2.3, substituting 2.4 differentiated with respect to time. Using the vector identities $\nabla \times (\boldsymbol{A} \boldsymbol{\cdot} \boldsymbol{B}) = \boldsymbol{A} \cdot (\nabla \times \boldsymbol{B}) + (\nabla \boldsymbol{A}) \times \boldsymbol{B}$ and $\nabla \times (\nabla \times \boldsymbol{A}) = \nabla(\nabla \cdot \boldsymbol{A}) - \nabla^2 \boldsymbol{A}$ and inserting 2.1 one obtains

$$\left[\nabla^2 - \frac{1}{c^2}\right] \boldsymbol{E} = \mu_0 \partial_t^2 \boldsymbol{P}, \tag{2.8}$$

where c is the speed of light in vacuum. This is the inhomogeneous wave equation (IWE) and governs the propagation of an electric field in a dielectric medium. The polarization term on the right can act as an electric field source when oscillating.

In the case of propagation in vacuum, 2.8 becomes known as the homogeneous wave equation, with $\boldsymbol{P} = 0$. Solutions of the wave equation in this case are plane waves of the form

$$\boldsymbol{E} = \boldsymbol{E_0} \cos\left[\boldsymbol{k} \cdot \boldsymbol{r} \pm \omega t + \tilde{\phi}(\omega, \boldsymbol{k})\right], \tag{2.9}$$

where ω denotes the angular frequency; $\boldsymbol{k} = k_x \hat{\boldsymbol{x}} + k_y \hat{\boldsymbol{y}} + k_z \hat{\boldsymbol{z}}$ is the wave vector; $\boldsymbol{r} = (x, y, z)$ is the position vector; and $\tilde{\phi}(\omega, \boldsymbol{k})$ is the phase angle. From 2.8 and 2.9 the dispersion relation in vacuum is obtained as $\omega = ck$, where $k = |\boldsymbol{k}|$.

2.1.2 Analytic electric field

The electric field $\boldsymbol{E}(\boldsymbol{r},t)$ is linked to its complex spectrum $\tilde{\boldsymbol{E}}(\boldsymbol{r},\omega)$ via Fourier transform through the definitions

$$\boldsymbol{E}(\boldsymbol{r},t) = \int_{-\infty}^{\infty} \tilde{\boldsymbol{E}}(\boldsymbol{r},\omega) e^{-i\omega t} \frac{d\omega}{2\pi} \tag{2.10}$$

$$\tilde{\boldsymbol{E}}(\boldsymbol{r},\omega) = \int_{-\infty}^{\infty} \boldsymbol{E}(\boldsymbol{r},t) e^{i\omega t} dt. \tag{2.11}$$

The spectrum positive and negative frequency components must follow the relation $\tilde{\boldsymbol{E}}(\boldsymbol{r},\omega) = \tilde{\boldsymbol{E}}^*(\boldsymbol{r},-\omega)$, as the electric field $\boldsymbol{E}(\boldsymbol{r},t)$ is real. The spectrum can then be conveniently divided in two functions such that $\tilde{\boldsymbol{E}}(\boldsymbol{r},\omega) = \tilde{\boldsymbol{E}}^+(\boldsymbol{r},\omega) + \tilde{\boldsymbol{E}}^-(\boldsymbol{r},\omega)$, defined as

$$\tilde{\boldsymbol{E}}^+(\boldsymbol{r},\omega) = \begin{cases} \tilde{\boldsymbol{E}}(\boldsymbol{r},\omega) & \text{for}\,\omega \geq 0 \\ \\ 0 & \text{for}\,\omega < 0 \end{cases} \tag{2.12}$$

$$\tilde{\boldsymbol{E}}^-(\boldsymbol{r},\omega) = \begin{cases} 0 & \text{for}\,\omega \geq 0 \\ \\ \tilde{\boldsymbol{E}}(\boldsymbol{r},\omega) & \text{for}\,\omega < 0 \end{cases} \tag{2.13}$$

From this we can define the analytic field as the Fourier transform of the positive part of the spectrum

$$\boldsymbol{E}^+(\boldsymbol{r},t) = \int_{-\infty}^{\infty} \frac{d\omega}{2\pi} \hat{\boldsymbol{E}}^+(\boldsymbol{r},\omega) e^{-i\omega t}, \tag{2.14}$$

and the real electric field as twice the real part of the analytical field

$$\boldsymbol{E}(\boldsymbol{r},t) = 2\mathcal{R}e\left[\boldsymbol{E}^+(\boldsymbol{r},t)\right]. \tag{2.15}$$

In general terms, the complex analytic field can be represented as a product between an amplitude function and a phase term:

$$\boldsymbol{E}^{+}(\boldsymbol{r},t) = \frac{1}{2}\tilde{\boldsymbol{A}}(\boldsymbol{r},t)e^{i\Gamma(t)}. \tag{2.16}$$

In most practical cases the spectrum will be centred around a mean frequency ω_0 and will present non-zero values in a defined frequency interval $\Delta\omega$ which is small compared to ω_0. In the time domain it is then convenient to introduce the carrier frequency ω_0 and write the analytical field as

$$\boldsymbol{E}^{+}(\boldsymbol{r},t) = \frac{1}{2}\boldsymbol{A}(\boldsymbol{r},t)e^{i(\phi(t)-\omega_0 t)}, \tag{2.17}$$

where $\boldsymbol{A}(\boldsymbol{r},t)$ is defined as the real field envelope (differently from $\tilde{\boldsymbol{A}}(\boldsymbol{r},t)$, which identifies the complex field envelope) and $\phi(t)$ is the time-dependent phase. The real field can then be written as

$$\boldsymbol{E}(\boldsymbol{r},t) = \frac{1}{2}\left(\boldsymbol{A}(\boldsymbol{r},t)e^{i(\phi(t)-\omega_0 t)} + \text{c.c.}\right). \tag{2.18}$$

which is the representation of a laser pulse in the time domain.

For the assumption of $\Delta\omega \ll \omega_0$ to hold, the temporal variation of the envelope $\boldsymbol{A}(\boldsymbol{r},t)$ and $\phi(t)$ must be small with respect to one optical cycle $T = 2\pi/\omega_0$, which for the complex envelope corresponds to

$$\left|\frac{d}{dt}\tilde{\boldsymbol{A}}(\boldsymbol{r},t)\right| \ll \omega_0 \left|\tilde{\boldsymbol{A}}(\boldsymbol{r},t)\right| \tag{2.19}$$

In this situation the pulse behaviour could be described by a slowly varying envelope and a phase, greatly simplifying the theoretical description of the pulse propagation and interaction with matter. The improtance of this condition among the pulse defining entities will become clear when the slowly-varying envelope approximation (SVEA) [27], is invoked later in this chapter to describe the pulse propagation.

It is useful to introduce here a different temporal coordinate system, called the "retarded" frame of reference, as:

$$\eta = t - \frac{z}{v_g} \tag{2.20}$$

where v_g is the pulse group velocity, which represents the pulse envelope propagation velocity (its expression will be introduced later in this chapter, when giving a detailed description of the pulse phase). This co-moving reference frame follows the pulse envelope and has a great practical usefulness: for example, in the case of a constant temporal phase $\phi(t)$, in this retarded reference frame the pulse envelope is unchanged in time.

2.1.3 Linear and nonlinear optics

As already stated, in the case of an electromagnetic field propagating in a dielectric medium the wave equation takes the inhomogeneous form (Equation 2.8), with a non-zero polarization term $\boldsymbol{P}$ which represents the response of the medium to the applied $\boldsymbol{E}$ field. The application of an electric field can induce oscillating dipole moments in the material, comprised of electrons moving with the applied oscillating field. The polarization term $\boldsymbol{P}$ is the sum of such moments. The strength of the electric dipole can be modelled as a harmonic oscillator by considering an electron moving in a binding potential. The atomic potential inside the medium can be represented via Taylor expansion whose order is dependent on the applied field strength. The resulting potential depends on the strength of the applied field: for small intensities, the potential is approximated as a harmonic function and thus the response is linear. For higher intensities, the potential is anharmonic and the polarization dependence of the applied field becomes nonlinear. The polarization too can be Taylor expanded as

$$\boldsymbol{P}(t) = \epsilon_0 \left(\chi^{(1)} \boldsymbol{E}(t) + \chi^{(2)} \boldsymbol{E}^2(t) + \chi^{(3)} \boldsymbol{E}^3(t) + ... \right), \tag{2.21}$$

where the coefficients $\chi^{(n)}$ are the nth order susceptibility terms of the medium. In the case of anisotropic media, the field and polarization response are not aligned and thus $\boldsymbol{\chi}$ is a tensor. For low optical intensities the polarization term $\boldsymbol{P}$ in the IWE is linear, allowing plane-wave solutions as in the free space case. These solutions take the same form as Equation 2.9 but with a modified dispersion relation, to account for the material:

$$k = \frac{n\omega}{c}, \tag{2.22}$$

where $k = |\boldsymbol{k}|$ and $n = \sqrt{1+\chi} = c/v$ is the refractive index of the material, describing the phase velocity v with respect to the speed of light in vacuum c. The refractive index (and susceptibility) is generally frequency dependent, giving rise to the well known chromatic dispersion.

In the case of higher intensities the polarization varies nonlinearly with the applied field strength and the IWE becomes nonlinear. Three different regimes of nonlinearity can be identified. These are defined by the incident electric field strength $|E_{in}|$ with respect to the atomic binding field E_{bind}.

For a linearly polarized electric field with limited intensity ($I \ll 10^{13}\mathrm{Wcm}^{-2}$) the nonlinear wave equation leads to the generation of low-order harmonics of the fundamental frequency, self-focusing and Raman scattering among many other phenomena. Nonlinear optics in this regime provides a range of tools that can be used to manipulate laser light: the work reported in this thesis, as will be explained in chapter 3, exploits three examples of nonlinear optical phenomena, namely self-phase modulation (SPM), second-harmonic generation (SHG) and stimulated Raman scattering (SRS) to provide diverse laser sources of various durations and wavelengths through the interaction with different nonlinear media. A detailed presentation of nonlinear optics in this regime and its rich phenomenology can be found in Boyd[28].

The second nonlinearity regime is reached when the applied field has a comparable intensity with the atomic binding field ($I \sim 10^{15}\mathrm{Wcm}^{-2}$). In this case over-the-barrier or tunnel ionization for outermost bound electrons is possible. The resulting dynamics take place in what is identified as the strong field regime, meaning that the electron dynamics are dominated by the applied field, which is strong enough to go beyond a simple perturbation of the atomic binding potential. An example of this is high-harmonic generation (HHG), which is commonly used to generate ultrashort bursts of radiation in the soft x-ray/XUV regime. A description of HHG basic concept and technique will be presented in chapter 6.

The third nonlinearity regime is achieved when the applied field intensity is extremely high ($I \gtrsim 10^{18}\mathrm{Wcm}^{-2}$). In this regime ionized electrons can achieve relativistic velocities when accelerated in the optical field. The resulting relativistic nonlinear optics requires a treatment which goes beyond the scope of this thesis.

2.1.4 Pulse phase

The concept of chromatic dispersion was mentioned in the previous section as a frequency dependence of the refractive index when considering an electric field propagating through a dielectric material. In this case a formula known as Sellemeier equation[29] is used to approximate the refractive index as a function of frequency. This formula contains various coefficients which are unique to the dispersive medium under consideration and allow calculation of the resulting chromatic dispersion. These are found empirically by fitting experimental data to the Sellmeier equation, but their validity is limited to particular spectral bands, due to atomic resonances, typically across the visible part of the spectrum.

The spectral phase acquired by a pulse propagating through a dispersive medium is calculated as the product of the frequency dependent wave vector $k(\omega)$ with the length of the material L, resulting in a chirped pulse, i.e. a variation of the instantaneous frequency over time and a temporal broadening.

The spectral phase can be expressed by a Taylor expansion around the central frequency ω_0 as

$$\begin{aligned} \tilde{\phi}(\omega) &= k(\omega)L && (2.23) \\ &= \frac{n(\omega)\omega}{c}L && (2.24) \\ &= \sum_{m=0}^{\infty} \frac{1}{m!}\tilde{\phi}^{(m)}(\omega_0)(\omega-\omega_0)^m, && (2.25) \end{aligned}$$

where $\tilde{\phi}^{(m)}(\omega_0)$ is the n-th derivative of the spectral phase evaluated at the central frequency ω_0. These coefficients are usually expressed in units of $[\mathrm{fs/rad}]^m$ for the angular frequency and in $[\mathrm{fs}]^m$ for the natural frequencies. Similarly, the temporal phase can be expanded as

$$\phi(t) = \sum_{m=0}^{\infty} \frac{1}{m!}\phi^{(m)}(t_0)(t-t_0)^m. \tag{2.26}$$

Here, t_0 represents the pulse position in time at a given instant, with respect to the laboratory frame. The optical phase accumulated at each frequency contains all the relevant information needed to calculate the reshaping of the pulse at any given location while propagating through a medium. A pulse with a flat phase is defined as a Fourier-transform limited (FTL) pulse and it exhibits the shortest temporal duration supported by a given bandwidth. It is useful to give a physical interpretation of some of the expansion coefficients for both the temporal and spectral case and their specific effect on the pulse in question. The first term $\tilde{\phi}^{(0)}(\omega_0)$ in Eq. 2.25 is the total phase accumulated by the reference frequency ω_0 and is related to the location of this frequency with respect to the envelope peak. The equivalent term in the time domain $\phi^{(0)}(t)$ is commonly known as carrier-envelope offset (CEO) or carrier-envelope phase (CEP) and it represents the location of the electric field maxima with respect to the temporal envelope peak (with $\phi^{(0)}(t) = 0$ when they coincide). This quantity becomes relevant in the case of few-cycle pulses, as depicted in figure 2.1, as a change in CEP can cause a variation in maximum intensity and then needs to taken into account (or compensated for via control loop systems) when the pulse is used in high-order nonlinear processes, where a small intensity fluctuation could cause significant changes of the experimental conditions. The second term of the expansion of the spectral phase is identified as the group delay (GD) $\tau_g \equiv \tilde{\phi}^{(1)}(\omega_0) = \frac{\partial\tilde{\phi}}{\partial\omega}\Big|_{\omega_0}$ and this represents the time taken by the pulse envelope centred at ω_0 to propagate through the material. From this

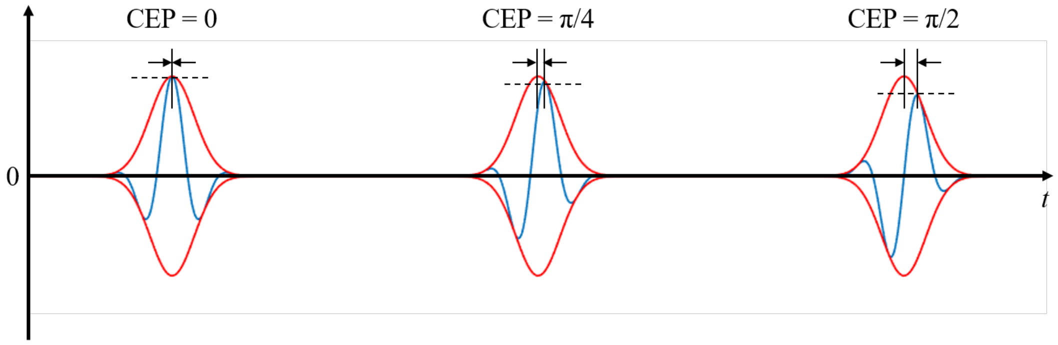

Figure 2.1: CEP effect on few-cycle pulses: field (blue) and envelope (red) of three few-cycle pulses with different CEP: 0, $\pi/4$ and $\pi/2$. The CEP variation, calculated in units of wavelength periods, causes the maximum intensity of the actual field (dashed line) to change with respect to the envelope maximum (top of red curves), reducing the pulse intensity. The left and right pulses usually termed "sine" and "cosine" pulse, respectively, and represent the maximum and minimum of the pulse intensity variation that can be induced by a variation in the pulse CEP.

the group velocity (GV) of the pulse $v_g(\omega)$ is

$$v_g(\omega) = \left(\frac{\partial k}{\partial \omega}\right)^{-1}, \tag{2.27}$$

so that, $\tau_g = L/v_g$. In the case of propagation through many materials the group velocity is frequency dependent, resulting in a frequency-dependent delay for each spectral component. This is known as group delay dispersion (GDD) and is quantified by the third term of the expansion 2.25

$$\tilde{\phi}^{(2)}(\omega_0) = \left.\frac{\partial^2 \tilde{\phi}(\omega)}{\partial \omega^2}\right|_{\omega_0} = \frac{\partial \tau_g}{\partial \omega}. \tag{2.28}$$

The macroscopic effect of the GDD is to temporally broaden the pulse and induce a sweep in the instantaneous frequency, considered in the pulse retarded reference frame, thus creating a chirped pulse. The sign of the GDD determines the direction in which frequencies are dispersed. A positive GDD is commonly known as normal dispersion and causes the higher frequencies to travel at a lower velocity, i.e. the leading edge (i.e. earlier time of arrival) of the pulse will present the ‘red’ end of the spectrum while the trailing edge (later time of arrival) will present the ‘blue’ part. Negative GDD will identify what is called anomalous dispersion, causing the lower frequencies to be slower. Both cases result in similar reshaping of the pulse, with only a sign distribution difference in the frequency variation.

The description of the pulse phase via Taylor expansion of the spectral phase loses its usefulness in the presence of time-varying phase evolution terms. This can happen when the pulse encounters a temporally varying refractive index.

To understand how this can affect the pulse spectrum one could consider the case of a pulse travelling through a medium characterized by a sinusoidal refractive index

$$n(t) = n_0 + \Delta n \cos(\omega_{\mathrm{m}} t), \tag{2.29}$$

where ω_{m} is the angular frequency of the time-varying refractive index and Δn its amplitude. In particular, we want to show how new frequencies can be generated by such an oscillating phase, thus we consider the simplified case in which the refractive index oscillation period $2\pi/\omega_{\mathrm{m}}$ is short compared to both the pulse duration τ_{pulse} and the transit time through the material $t_{\mathrm{transit}} = L_{\mathrm{m}}/v_{\mathrm{g}}$, where L_{m} and v_{g} are the length of the material and the pulse group velocity, respectively. A pulse propagating through such a medium would acquire a phase such that the output field E_{out} is written as

$$E_{\mathrm{out}} = E_{\mathrm{in}} e^{i\omega_0\left(t - \frac{n_0 L_{\mathrm{m}}}{c}\right)} e^{-i\Delta_{\mathrm{m}}\cos(\omega_{\mathrm{m}} t)}, \tag{2.30}$$

where $\Delta_{\mathrm{m}} = \omega_0 \Delta n L_{\mathrm{m}}/c$. Using the Jacobi-Anger expansion[30] Equation 2.30 can be rewritten as

$$E_{\mathrm{out}} = E_{\mathrm{in}} e^{-i\left(\omega_0 \frac{n_0 L_{\mathrm{m}}}{c}\right)} \sum_{n=-\infty}^{\infty} (-1)^n J_n(\Delta_{\mathrm{m}}) e^{i(\omega_0 - n\omega_{\mathrm{m}})t} \tag{2.31}$$

where $J_n(x)$ is the n-th order Bessel function of the first kind. Equation 2.31 demonstrates such a phase modulation can result in the generation of new spectral components centred at frequencies spaced at integer multiples of ω_{m} from the central frequency ω_0. The amplitude of the generated sidebands depends on Δ_{m}, which is identified as the modulation depth. This is proportional to the optical frequency, propagation distance and amplitude of the refractive index modulation. An oscillating refractive index of this type will be utilized in the ARNIEMPM technique.

In general, molecular phase modulation (MPM) exploits molecular motion in a medium at THz frequencies, induced by the applied optical field. The slower response of the material to the incident electric field oscillation is due primarily to the difference in mass between electrons, which respond rapidly and determine the principal induced dipole moment of the molecules, and the much heavier nuclei, which become parametrically coupled to the electronic response. The resulting effect of this induced motion is a modulation at THz frequencies of the molecular dipole moment determined by the molecular dynamics (rotational and/or vibrational).

2.2 Quantum mechanical model of Raman interaction

In this section I present the quantum mechanical framework from which the ARNIEMPM technique has been formulated as presented by Bustard[31]. This is based on Von Neumann's density matrix formalism and the interaction representation of the Raman Hamiltonian.

As already mentioned in the introductory chapter (see fig.1.1), the ARNIEMPM approach consists of three main steps, which will be theoretically presented in the following section: an impulsive seeding of the molecular motion via a few-cycle pulse; an adiabatic amplification step of this initial motion via a longer and more energetic pulse; a modulation step, where the generated molecular motion is used as a phase modulator for another few-cycle pulse.

2.2.1 Raman scattering

As already mentioned in the introductory chapter, Raman scattering is an inelastic scattering process where incident photons are annihilated on scattering from an optical phonon in a molecular or crystalline medium and another photon is emitted at energies $\omega_{\text{out}} = \omega_{\text{in}} \pm \omega_{eg}$, where $\omega_{eg} = \omega_e - \omega_g$ is the phonon frequency. The labels e and g denote the excited and ground states of the molecular motion respectively. The emitted photons are named Stokes and anti-Stokes in the case of the red-shifted and blue-shifted photons respectively for historical reasons. The process can cascade, leading to frequency sideband generation over wide a spectral range.

Raman scattering can take place in both a spontaneous[21] and stimulated regime[20]. Spontaneous Raman scattering was first observed by Raman in 1928[15] and led to its widespread use in spectroscopy due to the inherent ability of the process to access dipole forbidden transitions.

In the case of a spontaneous process the phase of the emitted photon is randomly determined by the quantum zero-point fluctuations that initiate the transition (see figure 2.2). When in the presence of photons with energy corresponding to the Stokes field frequency, the process can be stimulated[28], resulting in the amplification of the Stokes radiation

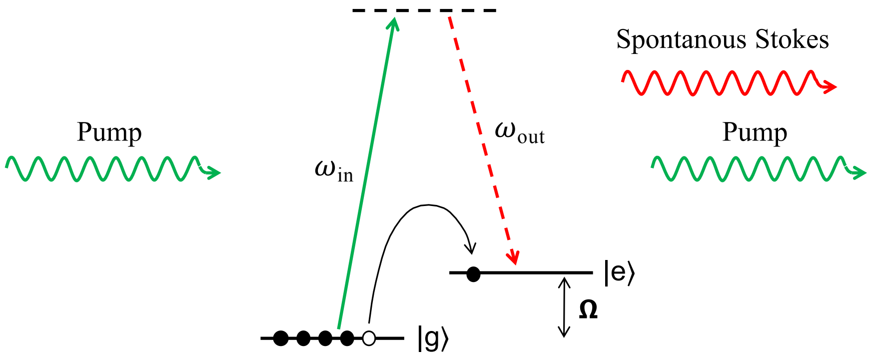

Figure 2.2: Spontaneous Raman scattering: an incident pump field is scattered by the material molecular motion, causing the emission of a Stokes photon with an energy difference equal to the molecular level spacing. The phase of the emitted Stokes is randomly defined by quantum zero-point effects.

(see figure 2.3). This is called stimulated Raman scattering (SRS). The process can be equivalently stimulated by the presence of a Stokes photon or of a molecular phonon, resulting in the amplification of the optical field or the material coherence respectively. The latter process is the process exploited in the ARNIEMPM technique to amplify the material coherence. A third scattering regime can be identified in the case of a pulse with a bandwidth large enough to span the molecular energy gap. This is known as impulsive stimulated Raman scattering (ISRS). In this case both the pump and Stokes fields originate

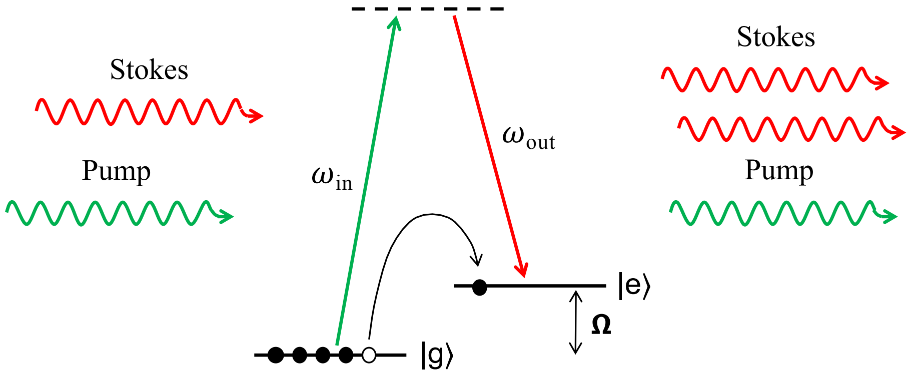

Figure 2.3: Stimulated Raman scattering (SRS): the presence of Stokes photons stimulates the Raman scattering process, resulting in the amplification of the Stokes field. The Stokes photons could be replaced by molecular phonons, leading to an analogous amplification process.

from the same pulse and possess well-defined relative phase. The slow material response to the optical field causes the material to be left in a coherent superposition of the molecular ro-vibrational levels after the pulse passage. ISRS technique is used by ARNIEMPM to initiate a material coherence with a defined phase relation with respect to the laser source from which the seed pulse is obtained.

2.2.2 Semi-classical approach

Following the approach of Bustard, the theoretical description presented in this chapter is semi-classical, using classic fields and quantized molecular dynamics. This is motivated by the unbalanced emission response between spontaneous and stimulated Raman scattering (SRS), which favours the latter in the presence of seeding. Quantum mechanically, spontaneous emission originates from the quantum zero-point ro-vibrational energy of the molecular medium and thus the generated Stokes photons have a random phase with respect to the pump laser field[32]. From both a theoretical[33] and experimental[34] point of view the ro-vibrational quanta for the SRS case are shown to grow more rapidly than their spontaneous counterparts in the presence of seeding phonons or Stokes photons. Therefore SRS emission with a well-defined phase is expected to dominate once it overcomes the quantum noise amplitude level. Spontaneous phenomena are thus neglected in the theoretical description of ARNIEMPM presented in this chapter, assuming that seeded dynamics play a dominant role in driving the molecular motion and the Stokes emission.

2.2.3 Classical fields

The analytic fields for the seed (se), pump (pu) and probe (pr) pulses constituting the ARNIEMPM technique are

$$\boldsymbol{E}_{\text{se}}(z,t) = \frac{1}{2}\left[A_{\text{se}}(z,t)e^{-i(\omega_{\text{se}}t - k_{\text{se}}z)} + \text{c.c.}\right]\hat{\boldsymbol{x}} \tag{2.32}$$

$$\boldsymbol{E}_{\text{pu}}(z,t) = \frac{1}{2}\left[A_{\text{pu}}(z,t)e^{-i(\omega_{\text{pu}}t - k_{\text{pu}}z)} + \text{c.c.}\right]\hat{\boldsymbol{x}} \tag{2.33}$$

$$\boldsymbol{E}_{\text{pr}}(z,t) = \frac{1}{2}\left[A_{\text{pr}}(z,t)e^{-i(\omega_{\text{pr}}t - k_{\text{pr}}z)} + \text{c.c.}\right]\hat{\boldsymbol{x}}, \tag{2.34}$$

where z is the propagation direction, after factoring out the (x, y) dependence (i.e. neglecting diffraction), and $\hat{\boldsymbol{x}}$ is the linear polarization direction, perpendicular to the wave propagation.

These pulses propagates through a molecular sample with a density N $[molecules \cdot m^{-3}]$ with a set of ro-vibrational states $|j\rangle$ whose energies are $\hbar\Omega_j$. These are coupled by the molecular polarizability Hamiltonian. The Stokes (S_{ij}) and anti-Stokes (aS_{ij}) transition angular frequencies are defined as

$$\omega_{S_{jk}} = \omega_{\text{pu}} - (\Omega_k - \Omega_j) \tag{2.35}$$

$$\omega_{aS_{jk}} = \omega_{\text{pu}} + (\Omega_k - \Omega_j), \tag{2.36}$$

for $\Omega_k > \Omega_j$. ω_{pu} represent the pump field frequency and Ω_j, Ω_k represent respectively the frequencies associated with the energy of the j nand k molecular levels involved in the transition.

2.2.4 Material dynamics

The unperturbed system Hamiltonian is

$$\hat{H}_{\mathrm{mol}} = \sum_j \hbar\omega_j \left|j\right\rangle \left\langle j\right| , \tag{2.37}$$

wiht ω and the molecule-field interaction is governed by the dipole Hamiltonian[35]

$$\hat{H}_{\mathrm{dip}} = -\hat{\boldsymbol{\mu}} \cdot \boldsymbol{E}, \tag{2.38}$$

where $\hat{\boldsymbol{\mu}}$ is the dipole operator.

The system evolution is governed by the Schrödinger equation

$$i\hbar\partial_t \left|\Psi(t)\right\rangle = \left[\hat{H}_{\mathrm{mol}} + \hat{H}_{\mathrm{dip}}\right] \left|\Psi(t)\right\rangle , \tag{2.39}$$

where $\left|\Psi(t)\right\rangle = \sum_j c_j(t)e^{-i\omega_j t} \left|j\right\rangle$ is the complete set of the molecular system field-free basis states.

As derived by Bustard[31] following Shore[35] and Sussman *et al.*[36], one can write the Schrödinger equation in the interaction picture as

$$i\hbar\dot{c}_k = \sum_j V_{kj}^{\mathrm{eff}} e^{-i\omega_{kj}t} c_j(t) \tag{2.40}$$

with $\omega_{kj} = \omega_k - \omega_j$. The effective potential $V_{kj}^{\mathrm{eff}} = V_{kj}^{\mathrm{dip}} + V_{kj}^{\mathrm{Ram}}$ is defined as the sum of the dipole interaction Hamiltonian

$$V_{kj}^{\mathrm{dip}} = -\hat{\boldsymbol{\mu}}_{jk} \cdot \boldsymbol{E}, \tag{2.41}$$

and the Raman interaction Hamiltonian defined as

$$V_{kj}^{\mathrm{Ram}} = -\sum_{qq'} \boldsymbol{E}_q^{(-)} \cdot \boldsymbol{\alpha}_{kj}(\omega_{q'}, \omega_q) \cdot \boldsymbol{E}_{q'}^{(+)} \tag{2.42}$$

$$= -\frac{1}{4} \sum_{qq'} \boldsymbol{A}_q^* \cdot \boldsymbol{\alpha}_{kj}(\omega_{q'}, \omega_q) \cdot \boldsymbol{A}_{q'} e^{-i\omega_{q'q}t}. \tag{2.43}$$

where $\omega_{q'q}$ is the frequency difference between the two fields $E_{q'}$ and E_q Here, $\boldsymbol{\alpha}_{kj}(\omega_{q'}, \omega_q)$ is the tensor polarizability operator for dipole transitions between states, whose matrix elements are defined in Cartesian coordinates $\{a, b \in x, y, z\}$ as

$$\alpha_{kj}^{ab}\left(\omega_{q'}, \omega_q\right) = \frac{1}{\hbar} \sum_p \left[\frac{\mu_{kp}^a \mu_{pj}^b}{\omega_{pj} - \omega_{q'}} + \frac{\mu_{kp}^b \mu_{pj}^a}{\omega_{pj} + \omega_q} \right], \tag{2.44}$$

where p denotes non-essential non-resonant higher states different from the essential j, k states among which the Raman transition takes place, the various μ are the components of the dipole momentum and ω the frequencies associated with the transitions and fields identified by the labels. The Raman interaction 2.43 can be written as

$$V_{kj}^{\mathrm{Ram}} = -\frac{1}{4} \sum_q \boldsymbol{A}_q^* \cdot \boldsymbol{\alpha}_{kj}(\omega_q, \omega_q) \cdot \boldsymbol{A}_q \tag{2.45}$$

$$-\frac{1}{4} \sum_{q,q' \neq q} \boldsymbol{A}_q^* \cdot \boldsymbol{\alpha}_{kj}(\omega_{q'}, \omega_q) \cdot \boldsymbol{A}_{q'} e^{-i\omega_{q'q}t}. \tag{2.46}$$

The first term in 2.46 identifies the dynamic Stark effect (DSE), while the second refers to Raman scattering between ro-vibrational levels. These two phenomena play different roles in the resulting molecular dynamics. The DSE affects dynamically the ro-vibrational levels by shifting their energy by an amount proportional to the field intensity. This is due to the fast variation of the field with respect to time scale of the molecular dynamics. This is different from the regular Stark effect, where the energy shift follows the field amplitude. If the field intensity is slow-varying with respect to the level splitting, then the state amplitudes follow adiabatically the intensity envelope $|A_q|^2$. The DSE potential causes the molecules to slowly evolve in a superposition of the molecular eigenstates and return to the original situation when the field intensity returns to zero, with only a phase term difference. This effect is used in adiabatic molecular alignment, where long (with respect to the molecular motion) duration pulses are used to forcibly align the molecules following the applied field intensity[37].

The Raman scattering term in equation 2.46 plays a different role. If the field is assumed to rapidly vary on the time scale of the molecular motion the resulting system evolution is diabatic. The molecules are left in a coherent superposition of field-free eigenstates after the driving field is gone, as they cannot adapt rapidly enough to the changing Hamiltonian. Energy is then left in the molecules after the passage of the field. In this regime Raman scattering creates field-free coherent dynamics which survive the applied field. This approach is the key element in stimulated Raman scattering (SRS) and impulsive stimulated Raman scattering (ISRS) and will play a pivotal role in the work presented in this thesis. The ARNIEMPM approach relies on coherently preparing the molecular dynamics with the application of two different pulses of fs and ps durations and exploiting this ns duration timescale motion to act as a phase modulator for the third pulse, which will encounter a refractive index which oscillates in time with a period determined by the molecular motion. It should be noted that this diabatic approach can be also exploited with longer pulses in the case of off-resonant fields with a sufficiently strong intensity. This approach relies on the application of near-resonant pump and Stokes fields with ns duration to stimulate a coherent superposition of molecular states[38,39].

2.2.5 Density matrix formalism

It is useful at this stage to introduce the Von Neumann density matrix formalism to model the system evolution. The density operator, defined as

$$\hat{\rho} = \sum_i p^{(i)} |\Psi^{(i)}\rangle\langle\Psi^{(i)}|, \tag{2.47}$$

is needed to describee physical systems in which the state of the system is a classical mixture of pure states. The density operator evolves in time according to the generalized Schrödinger equation

$$\frac{d\hat{\rho}}{dt} = \frac{i}{\hbar}\left[\hat{\rho}, \hat{H}\right]. \tag{2.48}$$

where $\hat{H}$ is the system Hamiltonian. $p^{(i)}$ is the probability that the system is in the normalized state $|\Psi^{(i)}\rangle$. In this formalism, the expectation value of an operator $\hat{O}$ when the system is prepared in state $\hat{\rho}$ is defined through the trace operation as $\langle\hat{O}\rangle = \mathrm{Tr}\left(\hat{\rho}\hat{O}\right)$.

Different from the state-vector approach, the density matrix formalism is more appropriate for statistical ensembles of quantum systems and can model quantum systems which have dissipative interactions with the environment, as in our case.

Rewriting 2.43 to pick up a z-dependent phase given by the transformation $A_q \to A_q e^{ik_q z}$ as

$$\hat{V}^{\mathrm{Ram}} = -\frac{1}{4} \sum_{qq'} A_q^* \hat{\alpha} A_{q'} e^{-i\omega_{q'q} t} e^{i(k_{q'} - k_q) z} \tag{2.49}$$

one can solve 2.48 for the density matrix components. Ignoring the elements which lead to Stark shift, the diagonal elements will evolve according to

$$\frac{\partial \rho_{jj}}{\partial t} = -\frac{i}{4\hbar} \sum_{k \neq y} \sum_{qq'} (\rho_{jk}\alpha_{kj} - \alpha_{jk}\rho_{kj}) A_q^* A_{q'} e^{-i\omega_{q'q} t} e^{i(k_{q'} - k_q) z}, \tag{2.50}$$

while the off-diagonal elements evolution is described as

$$\frac{\partial \rho_{ij}}{\partial t} = -i\Omega_{ij}\rho_{ij} - \frac{i}{4\hbar} \left[w_{ij}\alpha_{ij} + \sum_{k \neq i,j} (\rho_{ik}\alpha_{kj} - \alpha_{ik}\rho_{kj}) \right] \sum_{qq'} A_q^* A_{q'} e^{-i\omega_{q'q} t} e^{i(k_{q'} - k_q) z}, \tag{2.51}$$

where $w_{ij} = \rho_{ii} - \rho_{jj}$. The second term in 2.51 can be ignored in the case of small induced coherences, uneven ro-vibrational level spacing or in the case where a single Stokes sideband dominates.

2.3 The ARNIEMPM model

In this section I will present the ARNIEMPM model itself and the mathematical description used to describe the Raman-based laser-matter interaction at each of the three steps.

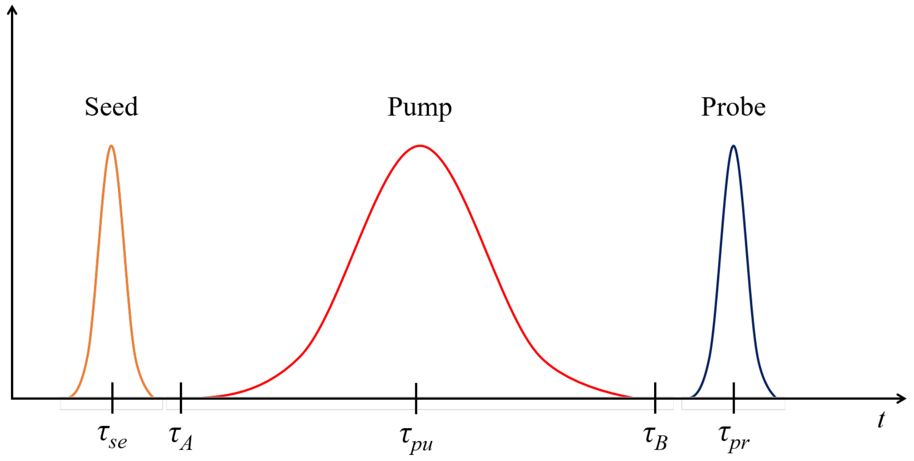

Figure 2.4: The ARNIEMPM pulse train.

2.3.1 Impulsive & transient limit

Equation 2.51 can be used to describe the effect of the various pulses constituting the ARNIEMPM technique under the specific experimental parameters. The three pulses, seed, pump and probe, interact differently with the molecular medium according to their bandwidth and duration with respect tp the molecular dynamics. Two situations can be identified, respectively the impulsive regime, for seed and probe, and the transient regime, for the pump pulse. The first refers to pulses with a bandwidth spanning the Raman energy gap Ω_{ij}, which for a Fourier-transform limited (FTL) pulse corresponds to a FWHM duration $\Delta\tau \lesssim 2\pi/\Omega_{ij}$. The transient regime refers to a pulse with duration $\Delta\tau$ such as $T_{2(ij)} \gtrsim \Delta\tau > 2\pi/\Omega_{ij}$, where $T_{2(ij)}$ is the coherence dephasing time associated with the particular molecular motion.

In both cases, a phenomenological damping term can be added to the density matrix elements to account for the dephasing caused by collisions between molecules. For diagonal elements, a term $-\rho_{jj}/T_{1(jj)}$ is added to equation 2.50, accounting for the damping of population to lower energy levels due to collisions between molecules, where $T_{1(jj)}$ is the characteristic time associated with this dephasing. For off-diagonal terms, $-\rho_{ij}/T_{2(ij)}$ is added to 2.51, with the aforementioned coherence dephasing time $T_{2(ij)}$.

In the remainder of this chapter the phenomenological damping will be expressed in terms the dephasing rate $\Gamma_{ij} = T_{2(ij)}^{-1}$ expressed in radians per seconds, which corresponds to the half-width at half maximum (HFHW) of the spontaneous Raman linewidth of the specific transition[40].

2.3.2 Propagation: the reduced wave equation

The optical fields propagation in the molecular medium is described by the IWE 2.8. The fields experience linear dispersion from the material and the Raman interaction is present as a polarization source term. The IWE can be simplified from a second-order equation to a first-order partial differential equation, identified as the reduced wave equation (RWE).

To do so, consider the analytic signal as

$$E^{(+)}(z,t) = \frac{1}{2} A_q(z,t) e^{i(k_q z - \omega_q t)}, \tag{2.52}$$

with the slowly varying envelope A_q and similarly the polarization source terms

$$P^{(+)}(z,t) = \frac{1}{2} \mathcal{P}(z,t) e^{i(k_q z - \omega_q t)}. \tag{2.53}$$

From the frequency domain IWE

$$\left[\partial_z^2 + \frac{\omega^2}{c^2}\right] \tilde{E}^{(+)}(z,\omega) = -\frac{\omega^2}{\epsilon_0 c^2}\tilde{\mathcal{P}}^{(+)}(z,\omega), \tag{2.54}$$

one obtains the RWE by inserting the Fourier transforms of 2.52 and 2.53 and applying the inverse Fourier transform. Two assumptions must be used: the slow-varying envelope approximation (SVEA) [27] to remove the second-order partial derivatives, and the fact that the envelopes are peaked around ω_q.

This yields the RWE as

$$\partial_z A_q(z,t) = i\frac{1}{2\epsilon_0 c}\left(\omega_q \mathcal{P}_q(z,t) - \partial_t \mathcal{P}_q(z,t)\right). \tag{2.55}$$

The second term can be neglected for a polarization envelope which is slowly-varying on a time scale $2\pi/\omega_q$. Here, following Bustard again, the polarization term $\mathcal{P}_q(z,t)$ is defined as

$$\mathcal{P}_q(z,t) = N\sum_{ij}\alpha_{ij}\rho_{ji}A_q(z,t). \tag{2.56}$$

where N is the molecular density and ρ_{ji} is termed here the "molecular coherence" or simply "coherence".

2.3.3 (A): seeding of the molecular coherence

The seeding process can be modelled from equation 2.51. In the first ARNIEMPM formulation, the seed is assumed to be in the purely impulsive regime, the dispersion is neglected as is depletion, such that $A_{\text{se}} = A_{\text{se}}(\eta_{\text{se}})$.

Including the phenomenological damping term, one obtains

$$\frac{\partial \rho_{ij}}{\partial \eta_{\rm se}} = -i(\Omega_{ij} - i\Gamma_{ij})\rho_{ij} - \frac{i}{4\hbar} w_{ij}\alpha_{ij}|A_{\rm se}(\eta_{\rm se})|^2 \tag{2.57}$$

Assuming there is no initial coherence ($\rho_{ij}(z,0) = 0$), this can be integrated to give

$$\rho_{ij}(z,\eta_{\rm se}) = \left[-\frac{i}{4\hbar} w_{ij}\alpha_{ij} \int_0^{\eta_{\rm se}} |A_{\rm se}(\eta'_{\rm se})|^2 e^{-i(\Omega_{ij}+i\Gamma_{ij})\eta'_{\rm se}} d\eta'_{\rm se}\right] e^{i(\Omega_{ij}+i\Gamma_{ij})\eta_{\rm se}}. \tag{2.58}$$

Equation 2.58 shows that a seed with a duration comparable to the motion period $2\pi/\Omega_{ij}$ will generate a coherence, while a longer seed will cause the coherence to follow adiabatically and vanish together with the seed pulse amplitude. The coherence situation described by by 2.58 is the initial condition of the molecular medium for the amplification step performed by the pump pulse.

2.3.4 (B): amplification of the molecular coherence

The pump pulse falls fully in the transient domain. In the original ARNIEMPM implementation the pump is assumed to be undepleted, and the S1 and AS1 sidebands have only been considered in terms of propagation. By defining the slowly varying quantity

$$Q_{ij} = \rho_{ij} e^{i\left[(k_{\rm pu} - k_{{\rm S}_{ij}})z - \Omega_{ij} t\right]} \tag{2.59}$$

in the transient limit, from the RWE and 2.51 one can obtain

$$\partial_z A_{\mathrm{S}_{ij}} = i\beta_{\mathrm{S}_{ij}} A_{\mathrm{pu}} Q_{ij}(z,t) \tag{2.60}$$

$$\partial_z A_{\mathrm{aS}_{ij}} = i\beta_{\mathrm{aS}_{ij}} A_{\mathrm{pu}} Q^*_{ij}(z,t) \tag{2.61}$$

$$\frac{\partial Q_{ij}}{\partial t} = -\Gamma_{ij} Q_{ij} - i\bar{\kappa}_{ij}\left[A^*_{\mathrm{pu}} A_{\mathrm{S}_{ij}} + A_{\mathrm{pu}} A^*_{\mathrm{S}_{ij}} e^{i\Delta k_{ij} z}\right], \tag{2.62}$$

where $\Delta k_{ij} = 2k_{\mathrm{pu}} - k_{\mathrm{S}_{ij}} - k_{\mathrm{aS}_{ij}}$, with the subscripts pu, S_{ij} and aS_{ij} referring to the pump, Stokes and anti-Stokes fields respectively for the ij Raman transitions. The coupling constant is defined as $\bar{\kappa}_{ij} = \frac{w_{ij}\alpha_{ij}}{4\hbar}$ and the propagation constant as $\beta_q = \frac{N\alpha_{ij}\omega_q}{2\epsilon_0 c}$. Solutions to equations 2.62, 2.60 and 2.61 can be obtained via Laplace transformation[31].

The crucial role of the dispersion contribution in 2.62 should be noted. A negligible dispersion ($e^{i\Delta k_{ij} z} = 1$) would cause Stokes and anti-Stokes field to remain coupled and prevent any coherence amplification. When dispersion is present, this term causes the anti-Stokes field to decouple from the material coherence[28], allowing the Stokes field to grow and amplify the coherences.

In this case, for a time $\tau > \tau_A$ where τ_A is the starting time of the coherence amplification step (see figure 2.4), one obtains the following:

$$Q_{ij}(z,\tau) = Q_{ij}(\tau_A) e^{-\Gamma_{ij}(\tau-\tau_A)} I_0\left[\sqrt{4h(\tau)z}\right], \tag{2.63}$$

where $I_n(x)$ are modified Bessel functions of n-th order[41] and

$$h(\tau) = \bar{\kappa}_{ij}\beta_{\mathrm{S}_{ij}} \int_{\tau_A}^{\tau} |A_{\mathrm{pu}}(\tau')|^2 d\tau'. \tag{2.64}$$

Equation 2.63 can be further simplified by considering the case of a square pump pulse and expressed in terms of the coherences Raman gain coefficients g_{ij}. For a square pump pulse with constant intensity I_p and duration $\Delta\tau_{\mathrm{pu}}$ the coherences can be written as

$$Q_{ij}(z, \tau_B) = Q_{ij}(\tau_A) e^{-\Gamma_{ij}(\tau_B - \tau_A)} I_0 \left[\sqrt{2 g_{ij} I_{\mathrm{pu}} L \Gamma_{ij} \Delta\tau_{\mathrm{pu}}} \right], \tag{2.65}$$

where L in the length of the interaction region and

$$g_{ij} = \frac{4\bar{\kappa}_{ij} \beta_{\mathrm{S}_{ij}}}{\epsilon_0 c \Gamma_{ij}} = \frac{w_{ij} N \alpha_{ij}^2 \omega_{\mathrm{S}_{ij}}}{2\hbar \epsilon_0^2 c^2 \Gamma_{ij}} \tag{2.66}$$

is the *Raman gain coefficient*, expressed in units of cmW^{-1}. The Raman gain is defined as

$$G = g_{ij} I_{\mathrm{pu}} L \Gamma_{ij} \Delta\tau_{\mathrm{pu}}. \tag{2.67}$$

One can see how the Raman gain is linearly proportional with respect to the gain coefficient, the medium length, and the pump flux ($\Delta\tau_{\mathrm{pu}}$), making these three quantities the principal parameters to maximize in order to increase the Raman process efficiency.

Equation 2.65 is the initial condition encountered by the probe propagating through the molecular medium, with τ_B indicating the starting time of the phase modulation step (see figure 2.4).

2.3.5 (C): phase modulation from the molecular medium

For the third step of the ARNIEMPM technique, a weak probe pulse propagates through the molecular medium in the impulsive regime, after the pump pulse is gone. The coherences evolution then follow the expression

$$\rho_{ij}(z,\tau) = \rho_{ij}(z,\tau_B) e^{i(\Omega_{ij}+i\Gamma_{ij})(\tau-\tau_B)} \tag{2.68}$$

for $\tau \geqslant \tau_B$. Here $\rho_{ij}(z,\tau_B)$ is a function of z given by equation 2.63 for the coherence evolution calculated at the probe modulation starting time τ_B (see figure 2.4). The reduced wave equation 2.55 can be used to model the probe propagation as

$$\partial_z A_{\mathrm{pr}}(z,\tau) = i\beta_{\mathrm{pr}_{ij}} \left[\rho_{ij}(z,\tau) + \rho^*_{ij}(z,\tau)\right] A_{\mathrm{pr}}(z,\tau), \tag{2.69}$$

where the second term in equation 2.55 (time-derivative of the polarization term) has been neglected. If we assume the probe influence to be negligible on the amplified coherence (equation 2.68), equation 2.69 can give solutions of the form

$$A_{\mathrm{pr}}(L,\tau) = A_{\mathrm{pr}}(0,\tau) \prod_{i,j>i} \exp\left\{ i\beta_{\mathrm{pr}_{ij}} \int_0^L \left[\rho_{ij}(z,\tau) + \rho^*_{ij}(z,\tau)\right] dz \right\}, \tag{2.70}$$

at a propagation distance L along the medium. To highlight the phase modulation effect, it is useful to consider a delta function seed pulse. From equations 2.58, 2.59 and 2.65 one can write equation 2.70 as

$$A_{\mathrm{pr}}(L,\tau) = A_{\mathrm{pr}}(0,\tau) \prod_{i,j>i} \exp\left\{ i\delta^{\mathrm{mod}}_{ij} \sin\left[\Omega_{ij}(\tau-\tau_{\mathrm{se}})\right] \right\}, \tag{2.71}$$

where

$$\delta^{\mathrm{mod}}_{ij} = 4\beta_{\mathrm{pr}_{ij}} \bar{\kappa}_{ij} |A_0|^2 e^{-\Gamma_{ij}(\tau-\tau_{\mathrm{se}})} \frac{L^{3/2}}{\sqrt{2G}} I_1\left[\sqrt{2G}\right]. \tag{2.72}$$

By comparing equation 2.71 with 2.31 it is evident how the probe is modulated at the ro-vibrational frequency Ω_{ij}. The molecular modulation depth $\delta_{ij}^{\mathrm{mod}}$ depends linearly on the seed energy and nonlinearly on the pump energy, confirming the feasibility of the ARNIEMPM approach in which a weak coherence is impulsively seeded by a weak short pulse and subsequently amplified by a more powerful pump pulse. The resulting coherent preparation allows the phase modulation of a probe pulse propagating through the material, according to equation 2.70.

From this, other crucial aspects of the ARNIEMPM approach emerge. It can be seen how the modulation phase and thus the probe's modulated phase depends exclusively on their delay relative to the seed, with no dependence on the pump. The modulation depth is dependent on the integrated temporal intensity (thus the pump fluence), making the amplification step independent of the pump temporal structure and phase.

2.4 Selection of experimental parameters

The calculations reported in this chapter have been used to determine the experimental parameters for my ARNIEMPM experiment in terms of gas medium, geometry and laser parameters.

As stated in the introductory chapter, the goal of this implementation of the ARNIEMPM technique is to obtain isolated few-cycle pulses at UV wavelengths via molecular phase modulation. This imposes some clear conditions that need to be met in my experimental investigation.

The first decision concerns the choice of molecular medium and will affect every aspect of the experimental design, determining both the seed, pump and probe duration, bandwidth and energy, and the geometry of the light-matter interaction. The original implementation of ARNIEMPM[19] was realized using rotating hydrogen molecules, corresponding to a 17.5 THz Raman energy shift (57 fs rotational period). This is well below the bandwidths that can be achieved with existing methods, such as second- and third-harmonic generation, linear and nonlinear optical parametric amplification, etc., and thus do not provide any substantial contribution towards the stated goal. The vibrational Raman shift for various diatomic molecules is of the order 100 THz, and is therefore far more suitable for the task. Of the various molecules considered, hydrogen possesses the largest vibrational shift, equal to a natural frequency shift of $\tilde{\Omega}_{\mathrm{H}_2} = 124.65\,\mathrm{THz}$ and thus provides the largest spectral modulation available. The choice of molecular medium restricts the parameters for a suitable seed pulse as the ARNIEMPM technique requires the seed to start the molecular coherence by ISRS. This is equivalent to having a pulse with a bandwidth spanning the chosen Raman energy shift. The probe pulse is also important, as in order to obtain an isolated pulse the probe spectrum should overlap with the stimulated Raman vibrational sidebands. The probe pulse must then posses a spectrum supporting a FTL duration at least equal to the vibrational period, $\Delta t_{\mathrm{pr}} \leqslant 8\,\mathrm{fs}$ in the case of hydrogen, where Δt_{pr} is the probe temporal FWHM. These constraints create a trade-off between the temporal compression achievable on the probe through spectral broadening and the experimental resources available to deliver the correct pulses. Deuterium was considered as an alternative due to its smaller (but sufficient) vibrational period ($\tilde{\Omega}_{\mathrm{D}_2} = 89.61\,\mathrm{THz}$, corresponding to a vibrational period $\Delta\tau \approx 11fs$). However, D_2 possesses a smaller laser cross section with respect to H_2 and would provide a smaller modulation depth. The experimental requirements in terms of technology and resources necessary to obtain a probe pulse suitable for use with vibrational hydrogen were deemed feasible and H_2 was selected as the molecular medium. Chapter 3 will present the details of the experimental setup and the techniques used to create suitable laser probes.

The choice of vibrational motion provides an advantage in terms of higher Raman gain because of the energy level occupation. The Raman gain coefficient expression 2.66 depends linearly on the factor $w_{ij} = \rho_{ii} - \rho_{jj}$, representing the population of the ro-vibrational levels. The molecular level occupation follows the Boltzmann thermal distribution. The vibrational level energy spacing implies that the vibrational population is almost entirely in the fundamental level $v = 0$ at room temperature, where v is the vibrational level quantum number, hence maximizing w_{ij}.

As stated in the introduction, I chose to utilize a single light source to provide all of the necessary pulses for the ARNIEMPM technique. This limits the available pulse energy, so I focussed my efforts on providing enough amplification and obtain sufficient vibrational coherence to modulate the probe. The chosen pump source (see chapter 3) is different in terms of central wavelength, energy and duration with respect to Bustard's work[19]. The wavelength (800 nm instead of 527 nm) and energy (1 mJ instead of 70 mJ) of the available pump pulse strongly limit the achievable Raman gain. One can quantify this effect by using the empirical formulas for the Raman gain coefficients for the fundamental rotational $S_{00}(1)$ and vibrational $Q_{01}(1)$ transitions, developed respectively by Bischel and Dyer[42] and Meng[43]. Figure 2.5 shows the calculated Raman gain coefficient for the different choice of pump wavelengths for different gas pressures, for both the rotational and vibrational case. It can be seen how the 800 nm pump causes a factor of ~ 2 reduction in the calculated gain.

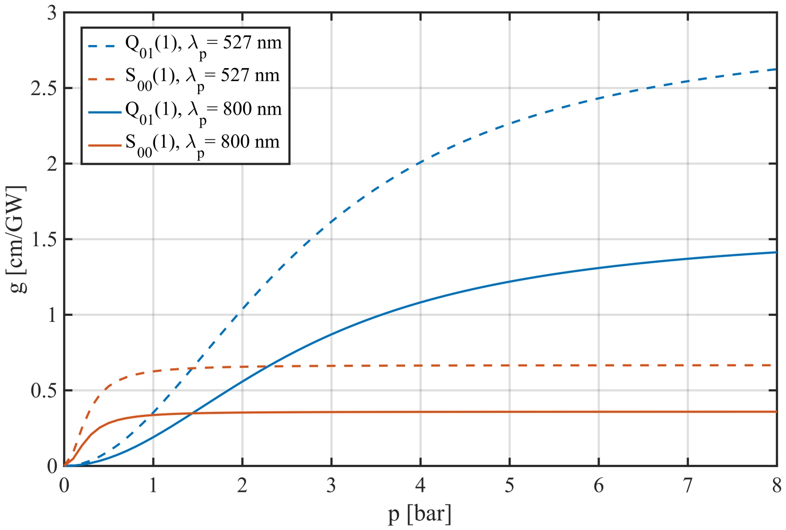

Figure 2.5: Raman gain coefficient as a function of H_2 absolute pressure, at room temperature: comparison of the calculated Raman gain coefficients for the rotational (blue lines) and vibrational (orange lines) transitions, for different choices of the pump pulse wavelength: 527 nm, like in the first ARNIEMPM implementation, or 800 nm as in the work presented in this thesis. The 800 nm pump gain is almost halved with respect to the 527 nm pump case.

This limitation has been alleviated by selecting a sufficiently high gas pressure so that the Raman gain coefficient is higher that the one previously used. Practical design limitations restricted the maximum operating pressure to 4 bar (absolute). As can be seen in figure 2.5, the vibrational gain in my case is higher than the rotational gain utilized by Bustard, where he operated at 1 bar.

This choice of pressure also ensures that vibrational transitions are favoured with respect to rotational ones, as one cannot have a purely rotational or vibrational coupling without implementing any sort of gating (by exploiting pulse polarization and selection rules for example).

The selection rules themselves play to the vibrational case. All energy levels are accessible due to the selection rules for vibrational molecular transitions being $v = \pm 1$.

The energy limitations on the pump will be alleviated by using a waveguide to increase the interaction length of the process. In Bustard's work, the ARNIEMPM interaction length was empirically assumed to be on the order of the Rayleigh range of the focussed beams, equivalent to a few cm. The presence of the waveguide (1 m length) will cause a factor ~ 10 increase in the interaction length. The gain expression (eq.2.67) depends linearly on the medium length, so this increase should partially compensate for the reduction in pump energy.

The third difference is the pump pulse duration (~ 100 ps instead of 10 ns) and this is advantageous. A pulse shorter than the coherence decay time implies that most of its energy is efficiently used during the amplification process. In my case, the calculated vibrational linewidth $\Gamma/2\pi$ for $Q_{01}(1)$ at 4 bar and room temperature is 138.06 MHz, corresponding to a decay time of 7.2 ns, two orders of magnitude larger that the pump pulse duration. For Bustard's case, the calculated Raman linewidth for $S_{00}(1)$ at 1 bar at room temperature is 55.57 MHz, corresponding to a coherence decay time of 27.5 ns, which very close to the pump pulse duration. This aspect should help to further mitigate the relative energy difference, enhancing the efficiency of the amplification step.

Chapter 3

Experimental setup for vibrational phase modulation

In this chapter I describe the experimental configuration used to test and demonstrate the feasibility to use vibrational Raman transition in hydrogen as an ultrashort phase modulator. Here we must generate three synchronized short pulses (seed, pump, and probe) with different energy, spectra and duration. I will highlight the reasoning for the choice of configuration used for each part of the setup, but the description of the results will be deferred to chapters 4 and 5, describing the material preparation and the probe modulation respectively. The compete experimental setup is quite complex, requiring the generation of seed, pump and probe and suitable diagnostics, each of which are described in the appropriate sections. I will present the various elements following the laser chain from which they are derived, then introduce the measurement techniques used in the system development.

The full laser chain system (see figure 3.2) is composed of three main components:

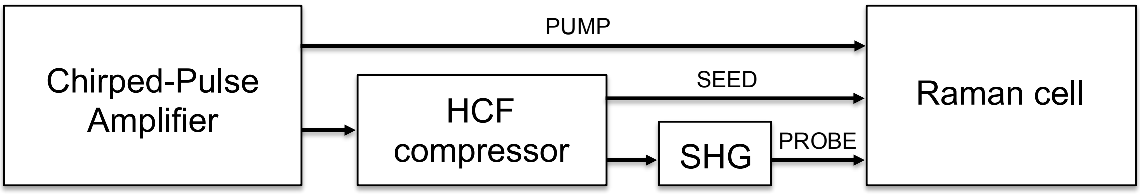

Figure 3.1: The laser chain system, composed of four main elements, provides the three pulses (seed, pump and probe) required for the ARNIEMPM approach.

chirped pulse amplifier (CPA); single laser source to generate the seed, pump and probe pulses, ensuring optical synchronisation; hollow core fibre (HCF) pulse compressor used to directly broaden and temporally compress the CPA output to generate the seed pulse; second harmonic generation (SHG) used to generate the probe; and Raman gas cell acting as the molecular Raman phase modulator.

3.1 Chirped-pulse amplifier

The first element, from which all the beams used in the experiment are derived, is a commercial (KMLabs Dragon) chirped-pulse amplifier (CPA). This generates up to 3 mJ pulses with a FWHM duration of $\Delta\tau \sim 25\,\text{fs}$, centred around 800 nm wavelength at 1 kHz repetition rate. Fig.?? presents a schematic view of the CPA concept.

In order to generate the stretched pump pulse, the system has been modified with the insertion of a 50:50 beam splitter (BS) before the grating pulse compressor used to compress the amplified, stretched CPA output. The reflection from this beam splitter corresponds to temporally stretched 2 mJ pulses, with an estimated[1] duration $\Delta\tau \sim 100\,\text{ps}$, with the same bandwidth of the nearly Fourier-tansform limited CPA main output (see fig.3.3).

---

[1] The pump pulse duration has been estimated by measuring the compressor geometry and calculating the negative dispersion it introduces, then numerically applying this dispersion to the measured $\sim 25\,\text{fs}$ CPA output pulse.

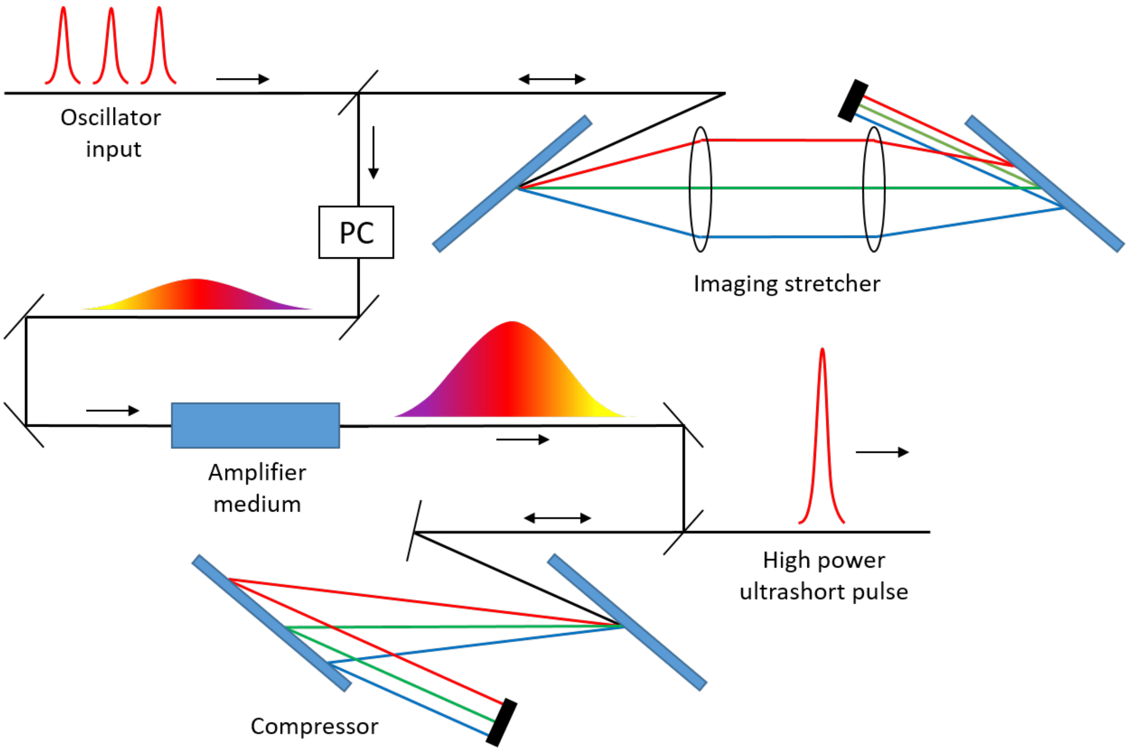

Figure 3.2: The chirped-pulse amplifier concept: the output of a boradband oscillator is stretched in time using an imaging stretcher; a Pockel's cell (PC) is used to pick one pulse from the oscillator high-repetition pulse train; the stretched pulse is amplified by travelling through an active medium; a grating compressor is used to temporally recompress the amplified pulse, providing a high-energy ultrashort pulse as an output.

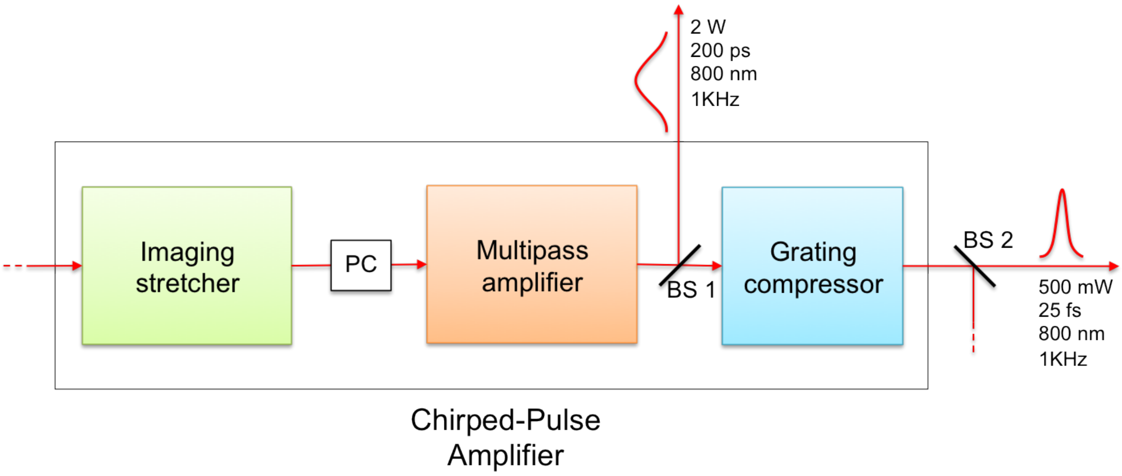

Figure 3.3: The CPA system: a 50% beam splitter (BS1) is inserted before recompressing the pulse after amplification, providing the temporally stretched pump pusle necessary for ANIEMPM. The main compressed output is sent to the few-cycle source to generate the seed & probe pulses (see section 3.2). PC: Pockel's cell; BS1, BS2: 50% beam splitters.

The remaining total CPA output is divided with another 50% BS, the reflection of which ($\sim 500\,\mathrm{mW}$) is sent to the HCF-based pulse compressor.

3.2 Few-cycle sources

3.2.1 Self-phase modulation pulse compressor

The second element of the laser chain is a hollow-core fibre (HCF) based pulse compressor. This system exploits self-phase modulation (SPM) in a noble gas followed by spectral phase compensation to achieve pulse temporal compression down to the few-cycle regime. The fundamentals of this process can be understood by taking into account what has been said in Chapter 2 regarding the nonlinear response of materials exposed to intense radiation. Equation 2.21 presents the Taylor expansion of the polarization response to the applied field. In the case of a centrosymmetric material, as is the case for noble gases, the second order nonlinearity is zero, as are all other even terms, due to symmetry considerations. The polarization can then be approximated as the sum of a linear plus a third order term and used to solve the IWE. The $\chi^{(3)}$ nature of the SPM process causes it to depend on $|E|^2E$ and is thus reflected in a refractive index which depends on the intensity of the applied pulse:

$$n(I) = n_0 + n_2 \cdot I \tag{3.1}$$

where n_0 is the linear refractive index and n_2 is the second order nonlinear refractive index of the medium. The pulse propagation causes the refractive index to be time dependent, following the evolution of pulse intensity envelope. Considering a simple pulse with a gaussian envelope in the pulse co-moving reference frame:

$$I(t) = I_0 \exp\left(-\frac{t^2}{\tau^2}\right) \tag{3.2}$$

with I_0 as the peak intensity and τ as half the pulse temporal duration (the envelope HWHM). The time-varying refractive index is

$$\frac{dn(I)}{dt} = n_2\frac{dI}{dt} = n_2 \cdot I_0 \cdot \frac{-2t}{\tau^2} \cdot \exp\left(-\frac{t^2}{\tau^2}\right), \tag{3.3}$$

which causes the instantaneous phase to evolve accordingly as

$$\phi(t) = \omega_0 t - \frac{2\pi}{\lambda_0} \cdot n(I)L, \tag{3.4}$$

where ω_0 and λ_0 are respectively the pulse central frequency and wavelength and L is the length travelled through the medium. From 3.3 and 3.4 the instantaneous frequency can be written as

$$\omega(t) = \frac{d\phi(t)}{dt} = \omega_0 + \frac{4\pi L n_2 I_0}{\lambda_0 \tau^2} \cdot t \cdot \exp\left(-\frac{t^2}{\tau^2}\right), \tag{3.5}$$

which shows a a frequency shift with opposite signs on each side of the pulse envelope peak. In particular, the leading edge of the pulse shifts to lower frequencies, while th trailing edge shifts to higher frequencies. This causes the spectral broadening of the pulse input spectrum. In common nonlinear media, like the case of neon gas, normal chromatic dispersion is present, adding GDD to the SPM effect and causing the generated frequencies to quickly walk off temporally and prevents interference effects. This causes the generated broadened spectrum to possess a linear chirp at the output of the SPM system, which can be compensated to obtain a fully compressed pulse that is temporally shorter than the input pulse, thanks to the spectral broadening. A more detailed treatment of the process can be found in the relevant contribution from De Silvestri*et al.*[44], as well as the seminal work of Nisoli *et al.*[5,6] and subsequent publications.

The design of the SPM experimental system is based on the one developed at Imperial College, which has been demonstrated capable of achieving a 3.4 fs pulse duration[45]. The system consists of a 90 cm fused silica (FS) glass hollow-core capillary, with an internal diameter (ID) of 260 μm an outside diameter (OD) 1.5 mm. This is mounted in a support capillary (ID: 2 mm, OD: 6 mm), held in place with epoxy resin on one end of the support capillary, completely sealing the space between the two. The two ends of the capillary are located inside gas chambers, attached with flexible braided bellows to laser window mounts.

The input and output windows are uncoated elliptical fused-silica (FS) windows, with a thickness of 1 mm. These are mounted at the Brewster angle (maximizing p-polarized light transmission) and glued directly on the mount with epoxy resin. They can withstand a maximum differential pressure of 2.5 bar (experimentally tested).

Optimal mode coupling

The ideal laser focusing geometry is calculated to maximize light coupling to the glass capillary hollow core. This is done by maximizing the overlap integral in between the laser mode in the focus and the fundamental electric hybrid mode (EH_{01}) inside the capillary. The laser is assumed to have a radial Gaussian amplitude profile:

$$E_{\mathrm{G}}(r) = e^{-\frac{r^2}{w_0^2}} \tag{3.6}$$

where r is the radial coordinate and w_0 is the amplitude waist[2] in the focus. The peak amplitude has been normalized to 1 for clarity purposes.

The mode amplitude inside the capillary is represented as a truncated zeroth-order Bessel function of the first kind:

$$E_{\mathrm{B}}(r) = \begin{cases} J_0(r/a), & \text{if } r \leq a \\ 0, & \text{otherwise} \end{cases} \tag{3.7}$$

where $a = D/2$ and $D = 260\,\mu\mathrm{m}$ is the capillary inner diameter.

The overlap amplitude integral η among the Gaussian and truncated Bessel modes is

---

[2] defined as radius

calculated in cylindrical coordinates as:

$$\eta = \int_0^\infty r E_{\mathrm{G}} E_{\mathrm{B}} dr \tag{3.8}$$

This is numerically maximized as a function of the half-width half-maximum (HWHM) of the Gaussian function, which corresponds to the focal waist. This yelds, in terms of transverse intensity profiles, an optimal focal waist $w_0 \sim 83\,\mu m$ for a capillary ID of $260\,\mu m$. From this one can obtain the relationship in between a capillary ID and the laser focal waist that would maximize coupling for Gaussian beams:

$$\frac{w_0}{a} = 0.64, \tag{3.9}$$

where w_0 is the beam waist in the focus and a is the capillary inner radius. For a beam of wavelength λ at a distance z away from the beam waist along the propagation axis, the variation of the spot (radius) size is given by:

$$w(z) = w_0 \sqrt{1 + \left(\frac{z\lambda}{\pi w_0^2}\right)^2}, \tag{3.10}$$

from which the ideal focal length f necessary to couple the beam into the fibre can be derived by finding $w(f)$ that matches the collimated beam spot size. From an experimental point of view, the chosen focal length was $f = 1000\,\mathrm{mm}$, stemming from the input beam profile. A motorized device was purposely built to assess the beam quality across the focus (M^2 parameter, astigmatism, focal waist, ellipticity). A focusing mirror was chosen instead of a lens to minimize chromatic aberration, at the expense of introducing a small astigmatism in the beam by using an off-axis spherical optic. Astigmatism was minimized by using a small incidence angle with respect to the normal for the focusing mirror. The residual astigmatism was precompensated by tilting a predisposed recollimating lens inside the CPA system. The measured beam waist in the focus was $w_0 = 70\,\mu m$. Having a waist smaller than the ideal dimension, an iris was used to clip the collimated beam before focusing to tweak the waist dimension and maximize coupling. The measured energy output of the whole HCF system is $200\,\mu$J, corresponding to a throughput efficiency of $\sim 58\%$. Considering the intrinsically lossy guiding mechanism of the hollow-core glass capillary[3], this is considered satisfactory.

Pulse re-compression

The output of the capilary exibits a predominant positive group delay dispersion (GDD) due to both self phase modulation and normal dispersion inside the capillary [44]. A compression system composed of a set of multilayer chirped mirrors (CM) and two FS wedges was used to compensate the GDD and provide a nearly-FTL pulse. The beam can bounce on the CM an even amount of times (from 0 to 12), with each bounce introducing a GDD of $-40\,\mathrm{fs}^2$. The introduced GDD is fine tuned by the two FS thin wedges (2° wedge), one of which is mounted on a piezoelectric translation stage, which provides a tunable positive dispersion.

Experimental results

The available parameter space in terms of laser power and maximum gas pressure inside the capillary system restrict the choice of the gas medium. Ne was tested as a possible gas

---

[3] the gas core refracting index is lower than that of the surrounding glass, preventing total internal reflection of the guided light and making the coupling very sensitive with respect to any small curvature of the capillary along its full length. The fibre mode is also leaky, further limiting the waveguide throughput energy.

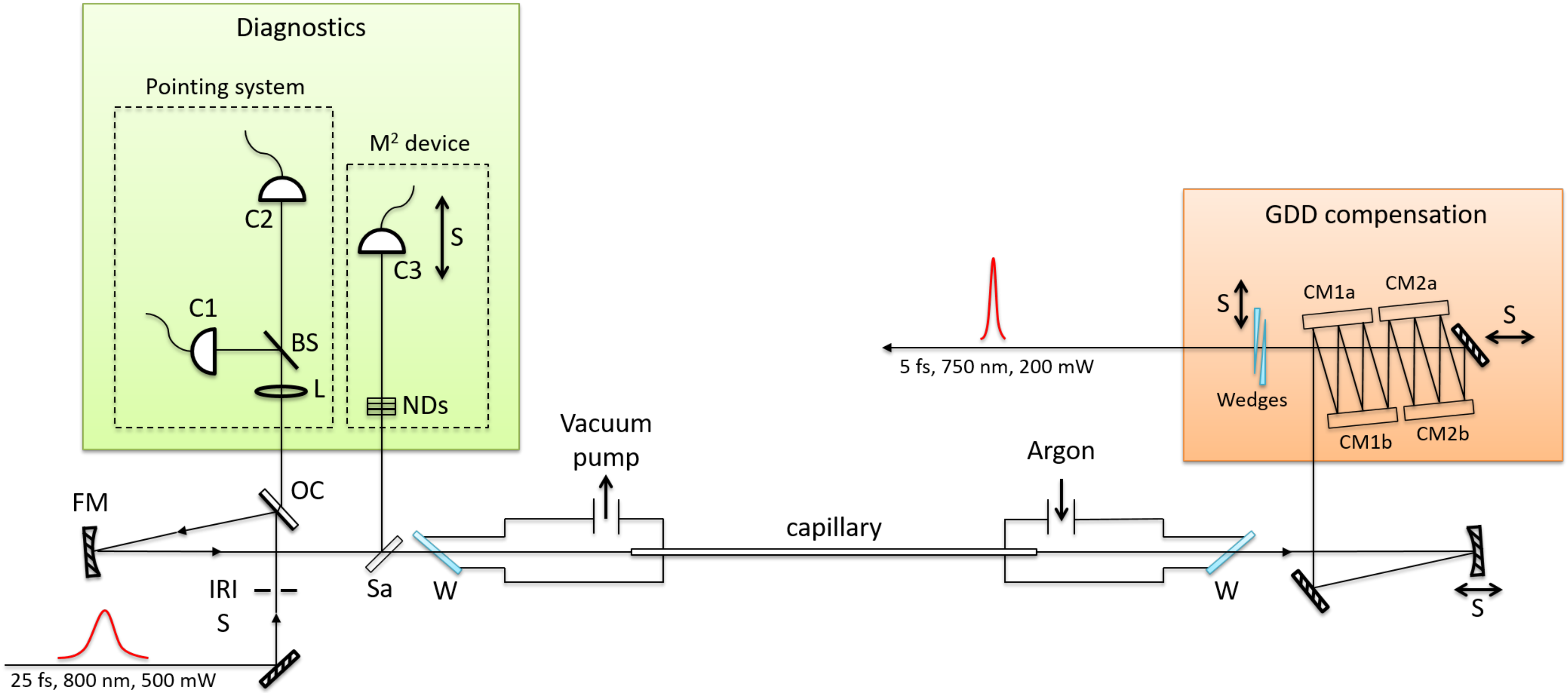

Figure 3.4: Pulse SPM compression system: the CPA output is sent into an Ar-filled (differential pumping) hollow capillary, where the pulses are spectrally broadened through SPM. FM: focusing mirror ($f = 1000\,\mathrm{mm}$); W: Brewster angle FS window, 1 mm thick; OC: output coupler (transmission 1%); Sa: uncoated glass beam sampler (5% reflection), on a flip-mount; S: translation stage. **Diagnostics:** Pointing system: two cameras (C1, C2), located before and after the focus of a lens (L) provide the input beam pointing reference; BS: 50:50 beam splitter. Two motorized mirrors (not depicted in this schematic) located at the CPA output provide the pointing adjustment. M^2 device: a camera (C3) mounted on a software-controlled motorized stage scans the beam focus along its propagation direction. **GDD compensation:** the predominant GDD phase component of the capillary output is compensated using a set of chirp mirrors (CM1a, CM1b, CM2a, CM2b: a & b refer to conjugated phase oscillations introduced by the multi-layer mirrors); two thin glass wedges, one of which is mounted on a motorized stage, provide fine tuning of the GDD by introducing variable positive dispersion.

medium due to the advantage in higher ionization energy (thus limiting plasma formation and consequent disruption at the HCF input), but it proved challenging to deliver pulses with a FTL temporal duration shorter than 10fs, which was not enough for the Raman experiment requirements. Instead, Ar was used in the HCF compressor, which allowed to obtain a sufficient temporal compression. The resulting experimental parameters are the following:

- input power: 360 mW (at the HCF input, after clipping the beam with the iris to fine tune the focal waist dimension);
- pressure: 800 mbar Ar, differential pumping: this was chosen to minimize plasma formation at the capillary entrance, which would disturb the coupling into the capillary and the pulse spectral broadening, providing vacuum on the input side and a linearly varying pressure gradient up to the chosen pressure on the output side.

The output was measured to be 200 mW, corresponding to an energy throughput of $\sim$ 55.6%. As the bandwidth typically spans the $600 - 950$ nm range, the pulse temporal compression can be achieved only in a specific location along the output beam path, as the dispersion introduced by propagating in air cannot be neglected. A measurement of the fully compressed pulse gave a minimum FWHM of 4.5 fs, but on a day-by-day basis the HCF parameters were slightly relaxed to reliably obtain a pulse duration of $\sim$ 6 fs (see Figure 3.5), which is considered satisfactory for the impulsive seeding of vibrating hydrogen (with motion period of 8 fs).

The technique used to measure these ultrashort pulses is Spectral Phase Interferometry for Direct Electric-field Reconstruction (SPIDER). Further details about this technique and the devices used can be found later in this chapter.

3.2.2 Few-cycle second-harmonic generation

The probe pulse is obtained by second-harmonic generation (SHG) from the HCF output in a β-barium-borate (BBO) nonlinear crystal (Crystech), located at the point along the beam path where the seed is temporally fully compressed. The crystal was specifically designed to support most of the bandwidth of the few-cycle NIR pulse, using the code developed by Dr. A. S. Wyatt. This code calculates the type-I phase matching function[28], which governs the intensity of the generated second-harmonic field and is defined as[4]:

$$PMF = \mathrm{sinc}^2\left(\frac{\Delta k L}{2}\right), \tag{3.11}$$

where L is the nonlinear crystal length and Δk is the wave vector mismatch between pump fields and second-harmonic fields

$$\Delta k = k_e(\omega_1 + \omega_2) - k_o(\omega_1) - k_o(\omega_2), \tag{3.12}$$

where ω_1 and ω_2 are frequencies belonging to the driving field (the seed in this case) and $\omega_1 + \omega_2$ are frequencies generated by the material nonlinear response (constituting the probe in this case); the subscripts refer to the ordinary (o) or extraordinary (e) polarization with respect to the crystal optical axis[28]. Aiming at maximizing the generated signal bandwidth, a $20\,\mu m$ thick BBO crystal with an optical axis orientation of 30° was chosen. The SHG experimental setup consists of a 1:1 telescope (using focussing mirrors, $f =$

---

[4] the sinc function is here defined as $\mathrm{sinc}(x) = \sin(x)/x$

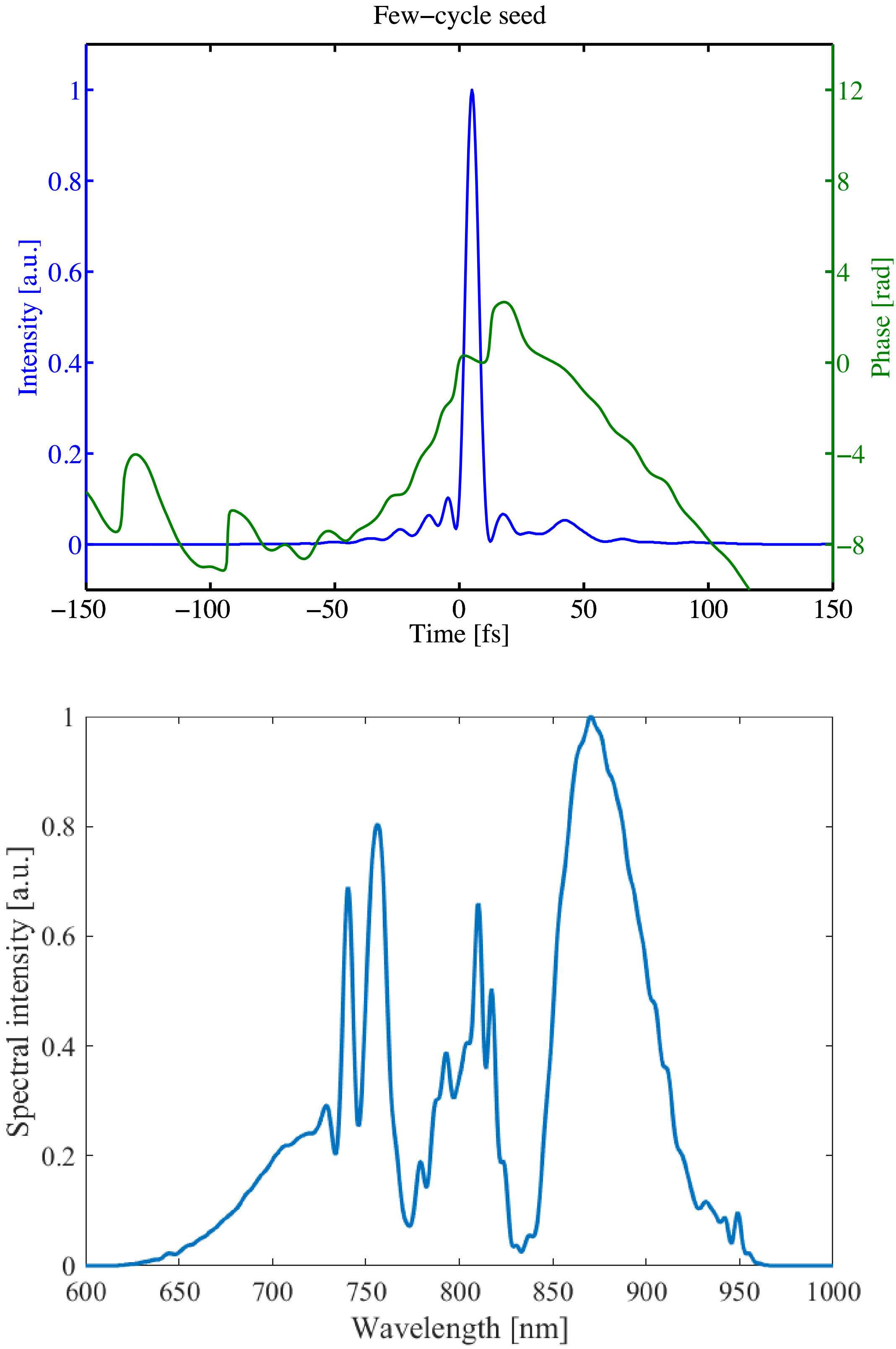

Figure 3.5: Top: seed time intensity (blue curve) and phase (green curve), at the temporal compression location. Temporal FWHM = 6.1 fs. Measured with APE FC-SPIDER. **Bottom:** seed spectral intensity at the temporal compression location. Measured with APE FC-SPIDER.

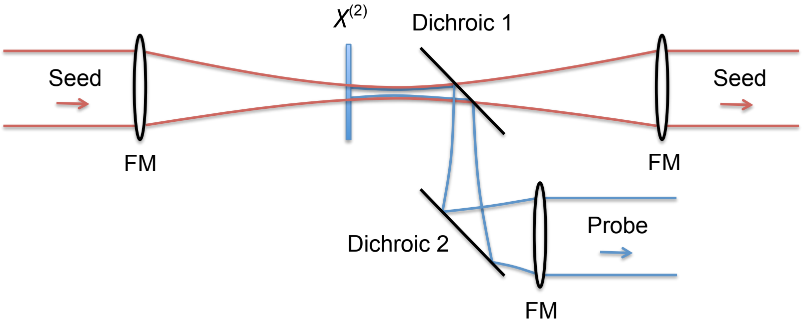

Figure 3.6: Probe SHG setup. $\chi^{(2)}$: BBO crystal; Dichroic 1: Semrock dichroich mirror, cutting wavelength 506 nm; Dichroic 2: Semrock dichroich mirror, cutting wavelength 525 nm (AOI = 0, represented as 45° for clarity purposes); FM: focussing mirror, $f = 1000$ mm (represented as lenses for clarity purposes).

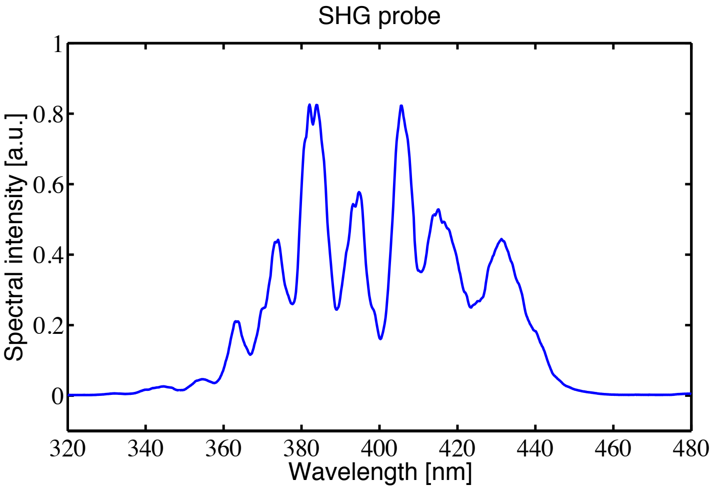

Figure 3.7: Probe spectrum generated via SHG from a 200 mW seed, using a 20 μm, 30° angle BBO crystal. Measured at the Raman cell output using a CCS200 Thorlabs spectrometer.

100 cm) to create an area with a reduced beam spot size and thus higher field intensity. The crystal was located about 15 cm away from the focus to avoid damage (see Figure 3.6). A 200 mW seed generated a 500 μW probe centred around 400 nm, with spectral distribution given in Figure 3.7. The corresponding FTL duration was 7 fs.

3.2.3 Raman cell system

The third element of the laser chain is the Raman cell. The ARNIEMPM technique is applied to molecular hydrogen in a 1 m hollow-core capillary to increase the interaction length tenfold with respect to its previous incarnation, as illustrated in Chapter 2. The Raman cell is based on the HCF system described in 3.2 and modified to accommodate the chosen experimental parameters. This implied redesigning the cell input and output laser windows to support a higher gas pressure (up to 4 bar absolute) and the pulse bandwidths, spanning from the UV to the NIR spectral region. Uncoated, 1 mm FS windows were chosen, to minimize the amount of GDD they impart on the pulses and allow transmission of the full wavelength range. The clear aperture and thickness of the windows was chosen to support the required pressure while inserting as little material as possible in the beam path. They are mounted perpendicularly to the beam, hence a loss of $\gtrsim 10\%$ from the windows surfaces total contribution should be accounted for when calculating the overall throughput efficiency of the Raman HCF. The system layout is illustrated in figure 3.8. The three beams, seed, pump and probe, are coupled into the same HCF. They present diverse wavelength and spatial quality, being effectively three different sources even if derived from the same initial laser. An M^2 device was used again to optimize the focal spot size and position along the propagation axis for all three beams, as already explained in Section 3.2.1. Home built beam pointing control systems have been implemented for each beam. The code and interface had been developed by Dr. A. S. Wyatt and is based on a proportional-integral-derivative (PID) optimization loop[46]. The automatic alignment was used in turn on each beam line independently to align each beam onto a common path that was directed into the fibre. The alignment of the three collinearly superimposed beams into the fibre was manually fine tuned by adjusting the piezo-mirrors in steps equal to their minimum movement. By the use of these diagnostics, the total throughput efficiency[5] reached for the different beams was:

- seed: $\sim$ 40%
- pump: $\sim$ 60%
- probe: $\sim$ 25%

Seed and probe energies do not need to be to high, but just enough to generate and to detect a coherence respectively. Pump coupling is critical since this will determine the final coherence magnitude. The achieved throughput efficiency was considered satisfactory. The delay between the pulses is controlled by a manual stage on the pump beam path and by a motorized stage (Physik Instruments, maximum travel: 30 cm, minimum step: $0.1\,\mu m$) on the probe beam path.

As will be illustrated in Chapter 5, a different implementation of ARNIEMPM with vibrating hydrogen was also attempted, replacing the blue probe with a replica of the seed. In this case the SHG generation system is removed and the probe is derived as a simple replica of the seed via a Michelson interferometer (GDD balanced), where one of the arms contains the motorized stage mentioned previously. Figure 3.9 illustrates the setup. It should be noted that the use of this interferometer reduces the seed power to the 25% of the blue probe case, i.e. both seed and probe will be centred at 750 nm and with an energy of $\sim 5\,\mu$J before entering the Raman cell. The removal of the SHG setup results also in

---

[5] taking into account the aforementioned estimated losses from the cell windows reflections.

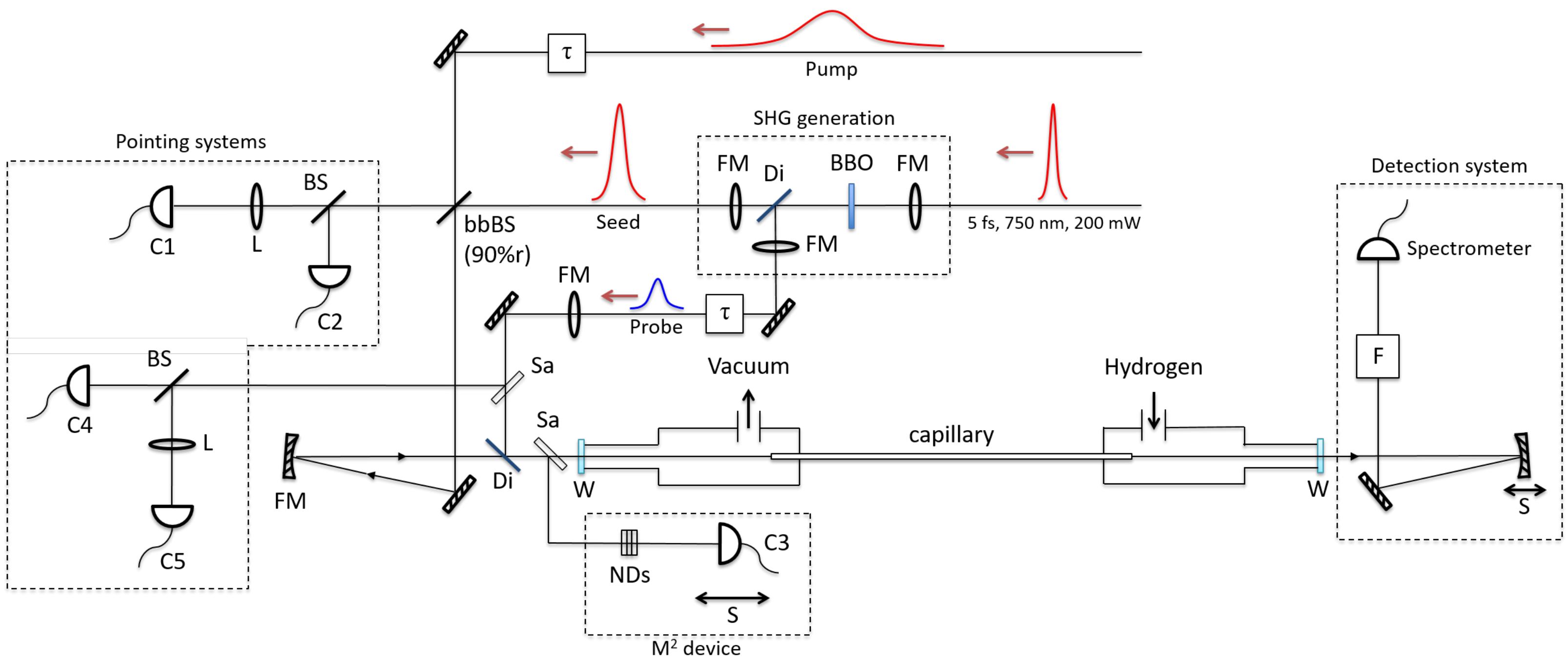

Figure 3.8: Raman cell setup, blue probe: the three beams are recombined using a 90% reflection broadband beam splitter (bbBS) (Layertec) and dichroics mirrors (Di) (Semrock, 506 nm cutting wavelength). The unused output port of the first beam splitter is used for the beam pointing system of the seed and pump, while a separate one is used for the probe. The three pulses are coupled into a hydrogen-filled (differential pumping) hollow capillary. BS: beam splitters; FM: focusing mirrors (sometimes represented as a lens for clarity); W: FS window, 1 mm thick; Sa: uncoated glass beam sampler (5% reflection), on a flip-mount; S: motorized translation stage. **SHG generation:** the 400 nm probe is derived from a 20 μm BBO crystal (Crystech, AR coated, with substrate, custom made), inserted in a 1:1 telescope, near the focus; a dichroich mirror (cutting wavelength 506 nm) is used to separate the probe from the driving seed pulse. **Diagnostics:** Pointing system: CMOS cameras (C1, C2; C4, C5), looking at the beam near and far field by inserting a lens (L) in front of one of the cameras. Piezo-electric mirrors (not depicted in this schematic) located on each of the three beam paths provide the pointing adjustment. M^2 device: CMOS camera (C3) mounted on a software-controlled motorized stage scans the beam focus along its propagation direction. **Detection scheme:** the HCF output is recollimated; a filtering system (F) consisting of a combination of broadband polarizing beam-splitters (FemtoLasers) and spectral filters (dichroich longpass filter, Edmumnd Optics 69889; Thorlabs) provides detection enhancement for a particular pulse or spectral region, according to the different measurement necessities; the main detector is a line grating spectrometer (Thorlabs CCS200)

a reduced GDD. The temporal duration measured before entering the Raman cell is 80 fs, against the ~ 120 fs duration of the blue probe case.

3.3 Measurement devices and techniques

Raman-based spectral modulation

The detection system is aimed towards measuring the spectral modification experienced by the seed, pump and probe pulses. A grating-based line spectrometer (Thorlabs CCS200) with a detection range of $200 - 1100$ nm is used as the main detector, with a combination of cube polarizing beam splitters (Thorlabs PBS012), thin-film ultrabroadband polarizer (Femtolasers), dichroich and longpass filters (Semrock, Edmund Optics, Thorlabs) in different combinations to enhance the signal detection for the 400 nm probe or the pump AS sidebands (see Chapter 4 and 5 for the details about the performed measurements).

Pulse delays

In an experiment involving multiple pulses ordered in a precise sequence the definition of temporal delays needs to be unequivocal. For the remainder of the thesis, the co-moving time frame of the seed pulse is set as the zero delay reference. The relative delays of pump and probe pulse will then be respectively τ_{pu} and τ_{pr} (see fig. 2.4). These have been defined to be positive when the pulses are coming later than the seed pulse, and vice-versa. As all three pulses are derived from the same laser system, the relative delays are defined by measuring each optical path. Experimentally, the $\tau_{\text{pu}} = 0$ condition was set using a fast photodiode (70 ps rise time) and oscilloscope. The oscilloscope was triggered using the

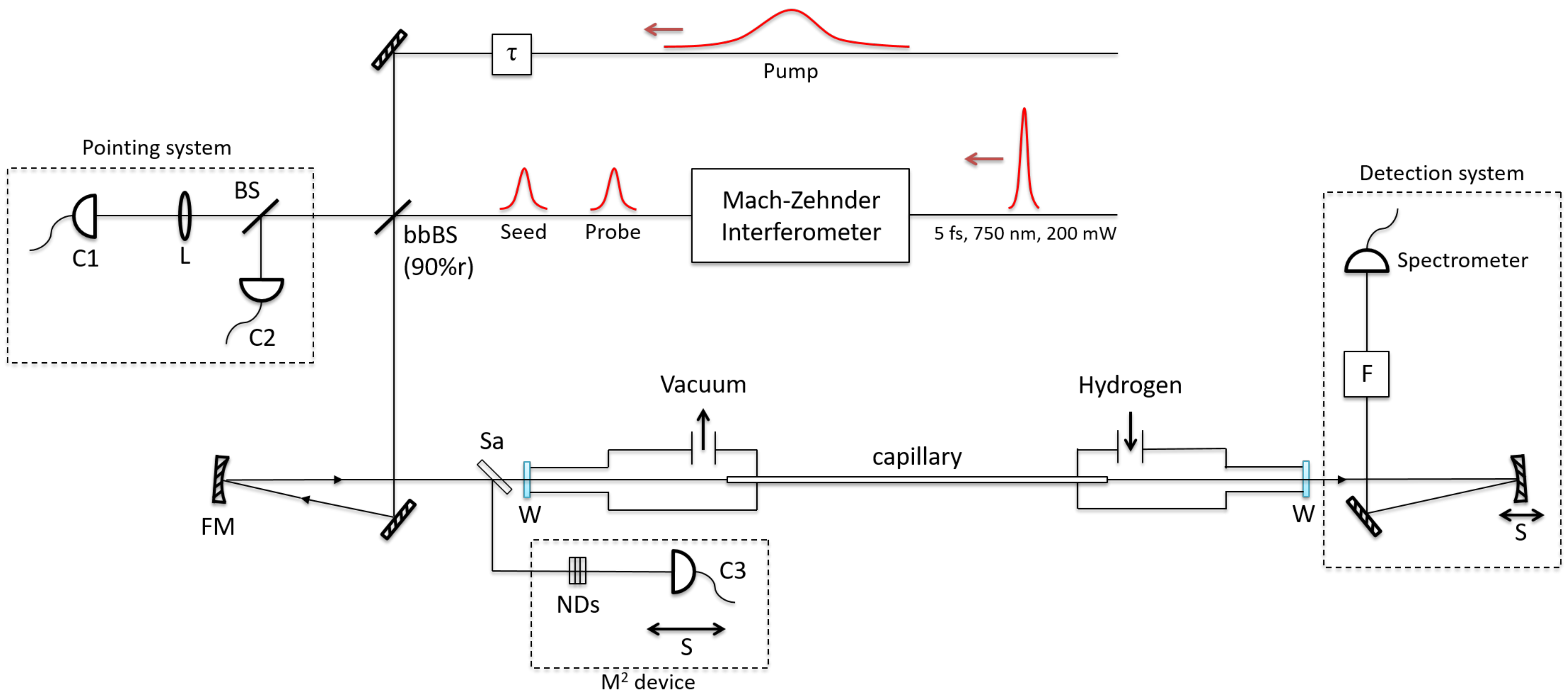

Figure 3.9: Raman cell setup, red probe: the three beams are recombined using a thin broadband 50 : 50 beam splitters (Layertec), for the seed and probe and a 90% reflection thin broadband beam splitter (bbBS) (Layertec) for the collinear seed plus probe and the pump. The unused output port of the first beam splitter is used for the beam pointing system of all the three beams. The three pulses are coupled into a hydrogen-filled (differential pumping) hollow capillary. BS: beam splitters; FM: focusing mirrors (sometimes represented as a lens for clarity purposes); W: FS window, 1 mm thick; Sa: uncoated glass beam sampler (5% reflection), on a flip-mount; S: motorized translation stage. **Probe generation:** the probe is obtained as a replica of the seed pulse, using a Michelson interferometer, GDD balanced; thin, broadband beam splitters are used (Layertec). One of the arms contains the motorized Physik Instrument stage for the control of the probe delay. **Diagnostics:** Pointing system: CMOS cameras (C1, C2), looking at the beam near and far field by inserting a lens (L) in front of one of the cameras. Piezo-electric mirrors (not depicted in this schematic) located on each of the three beam paths provide the pointing adjustment. M^2 device: CMOS camera (C3) mounted on a software-controlled motorized stage scans the beam focus along its propagation direction. **Detection scheme:** the HCF output is recollimated; a filtering system (F) consisting of a combination of broadband polarizing beam-splitters (FemtoLasers) and spectral filters (dichroich longpass filter, Edmumnd Optics 69889; Thorlabs) provides detection enhancement for a particular pulse or spectral region, according to the different measurement necessities; the main detector is a line grating spectrometer (Thorlabs CCS200)

reference signal from CPA from which all the pulses are derived. A manual stage located in the pump beam was adjusted until the peak of the two signals was overlapped on the scope screen. This was double-checked via non-collinear sum-frequency generation (SFG) in a $100\,\mu$m BBO crystal between the seed and pump pulses, where the signal is maximized in correspondence of temporal overlap between the pulses. In the case of the probe pulse, when deriving it as the SHG of the seed pulse the same procedure described above, using photodiode and oscilloscope, was employed. When the probe is a replica of the seed pulse, i.e. with the same bandwidth, the $\tau_{\rm pr} = 0$ condition was identified by measuring the spectral fringes generated by the seed-probe delay on a Thorlabs spectrometer (CCS125), providing a much more precise measurement.

Pulse duration

Multiple SPIDER systems were used to measure the pulse durations at the various stages of the laser chain. A commercial LX-SPIDER from APE GmbH was used to routinely measure the CPA system output and ensure the full pulse compression, providing 25 fs pulses.

The SPIDER technique, first developed by Iaconis *et al.* in 1999[47], is a self-referencing ultrashort pulse characterization technique based on spectral interferometry. Many incarnations of this technique exists, to deal with a diverse range of situations and regimes. The fundamental approach uses a nonlinear medium to generate two replicas of the pulse to be characterized that are ”sheared” (shifted) in spectrum by a small amount. This allows the information about the pulse spectral phase to be encoded in the interference pattern generated by these two pulses. The spectral phase gradient can be deterministically retrieved via

Fourier filtering and then integrated to give the pulse spectral phase. The pulse temporal profile can then be reconstructed via Fourier transform from the pulse spectral intensity and phase.

A home made SEA-SPIDER[48][6] was used during the development of the HCF system to generate the seed pulses and it was later replaced by a commercial FC-SPIDER[7] from APE GmbH. The seed pulse was measured at the SHG crystal location; 50 cm before the Raman cell input; and 100 cm after the Raman cell output. With the SHG system inserted the seed beam path, the measured seed durations at these three locations were:

- SHG crystal location: 6 fs
- pre-Raman cell: 130 fs
- after Raman cell: 220 fs

It should be noted that the pulse temporal structure gets increasingly complex together with the added GDD, with multiple peaks and various features. Hence, the temporal FWHM relevance is reduced the farther we move from the FTL case.

Beam quality

The beam quality and focusing was measured both for the seed HCF system and Raman cell using a homebuilt M^2 device, based on a Thorlabs CMOS camera (DCC1545M) mounted on a motorized stage. The beam pointing was controlled using a commercial KMLabs system (PointLock) in the case of the CPA system output. Multiple Stemmer Imaging cameras

---

[6] SEA-SPIDER: spatially encoded arrangement SPIDER

[7] FC: few-cycle, detecting pulses down to sub-5 fs duration

(IDS UI-1540SE-M-GL) and Newport piezoelectric motorized mirrors (AG-M100N) were used in the case of seed, pump and probe pulses.

Beam power

The beam power was measured with a thermo power meter for the pump and seed beams, while a photodiode power meter was used for the weak 400 nm probe. Day-to-day fluctuations of the CPA system power are $\lesssim 5\%$ of the total output, accordingly affecting the HCF system output and overall performance.

Chapter 4

Material coherence preparation

In this and the next chapter the investigation of the ARNIEMPM approach in a new regime is presented. As discussed in chapter 3, in this implementation of the ARNIEMPM technique we use vibrating hydrogen inside a capillary waveguide as a molecular medium. The main differences of this implementation thus concern the molecular motion exploited (vibrational instead of rotational) and the use of a waveguide to enhance the process efficiency. In particular, the former element puts heavy constraints on the duration of the pulses required to seed the molecular motion, pushing the limits of currently available technology. Practically, this means that some of the assumptions made on the ARNIEMPM first incarnation must be tested here to ensure the validity of the ARNIEMPM theoretical approach.

The three required pulses, seed, pump, and probe are derived as described respectively in 3.2.1, 3.1 and 3.2.2.

This chapter specifically presents the material preparation, with the application of seed and pump pulse only, while the next chapter presents its probing with the full three-pulse train.

The pulses we used have characteristics which put them in a peculiar regime with respect to hydrogen molecular dynamics. The seed in particular (and similarly the probe pulse, as it will be illustrated later in this chapter) has a bandwidth that spans the vibrational energy shift, but is not Fourier-transorm Limited (FTL), i.e. it is temporally stretched beyond the vibrational motion period of $\sim 8\,\mathrm{fs}$. A similar condition can be identified for the pump pulse with respect to the rotational period, which for hydrogen is $\sim 56\,\mathrm{fs}$. These differences from the previous implementation of ARNIEMPM have a clear impact on the results of the seeding, amplification and probing of the molecular motion. It was then decided to experimentally investigate this technique by focussing on three main elements: the new pulse durations with respect to the molecular vibration; the limited available power, due to the presence of a waveguide; the role of dispersion, which thanks to the broadband nature of the pulses used cannot be neglected anymore.

4.1 Coherence preparation

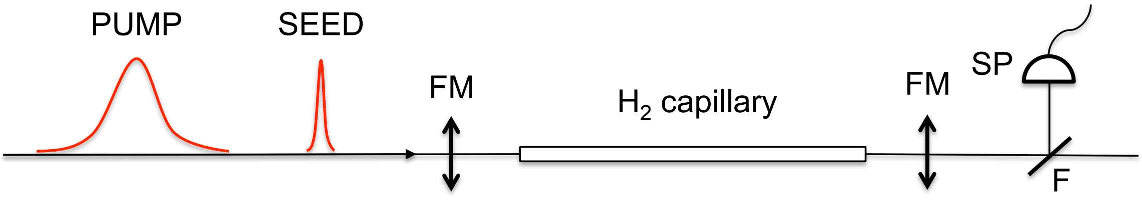

Figure 4.1: Coherence preparation: seed and pump pulse are sent through the hydrogen-filled capillary and their output spectra are recorded. FM: focusing mirror; TFP: broadband thin film polarizer (x2); F: longpasspass filter, 550 nm; SP: spectrometer.

The coherent molecular vibrational motion is prepared and investigated by measuring the output of the Raman cell when only sending the seed and pump pulses through the capillary (see 4.1).

Following from Bustard's initial work on ARNIEMPM[31], the diagnostic chosen to assess the seeding of the molecular vibration is the Raman sideband generation on the pump pulse spectrum: it was demonstrated that, in presence of a seed pulse travelling through the gas sample before the pump, this sideband generation is more efficient. In our case we are considering the vibrational sidebands on the pump with $\sim 30\,\mathrm{nm}$ bandwidth spectrum, centred at $\sim 800\,\mathrm{nm}$ wavelength. The extent of the vibrational frequency shift (125 THz) and the detector used (Thorlabs CCS200, with a detection range of $200 - 1100\,\mathrm{nm}$) restrict the measurement range to the Anti-Stokes sideband spectral region. Table 4.1 presents the Raman sidebands generated from vibrating hydrogen for an initial driving field centred at 800 nm.

sideband	AS5	AS4	AS3	AS2	AS1	λ_0	S1	S2
λ [nm]	300	343	400	480	600	800	1200	2403

Table 4.1: Table of useful Raman sidebands wavelength for an initial wavelength $\lambda_0 = 800\,\mathrm{nm}$. S- and AS- denote the Stokes and Anti-Stokes sidebands respectively. The numbers identify the sideband order.

Pump energy

Figure 4.2 shows the pump spectral behaviour as a function of the input energy, in the unseeded and seeded case. The pump power has been measured before entering the Raman cell and varied in steps of 100 mW through the use of a reflective variable attenuator. In the presence of a seed pulse the AS sidebands become visible. The cell output in this peculiar measurement was reflected from a longpass filter (cutting frequency: 506 nm) to increase the dynamic range of the sideband measurements, resulting in an attenuation factor of ~ 20 for wavelengths higher than 505 nm (covering the pump fundamental spectrum and its AS1 sideband). Despite this, the AS sidebands in the unseeded case are still below the noise threshold for this specific measurement.

Different from the previous ARNIEMPM implementation, figure 4.2 shows how one cannot assume the amplification step to happen in the undepleted pump regime. Considering it is impossible for the detection system used to measure the Stokes sidebands and the limited dynamic range to measure Anti-Stokes sidebands in the unseeded case, the pump depletion seems a good diagnostic to quantify the total energy transfer to the Raman sidebands.

Figure 4.3(left) compares the normalized pump depletion for the unseeded and seeded case: despite the clear difference in terms of AS sideband formation, the energy depletion in the pump fundamental spectrum is rather limited. However, a clear spectral reshaping is visible in the seeded case, implying that rotational Raman modulation is taking place too. This rotational modulation happens in a regime where the pump bandwidth spans the rotational energy shift and its duration stretched well beyond the rotational period by about three orders of magnitude. This disparity is large enough to assume that instantaneously the pump appears monochromatic on the time scale of the molecular rotation, thus it is assumed that no coherent superposition is created in the medium by the pump pulse alone, in both the rotational and vibrational domain. The effect of seeding is more apparent for example by tracking the peak intensity of the fundamental part of the pump spectrum, as illustrated in figure 4.3(right).

From figure 4.3 it can be seen that the contribution of the seeding is rather limited for higher pump powers, with respect to the unseeded case. Considering the trade-off between

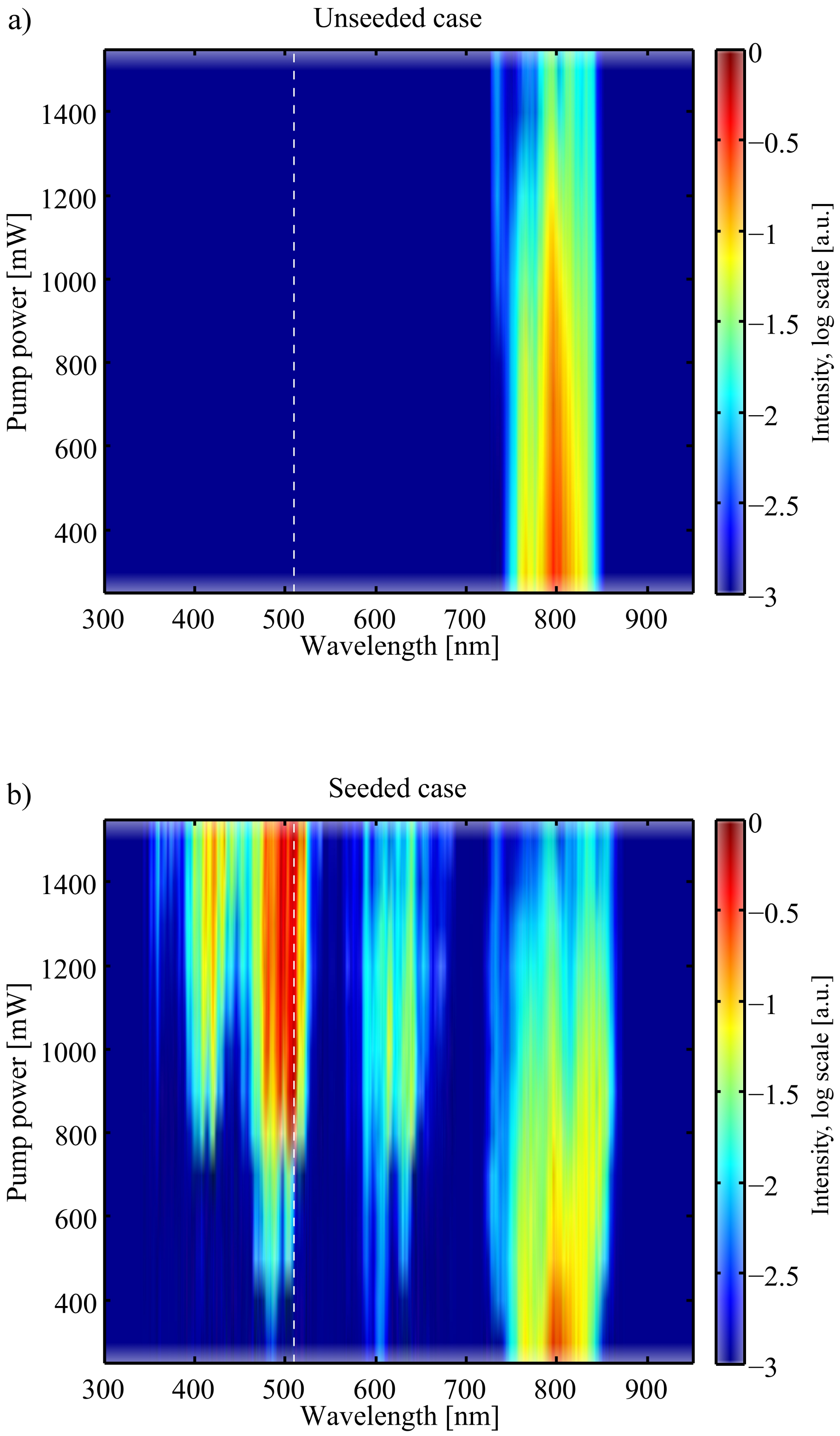

Figure 4.2: Coherence preparation as a function of pump power: the pump pulse spectral intensity (in logarithmic scale) at the output of the Raman cell is plotted as a function of the pump input power, showing the pump residual spectral intensity and AS sidebands (down to AS4). **a)** unseeded case: pump only; **b)** seeded case: pump preceeded by seed pulse. Spectral intensity on the right of the white dashed line is reduced by a factor 20, as the signal is a reflection of a shortpass filter with cutting wavelength centred at 505 nm.

the seeding effect emerging from these measurement and the risk to damage the Raman HCF, the pump power is set at 1000 mW for the remainder of the measurements in this chapter.

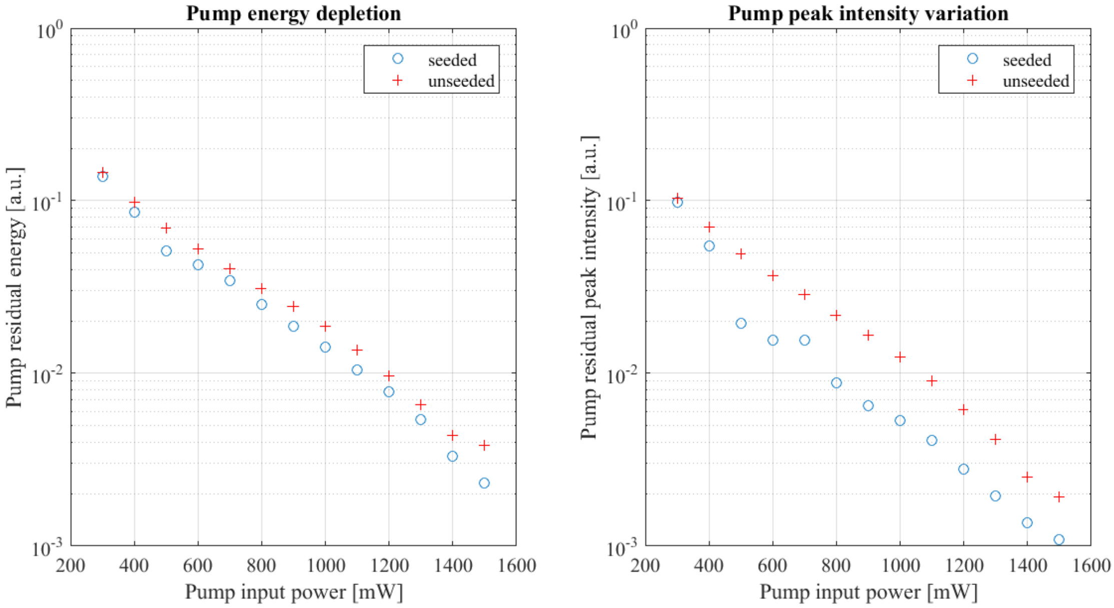

Figure 4.3: Pump depletion as function of pump input power: logarithmic plot of the residual pump energy (left) and peak intensity (right), both normalized with respect to the input pump power, for the seeded (blue circles) and unseeded case (red crosses). The effect of the seed is more apparent in peak intensity plot, as it includes the rotational Raman sideband stimulation in between the limits of the pump input bandwith.

Seed-pump delay

The effect of the seed has been further investigated to confirm its role in initiating the molecular coherence. The delay between seed and pump has been varied, temporally scanning the pulses through each other. After every movement of the delay stage the beams pointing have been adjusted to ensure the beam coupling into the Raman cell HCF is constant. The measurement setup was the same used in the previous section, with the dichroic mirror changed for a longpass filter (550 nm cutting wavelength), used in reflection.

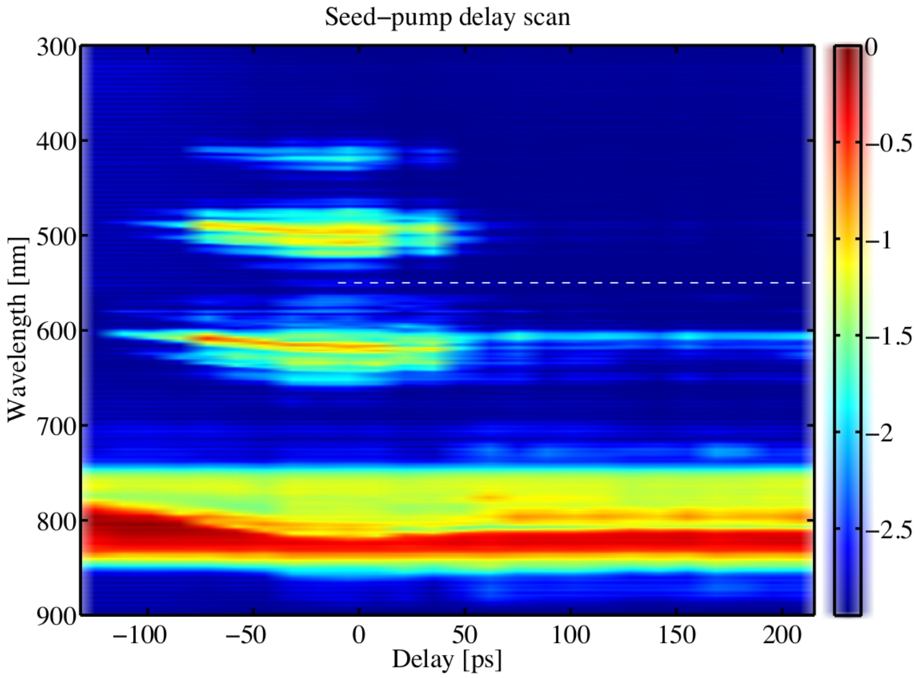

Figure 4.4: Seeding effect as a function of seed-pump delay: recorded spectra of the seed and pump pulses at the output of the Raman cell as a function of the seed-pump delay. As stated in chapter 3 a negative delay identifies a seed pulse arriving after the pump pulse.

As stated in the previous chapter, negative delay corresponds to the seed arriving later than the pump. The pulse zero delay situation corresponds to their temporal intensity peak overlap, with a precision estimated around $+/-10$ ps. Figure 4.4 shows the complete recorded spectral output of the seed and pump while their relative delay is scanned manually over a range of hundreds of ps. Analyzing the behaviour of the AS sidebands and of the pump depletion we can get some insight on the dynamics that are initiated by the seed and pump temporal configuration. Figure 4.5(top) illustrates the behaviour of the AS sidebands energy content as a function of the delay scan. It can be seen how in the region of pulse temporal overlap a large amount of energy is transferred from the pump pulse to its AS sidebands, but when the seed precedes the pump ($\gtrsim 100\,\mathrm{ps}$ range) the AS sideband generation is modest. In particular, only AS1 can still be seen, while the higher order AS sidebands fall below the noise floor. Considering the pump, Figure 4.5(bottom) shows the calculated energy depletion with respect to a pump-only measurement in the $700 - 900\,\mathrm{nm}$ region. We see how the depletion rises once the pulses start overlapping, consistent with the estimated duration of the pump pulse (~ 200 ps). It peaks and starts decreasing, but then remains fairly flat, consistent with the expected dephasing time of vibrational coherence ($\sim 7\,\mathrm{ns}$) once there is no more overlap and the seed precedes the pump.

Three different situations can be identified:

- an unseeded region, when no AS sidebands are measured with the current detection system, the seed comes after the pump and plays no role in any Raman scattering the latter stimulates;
- an intermediate region, when the pulses temporally overlap (-100 to $+100\,\mathrm{ps}$ range) and the pump pulse stimulates cascaded Raman scattering initiated by the seed. It should be noted that the seed plays different roles simultaneously, as it possesses a spectral component ($\sim 600\,\mathrm{nm}$) which stimulates the pump AS1 sideband, while the rest of the spectral components contribute to population transfer to higher vibrational levels;
- a seeded region, when the seed comes before the pump, where the pump stimulates cascaded Raman scattering depending solely on whatever vibrational population situation was left behind by the seed passage.

To better understand this, it is useful to think back to the vibrational levels system of

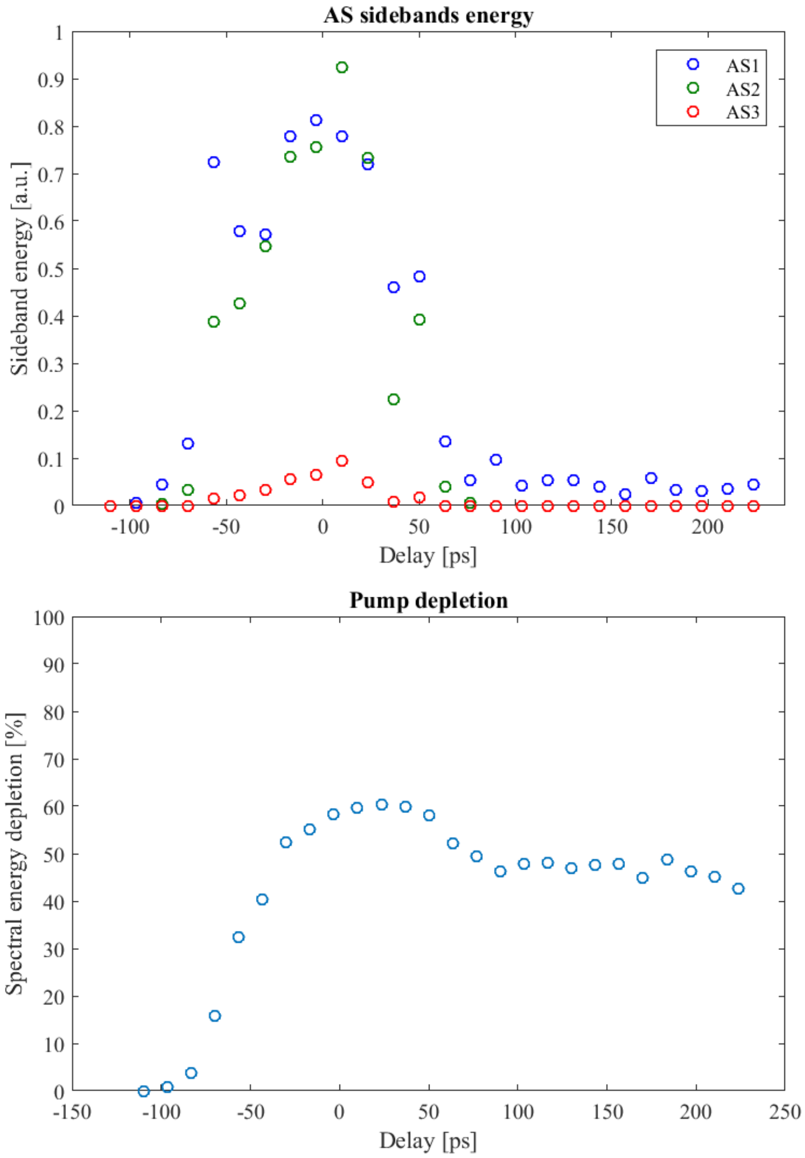

Figure 4.5: Effect of the seed-pump delay on the pump spectrum:top: sideband energy as a function of the seed-pump relative delay. AS1 is reduced by a factor of 10 by the longpass filter used in the detection system (from 550 nm). **Bottom**: (normalized) energy depletion for the pump pulse measured in the $700 - 900$ nm region as a function of the seed-pump relative delay, with respect to a pump-only reference measurement.

molecular hydrogen in these three different conditions, as depicted in 4.6.

From this measurement we can infer some points about the molecular dynamics during the seed + pump coherence preparation process:

- the seed pulse can impulsively initiate the vibrational motion even if not temporally compressed; when pulses are temporally overlapped the sideband generation is much more efficient, suggesting multiple roles played by the seed in both stimulating AS1 emission and in transfer
- the pump energy depletion peaks while the pulses overlap, but experiences a $\sim 20\%$ decrease only when the seed precedes the pump pulse. This suggests that most of the energy is transferred to the Stokes sidebands in this case (and thus that more population is transferred to excited vibrational states, fulfilling the coherence amplification role).

Further investigation into the dynamic of the coherence seeding is needed, to better understand the role played by the temporal stretching of the seed pulse well beyond the vibrational period. Two measurements are performed, to assess if the seed effect is dominated by the AS1 stimulated emission from the 600 nm component or by the impulsive population transfer to higher vibrational levels.

Seed bandwidth

In the first measurement we track the total spectral output as a function of the seed bandwidth, scanning across the vibrational energy gap of $\sim 125\,\mathrm{THz}$, using the same detection setup used in the previous section. As illustrated in the previous chapter, the seed is derived

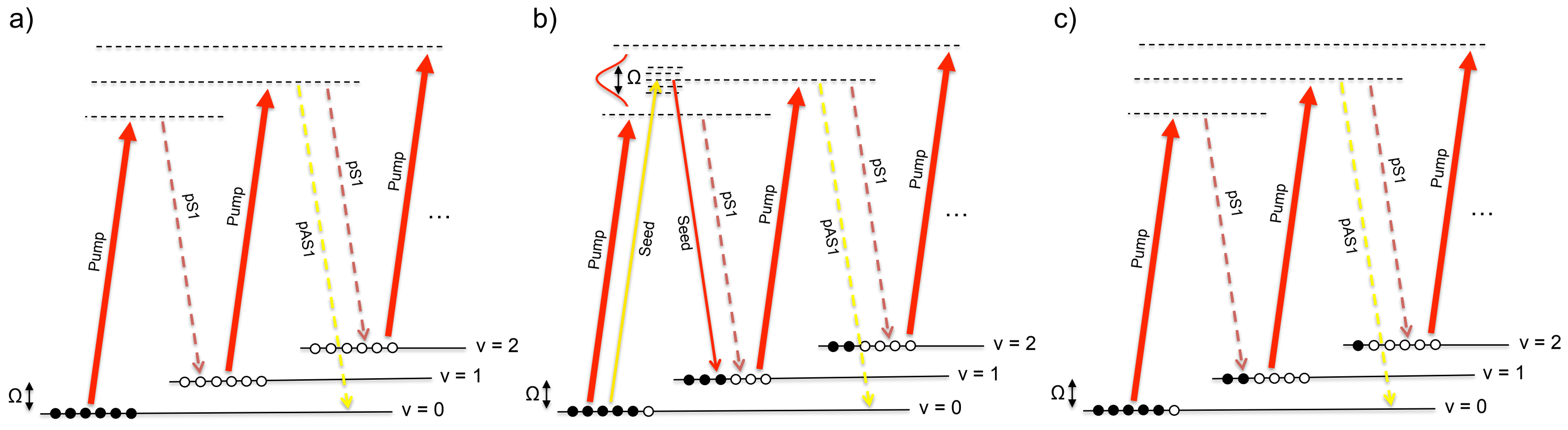

Figure 4.6: Visualization of the different situations identified while scanning seed and pulse relative delay. Pump and Seed identify the two pulse fields, where for the seed the 600 nm and 800 nm components only are represented. pS1 and pAS1 represent the pump Stokes and Anti-Stokes sidebands respectively. Cascading Raman scattering is happening (sidebands down to AS4 are recorded), but sidebands up to 1st order only are represented here. **a)** the pump preceeds the seed, the vibrational level population is fully in the fundamental level and any (cascaded) Raman scattering happens in the transient regime and is due to the pump only; **b)** seed and pump pulses are temporally overlapped, the seed plays the double role of stimulating AS1 and impulsively seeding population to higher levels, which is then amplified by the pump; **c)** the seed precedes the pump: Raman scattering undergone by the pump depends on the population seeded to higher levels by the seed passage, which is limited due to the seed temporal dispersion.

from SPM in a hollow capillary, differentially pumped with typically 600 mbar of Ar. Several different parameters can be used to affect the seed pulse bandwidth without modifying the HCF setup itself, including the input pulse peak intensity or the gas pressure inside the capillary. The setup specifics make it hard to reduce the pressure below 600 mbar with a good enough control, while reducing the input pulse power would reduce the output power enough to hamper the Raman-based part of the experiment. The input pulse peak power has therefore been modified by varying the temporal dispersion on the HCF input pulse, introduced by scanning the CPA output compressor grating separation.

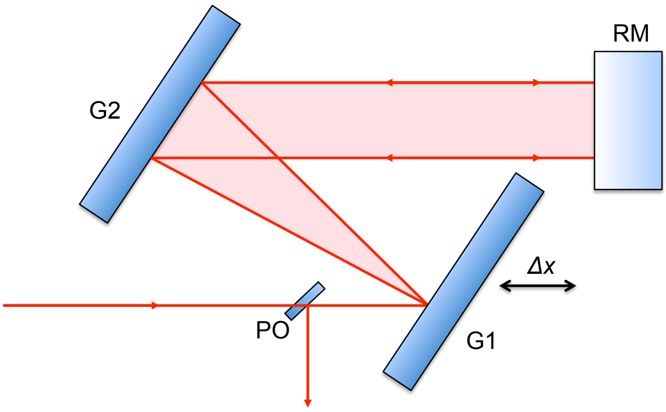

Figure 4.7: Grating movement inside CPA compressor. G1, G2: gratings; RM: rooftop mirror; PO: pick-off mirror.

The first grating in the compressor is moved closer to the second one. The compressor is then undercompensating for the positive dispersion introduced by the CPA stretcher. The HCF input pulse thus has a variable positive GDD[1] estimated in the range $0 - 5550\,\mathrm{fs}^2$.

Figure 4.8 shows the measured output spectrum, here as a function of the seed band-

---

[1] Positive GDD was chosen over negative because of the role it plays in the SPM process, which allows spectral broadening by temporally dispersing the frequency components in time and introducing a positive GDD. An initial negative GDD on the input pulse will eventually cause the frequency components to walk through each other during the SPM process, imposing a complex interference structure on the output spectrum.

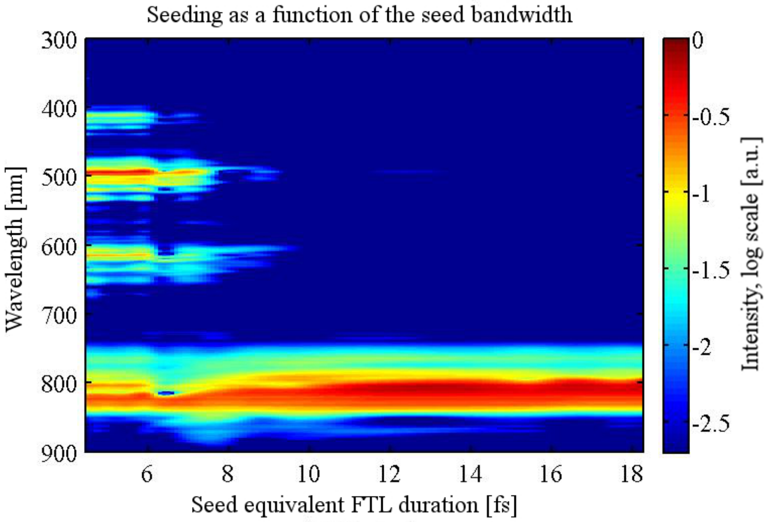

Figure 4.8: Seeding as a function on the seed bandwidth: recorded output spectra in function of the seed bandwidth, quantified in terms of the equivalent FTL duration. Logarithmic intensity scale. Same setup as used in the previous measurements.

width. The AS sidebands are seen to drop below the detection noise floor shortly after the bandwidth equivalent FWHM duration gets larger than the 8 fs vibrational period of the molecular medium. The dip in intensity around FWHM 6.5 fs is an artifact created by the data interpolation. On the raw data a jump in the peak energy is clearly visible, likely due to a drift in the coupling conditions of the first HCF system, which in turn affects the energy and spatial quality of the created seed pulse. Figure **??** shows the recorded spectra for a sample of measured spectra at the input of the Raman cell. (a) presents a sample of measurements with a constant step, plotted for the corresponding translation setting of the CPA compressor grating, as represented in fig. 4.7. (b) presents the same spectral measurements in function of their equivalent FTL duration, calculated from their FC-SPIDER measurements. It should be reminded although that the seed pulses used to seed the process are not temporally compressed at the Raman medium location. Figure 4.10 presents a typical temporal profile of the seed pulse at the Raman cell input.

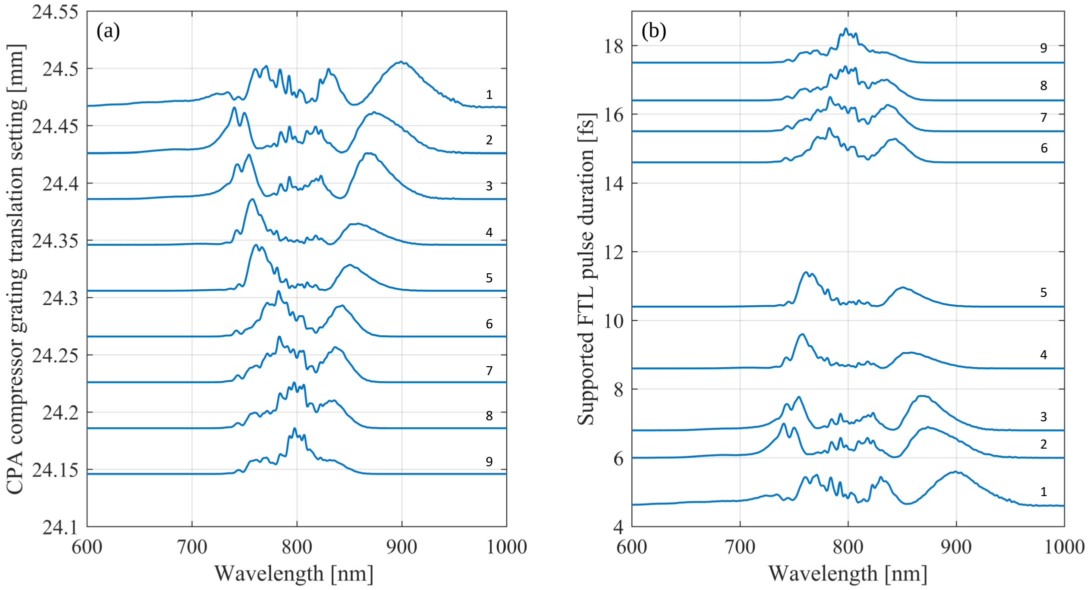

Figure 4.9: Spectral measurement of the seed pulse used to probe the seeding process as a function of the seed bandwidth: (a) a selected sample of spectral measurements plotted against a constant CPA grating translation, measured before the Raman cell input. Same spectral measurements plotted as a function of their calculated equivalent FTL duration. The labels 1 to 9 identify the same measurements in both plots.

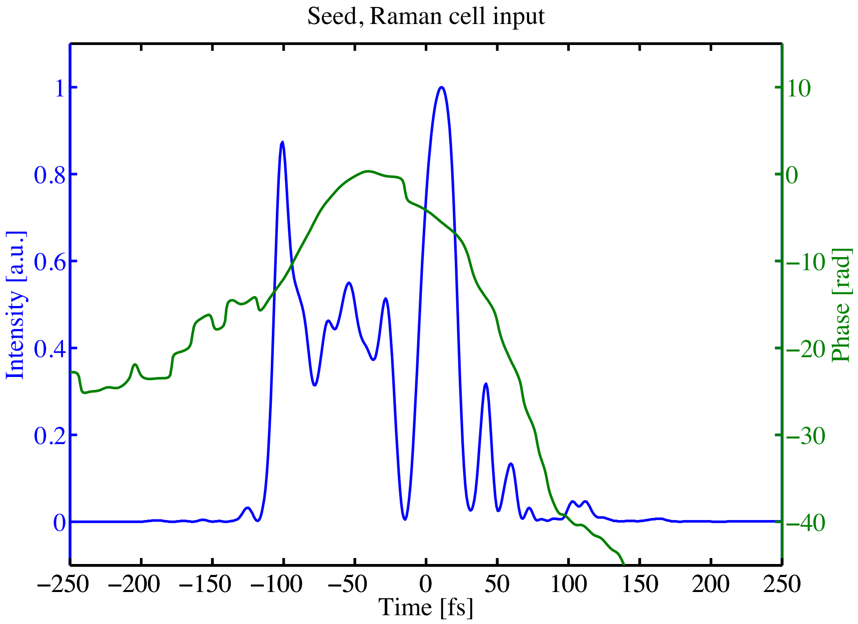

Figure 4.10: SPIDER measurement of the seed at the cell input: seed temporal intensity (blue curve) and phase (green curve), measured before the Raman cell input. 50 cm propagation in air and 1 mm propagation in FS should be added to obtain the seed temporal profile inside the hydrogen-filled capillary.

Double seeding

The second measurement is focussed on testing the regime in which the population is transferred by the seed pulse. The duration of the seed pulse (> 150 fs) falls in the transient regime but the bandwidth hypothetically supports impulsive dynamics, as from the measurements in the previous section we know that the coherence left behind after the seed passage lasts well after the pulse duration and is amplified by the pump. The bandwidth of the seed contains multiple frequency pairs that can drive the Raman transition which are spread in time. If the population transfer is dominated by an instantaneous two-frequency process it is logical to expect an increase in efficiency if these two frequency components are closer in time. In particular, an overlap of the two Raman-shifted frequencies should maximize the population transfer and be reflected by an increase in the measured AS sidebands. I tested this by implementing a double pulse seeding scheme, by inserting a compact Michelson interferometer to create two replicas of the seed and scan their relative delay. The interferometer is balanced in GDD, introducing the same dispersion to both the output pulses: a compensating plate of the same thickness and material (FS) of the beam splitter substrate is inserted in one of the arms (see Figure 4.11). We expect an increase in the sideband generation when the delay matches the instantaneous frequencies of the two pulses ω and $\omega + \Omega$, which for a large enough GDD corresponds to:

$$\Delta\tau \sim \phi''\Omega \tag{4.1}$$

where $\Omega = 125\,\text{THz}$ and ϕ'' is the pulse GDD.

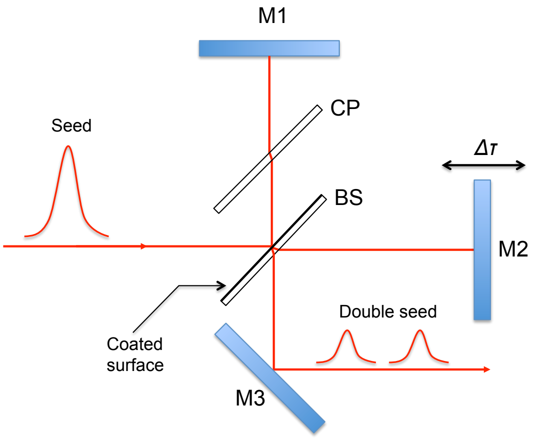

Figure 4.11: Double seed setup: Michelson inserted in the seed path. M1, M2, M3: mirrors; M2 is mounted on a motorized stage; BS: plate beam splitter, reflecting coated surface on the input side; CP: compensating plate.

In my case, the disperison of the pulse is not purely linear and higher order components of the spectral phase will affect the sharpness of the expected peak. A simulation of the double seed effect has been performed (code developed by Dr. Adam S. Wyatt). The vibrational coherence driven by the seed is represented as the two-frequency correlation function, with the correlation separated by the vibrational shift:

$$C(\Omega) = \int \tilde{E}(\omega)\tilde{E}^*(\omega + \Omega)d\omega, \tag{4.2}$$

where the $|C|^2$ represents the excited vibrational level population. The overall effect of the double seed is calculated relative to the FTL pulse case, as:

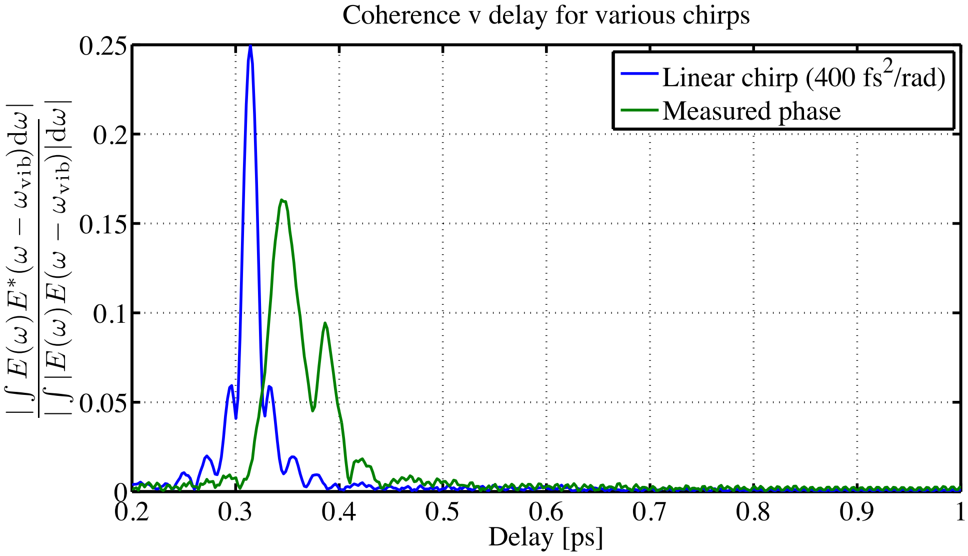

Figure 4.12: Numerical simulations of the coherence versus the double seed interpulse delay: comparison between a purely GDD spectral phase (blue curve) and the measured one (green curve).

$$\mathsf{C}_{\mathrm{norm}}(\Omega) = \frac{\displaystyle\int \tilde{E}(\omega)\tilde{E}^*(\omega + \Omega)d\omega}{\displaystyle\int |\tilde{E}(\omega)||\tilde{E}^*(\omega + \Omega)|d\omega}. \tag{4.3}$$

Figure 4.12 shows the calculated relative coherence variation as the double seed interpulse delay is varied, highlightling the role of the dispersion higher order terms: in one case a purely linear chirp is numerically added to the measured spectrum, while in the second case both the measured spectrum and phase are used. These simulations numerically account for the supplementary propagation (60 cm) in air and through the input window of the Raman cell (1 mm, FS), using the actual pulse that is coupled to the HCF. As expected, the purely GDD case presents a sharp peak in the generated coherence when the delay matches the condition mentioned above, so that the instantaneous frequencies of the two pulses are shifted by the vibrational shift. The realistic case presents a shifted peak position and a much broader peak, due to the spectral phase higher orders of the measured seed pulse. Figure 4.13 compares the calculated coherence in the realistic scenario (using the seed measured with the FC-SPIDER) against the pump AS sideband energy experimentally measured at the Raman cell output. The delay between the second seed and the pump is fixed to 200 ps. The first copy of the seed is scanned over a negative delay range of $0.2-2$ ps with respect to the second, fixed seed copy. The measured energy from AS2 and AS3 shows a peak compatible with the simulations.

The measured double seeding effect is rather limited in comparison with the simulated scenario. Considering this and the 75% power reduction on a single seed pulse due to the interferometer, it was chosen not to maintain the double seed approach and revert back to a single seed pulse scheme for the full ARNIMPM technique.

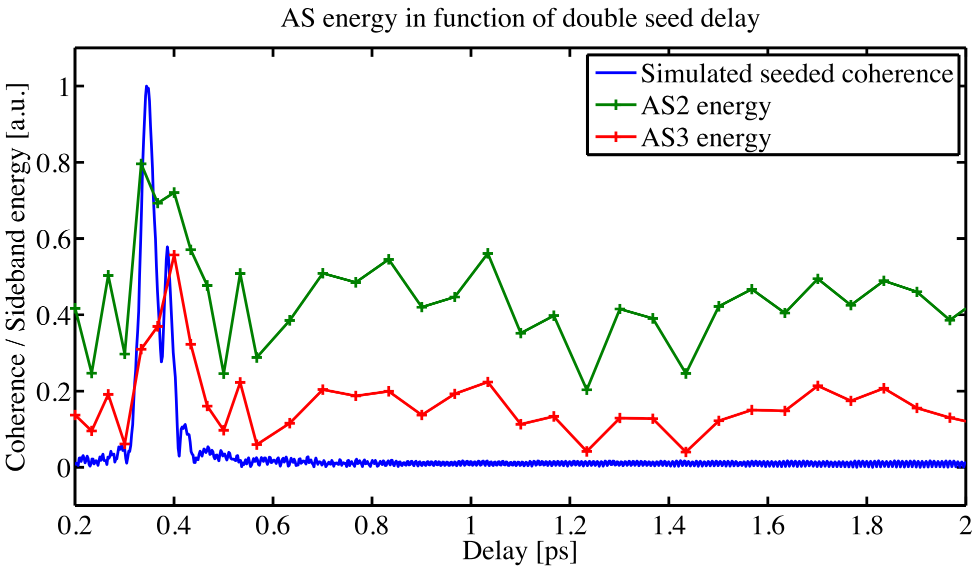

Figure 4.13: Coherence as a function of the two seeds realtive delay: calculated coherence (blue curve) and measured AS sideband energy (AS2, green curve; AS3, red curve) as a function of the double seed interpulse delay. The Measured data shows a peak in the expected position, but the magnitude of the peak is limited with respect to the noise floor.

Chapter 5

Phase modulation measurements

In this chapter I present the molecular phase modulation of ultrashort pulses exploiting the previously illustrated coherent collective molecular vibrational motion preparation. The full three-pulse train is used, with two different choices of probe: a 400 nm probe obtained by SHG from the seed or a replica of the seed itself, obtained by using a Michelson interferometer. The two cases will be denoted respectively as “blue probe” and “red probe”. The investigation is focussed on measuring the spectral modification experienced by each probe. Because of the choice of pulses, in both cases the pump will contaminate the measurements by (partially) overlapping with the probe spectrally: for the red probe case, it will overlap with the input pump spectrum and its AS1 sideband; for the blue probe case, with the pump AS2 and AS3 sidebands.

5.1 Degenerate detection scheme

It is useful to remember once again that the large pulse bandwidths used make it challenging to temporally compress the pulses inside the molecular medium. The dispersion acquired by travelling through 1 m of molecular hydrogen, in a linear pressure gradient ranging from 0 to 4 bar absolute, would chirp the pulse during the propagation. The blue case in particular requires the seed (and thus the generated probe) to be temporally compressed at the nonlinear crystal location, preventing one from achieving temporal compression inside the Raman cell.[1] The estimated durations for the two cases (taking into account the added propagation from the SPIDER measurement location and the Raman cell entrance window) are:

- **red probe case**: seed & probe are replicas of each other, with a duration of ~ 110 fs at the HCF entrance;
- **blue probe case**: seed: ~ 180 fs, probe ~ 150 fs at the HCF entrance.

This prevents truly impulsive modulation of the probe but opens up the possibility for a detection scheme with an improved sensitivity towards any vibrational phase modulation taking place. This approach exploits an interference effect between the chirped probe and its instantaneously modulated vibrational sidebands. This interferometric scheme will be identified as “degenerate” in the remainder of this thesis. Figure 5.1 illustrate this concept

---

[1] A second chirp mirror system could be inserted in the setup to recompress the seed and red probe and a prism compressor could be used to compress the blue probe. These elements would increase the complexity of the system even further and were beyond the achievable targets of this research work.

using the pulse spectrogram, in the form:

$$S(\omega, t) = \int E^{*}\left(\omega' + \omega\right) E\left(\omega' - \omega\right) e^{i2\omega' t} d\omega' \tag{5.1}$$

When a broadband chirped pulse undergoes Raman modulation each instantaneous frequency slice of the spectrum generates isolated sidebands. These sidebands (red outline in Figure 5.1) will gradually shift in time with the driving pulse instantaneous carrier frequency, due to the input pulse GDD. This creates two temporally separated spectral components (blue outline in Figure 5.1), which for a purely linear dispersion have a fixed delay across the whole spectrum, generating an interference pattern. This degenerate scheme has advantages of an increase of the signal-to-noise ratio (through the interference pattern peaks) and the ability to detect the presence of phase modulation even if the generated sidebands are below the noise floor or are in spectrally unavailable areas (as is partly the case due to the pump pulse and pump AS sidebands presence).

A simple numerical simulation has been performed for an ideal case with similar parameters to the red probe experiment, i.e. a broadband Gaussian pulse with a FTL duration of 5 fs, linearly dispersed to a duration of about 100 fs to which a weak oscillating temporal phase (with an 8 fs period) is applied, as if propagating through vibrating hydrogen. Figure 5.2 shows the simulation results comparing the input pulse spectrum with the modulated one, for a FTL case and a chirped case. An interference pattern with a constant period is clearly visible for the chirped modulated pulse case.

For a large chirp, the spectrum is mapped onto the pulse temporal intensity with a

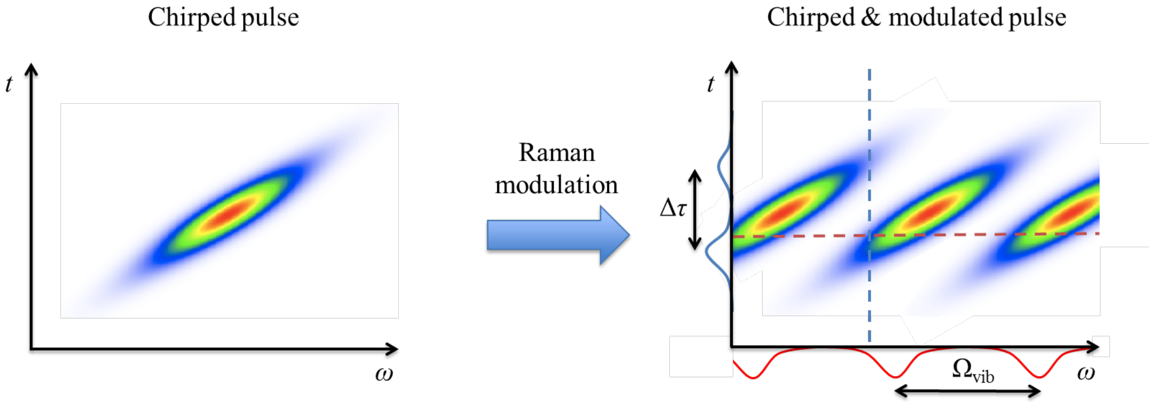

Figure 5.1: Interferometric degenerate scheme concept: spectrograms of the chirped pulse before (left) and after Raman modulation (right). The modulated spectrogram shows the generated AS1 and S1 sidebands with a normalized intensity. The red and blue outlines correspond to the two dashed lines. The red one shows respectively the instantaneous spectrum with the fundamental, Stokes and Anti-Stokes peaks spaced by the Raman shift Ω_{vib}. The blue one shows a single frequency component of the pump and AS1 sideband at a fixed delay $\Delta\tau$.

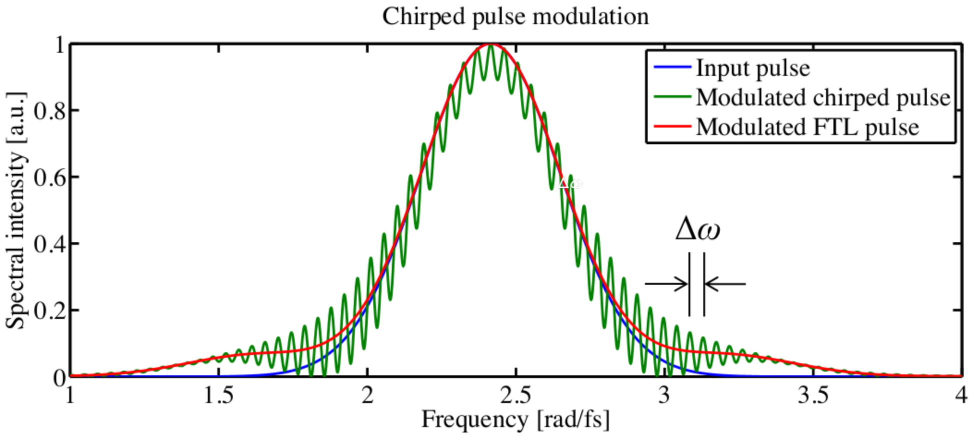

Figure 5.2: Interferometric degenerate scheme simulation: spectrum of input broadband pulse (blue curve) and modulated pulse with oscillating temporal phase: with chirp (green curve) and FTL case (red curve). Parameters used: central wavelength: 800 nm; FTL pulse duration: 5 fs; chirped pulse duration: 100 fs; oscillatory phase period: 8 fs.

scaling factor equal to the pulse GDD:

$$t \sim \omega\phi'', \tag{5.2}$$

where ω is the frequency and ϕ'' the pulse dispersion.

For a pulse with purely linear dispersion a simple relationship can be established between the fringe spacing, the material motion and the pulse GDD. The spectral fringe spacing is

$$\Delta\omega = \frac{2\pi}{\Delta\tau}, \tag{5.3}$$

where $\Delta\tau$ is the delay between the two interfering spectral components. Exploiting equation 5.2 for a fixed Raman energy shift Ω one obtains

$$\Delta\omega = \frac{2\pi}{\Omega\phi''} = \frac{\tau_{vib}}{\phi''}. \tag{5.4}$$

It should be noted that the experimental parameters chosen cause the interference pattern to happen between the driving field and only one sideband at a time, but a larger bandwidth or smaller Raman frequency shift could cause both of them to interfere creating a three-element interference pattern (or more, if cascaded higher order sidebands have sufficient intensity). At the same time, ways to selectively stimulate only one sideband could overcome this problem, for example by exploiting selection rules or polarization filtering (as can be done in rotating hydrogen)[31].

5.2 Molecular phase modulation measurements

5.2.1 Red probe case

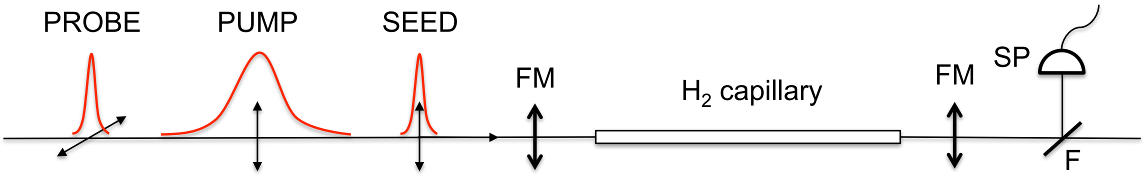

Figure 5.3: Probe phase modulation: the seed (V pol.), pump (V pol.) and red probe (H pol.) pulses are sent through the hydrogen-filled capillary and their output spectra are recorded. FM: focusing mirror; F: broadband thin film polarizer (x2); SP: spectrometer.

The first attempt at phase modulation exploiting vibrating hydrogen is performed on the red probe, a copy of the seed pulse. The seed, pump and probe pulses, in this order, are sent through the hydrogen filled HCF. The Raman cell output was recorded after recollimation with the same spectrometer used in the measurements illustrated in the previous chapter (line spectrometer, $200 - 1100\,\mathrm{nm}$ range). A double broadband thin-film polarizer was used to suppress light from the seed and pump pulses as much as possible, exploiting the crossed polarization between the probe and the seed plus pump. Despite this, the residual pump centred around 800 nm and its AS1 sideband still saturated the detector, due to the long integration times required (hundreds of ms) for measuring the probe with a good signal-to-noise ratio. The delays in between the three pulses were set with respect to the seed, following the convention established throughout this thesis. The pump delay was set to 200 ps to avoid transient effects from taking place when the pulses are overlapped. The probe delay was set to 667 ps, again to avoid overlap and ensure that the coherence preparation contribution is far from the adiabatic regime, lasting after both seed and pump are gone. Figure 5.4 shows the result of 100 sequenced measurements of the probe spectrum with an integration time of 500 ms. The interference pattern generated by the molecular phase modulation is visible across most of the spectrum, with the exception of the areas around the pump fundamental spectrum and its AS1 sideband, respectively centred around 800 nm (2.35 rad/fs) and 600 nm (3.14 rad/fs), indicated by dashed white lines in fig.5.4 (bottom). The presented probe measurement has been obtained by recording the total output of the Raman cell and subtracting the seed and pump case, where the probe is not present. Even after polarization filtering, the residual pump is more intense the probe and saturates the detector. The subtraction is thus imperfect due to energy and pointing fluctuations of the whole system, which have a considerable impact on the Raman cell output, and is responsible for the saturated signal recorded around these two wavelength.

Figure 5.5 shows the effect of the seed on the probe modulation on a single measurement, expanding the spectral section where the interference pattern shows a good visibility. The interference on the probe vanishes when the seed is not present, confirming that the modulation is seed dependent and is thus coherent with respect to the probe, according to the principles of the ARNIEMPM technique confirmed in previous work[19].

5.2.2 Blue probe case

For the second measurement of this chapter molecular phase modulation is attempted for the blue probe case, using the broadband 400 nm probe pulse generated by SHG in a nonlinear BBO crystal from the compressed seed pulse (see Section 3.2.2).The Raman cell output spectrum was recorded after recollimation using the same setup as the red probe case (double broadband thin-film polarizer and spectrometer), with an added longpass filter in reflection (cutting wavelength 550 nm) used to further reduce the seed and pump residual

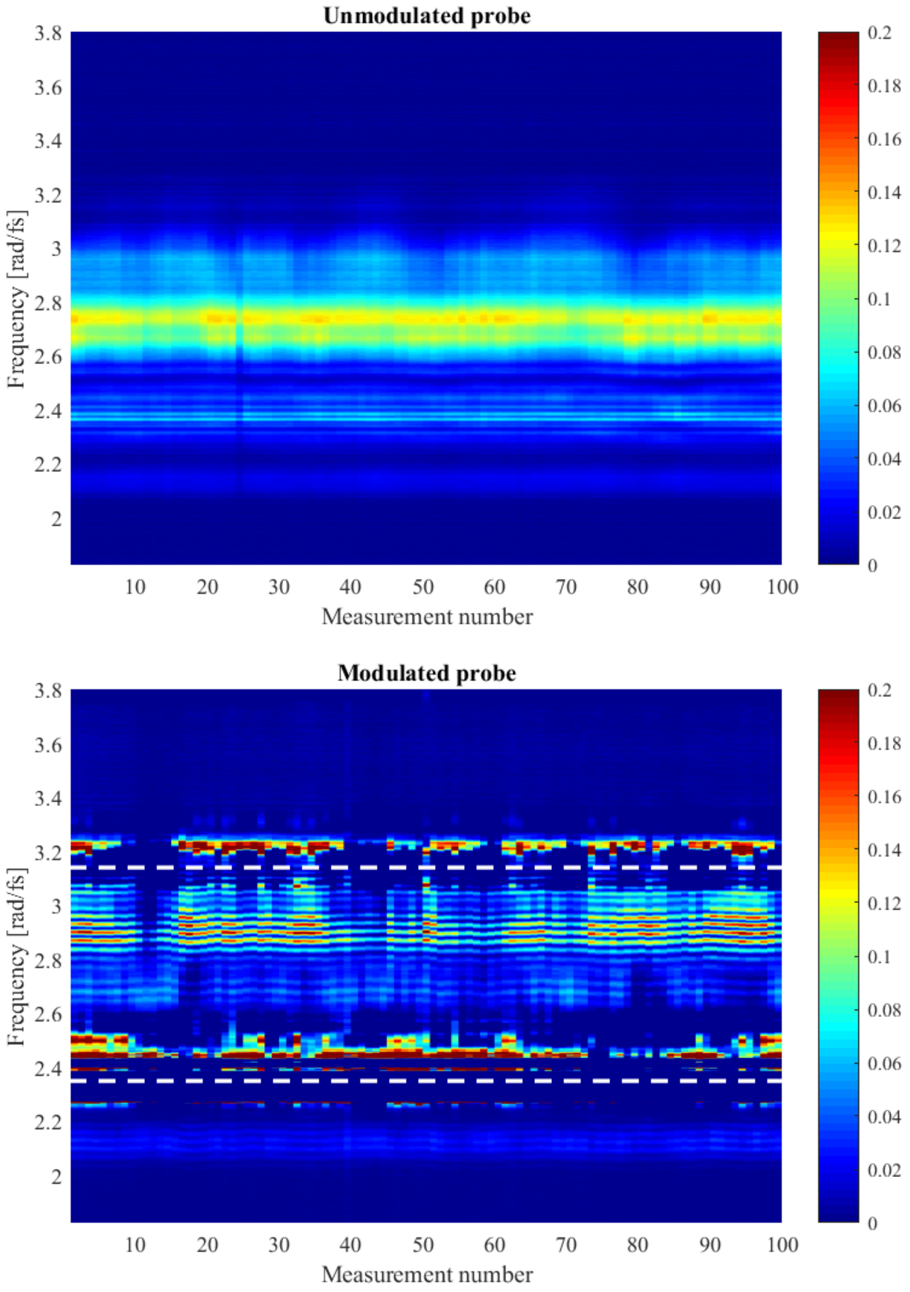

Figure 5.4: Red probe modulation: spectrum of the probe pulse, measured at the Raman cell output, for multiple samples. **Top:** probe without coherence preparation (i.e. no seed and pump). **Bottom:** modulated probe, all pulses present; the interference generated by the molecular modulation is clearly visible. The dashed white lines represent the position of the pump fundamental and AS1 central frequencies (respectively 2.35 rad/fs and 3.14 rad/fs, corresponding to 800 nm and 600 nm), at which the probe signal detection is disturbed due to an imperfect background subtraction.

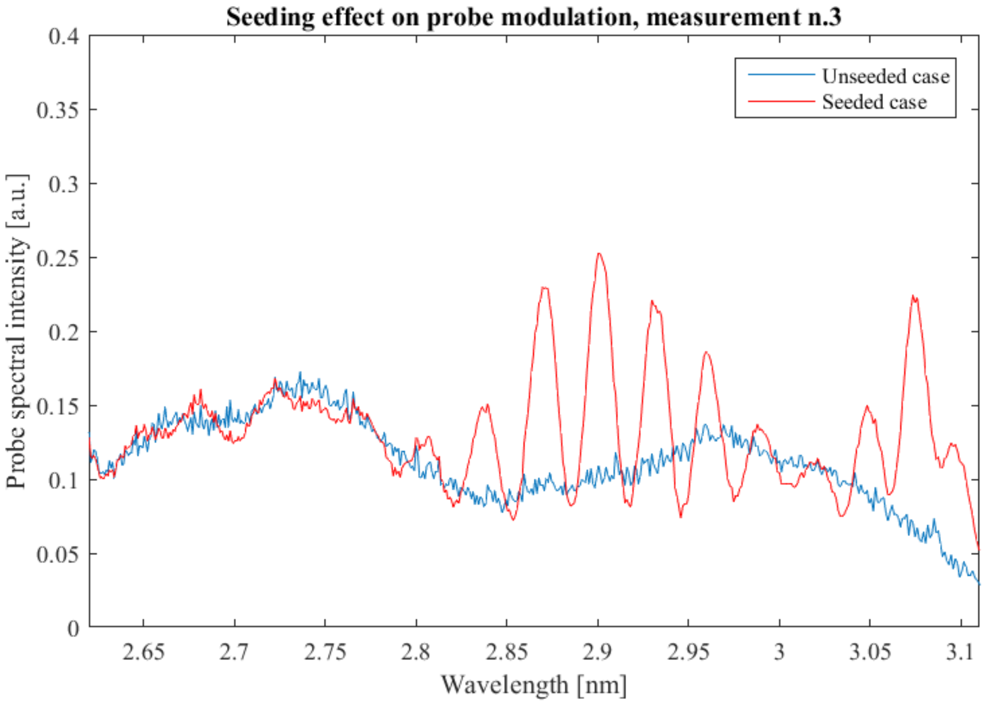

Figure 5.5: Seed effect on probe modulation: Unseeded case (blue line): measurement of the Raman cell output when using pump and probe only (an independent measurement of the seed has been added to maintain the total energy unchanged). Seeded case (red line): Raman cell output when using all the three beams. When the seed is not present, the modulation on the probe vanishes, confirming the coherent seeding of the molecular motion. (Measurement n.3 from fig.5.4)

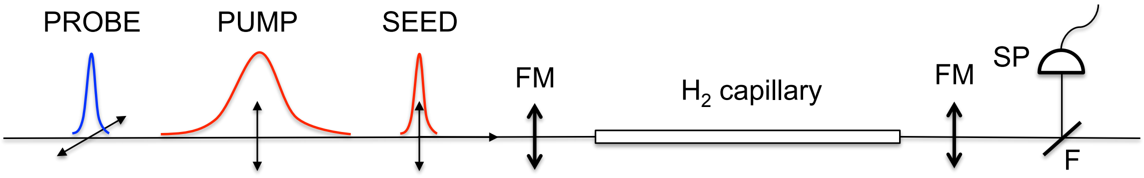

Figure 5.6: Probe phase modulation: the seed (V pol.), pump (V pol.) and blue probe (H pol.) pulses are sent through the hydrogen-filled capillary and their output spectra are recorded. FM: focusing mirror; F: broadband thin film polarizer (x2) + longpass filter, 550 nm; SP: spectrometer.

signal by a factor of 20. This measurement proved particularly difficult as the leakage from the pump AS3 is degenerate with the probe central wavelength (400 nm) and the pump AS2 covers exactly the area where the probe S1 is expected (480 nm). The degenerate interferometric detection technique is the key to characterize the modulation, but further problems are present. The data show wide intensity fluctuations especially for the pump and its AS sidebands which saturate the detector and preventing any meaningful measurement being achieved. This is likely due to beam pointing and coupling issues, as the Raman HCF must be carefully adjusted manually to maximize the blue probe coupling into the HCF at the expense of the seed and pump coupling efficiency. Spectral and power instabilities from the seed HCF may also affect the pump AS sidebands and are seen to cause changes in the probe spectrum over time, so that the differential measurements between data taken at different times (e.g. over several hours) have a limited usefulness. Figure 5.7 shown the recorded spectrum of the probe at the output of the Raman cell, while blocking the seed and pump pulses before the input. This is the initial spectrum recorded when attempting phase modulation in the blue probe case.

The measurements performed intended to find evidence of the blue probe phase modulation by comparing the case of a probe coming after the seed & pump pulses (approximatively 233 ps after the seed) or before (approximatively 133 ps before the seed), with the seed and pump delay fixed to ~ 133 ps). It was decided to post-select the spectral measurements to isolate and use the samples in which the pump AS3 (which strongly fluctuates in intensity) was absent or weak enough to not affect the probe spectral measurement in a relevant way, by comparing them with the pulse spectrum alone.

Figure 5.8 shows the result of multiple measurements of the probe spectrum, for the

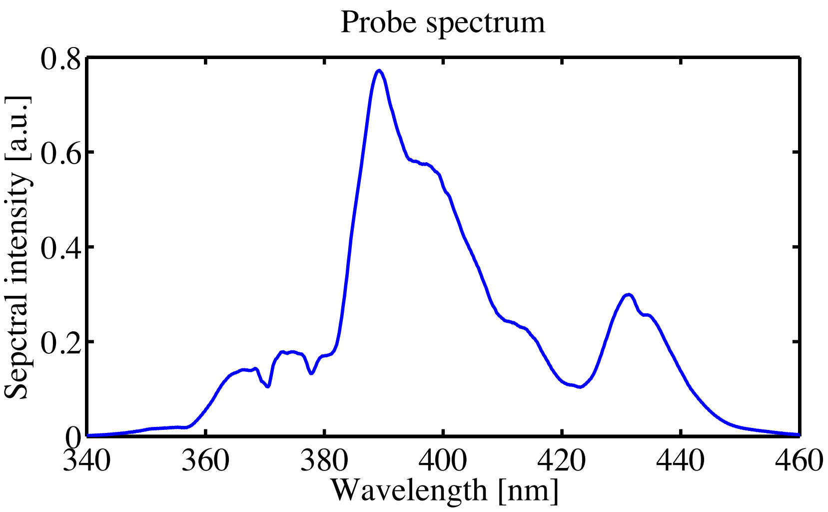

Figure 5.7: Probe spectrum: used for the blue probe case modulation measurements, recorded at the Raman cell output. Seed and pump blocked before the input.

modulated and unmodulated case. For the former case, of 1000 total samples, less than 100 resulted to be usable becasue of the pump AS3 fluctuations, limiting the relevancy of the data, but further investigation to obtain better data was not feasible due to time constraints. Nevertheless, the interference pattern generated by the molecular phase modulation is faintly visible across most of the spectrum (10% visibility approximatively). There is also a certain reshaping of the probe spectum, but there is insufficient data to confirm if it originated from the phase modulation and not from a drift in the seed spectrum generating the blue probe. Figure 5.9 shows the comparison between the modulated and unmodulated cases, averaged over all the post-selected samples. The weak interference pattern is clearly present, but the averaging process reduces the fringe visibility.

5.2.3 Phase matching concerns

On top of the stability issues of the whole laser system, which appear worse for the blue probe setup, another effect is limiting the modulation available for the blue probe. In the

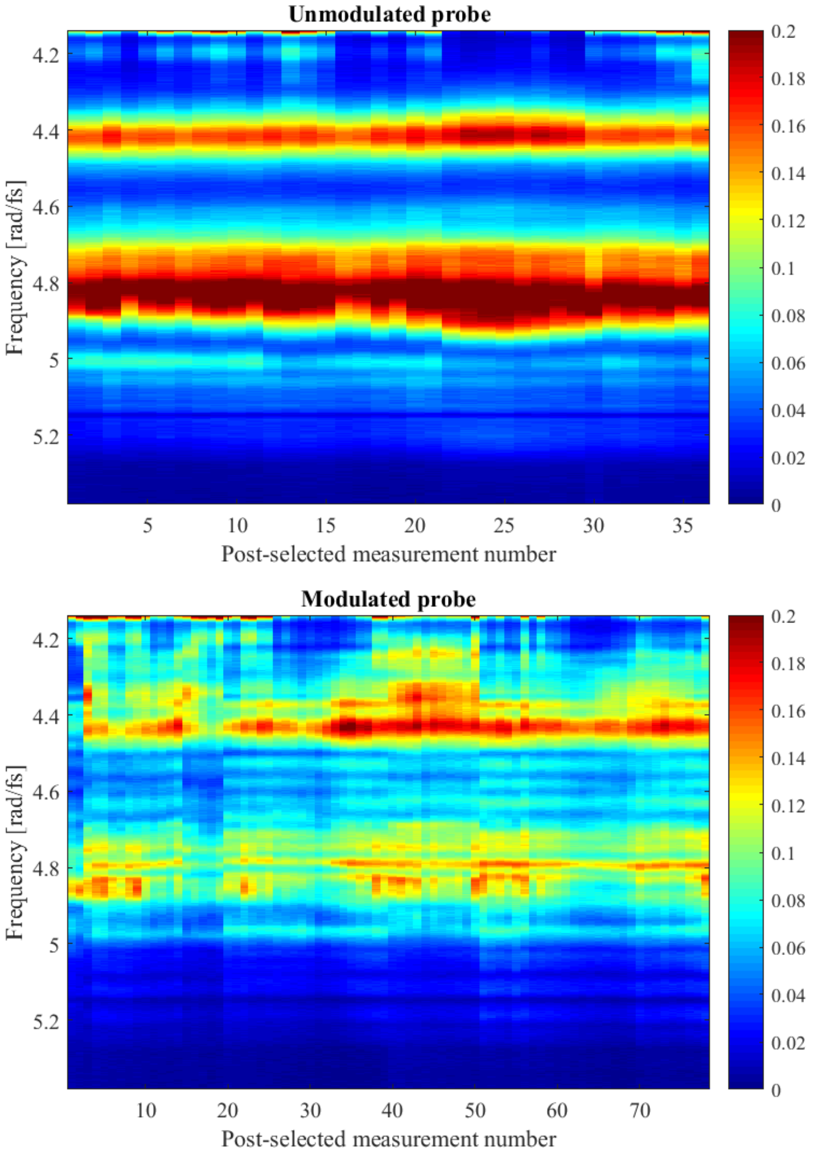

Figure 5.8: Blue probe modulation: probe spectrum measured at the Raman cell output, multiple samples (postselected to exclude AS3 leakage overlapped with probe spectrum). **Top:** probe propagates through the molecular medium before seed and pump (delay: ~ -133 ps from seed). **Bottom:** probe propagates through the molecular medium after seed and pump (delay: $\sim +233$ ps from seed); the interference generated by the molecular modulation is faintly visible. The system instabilities and fluctuations affect the quality of the data, preventing a strong indication of phase modulation.

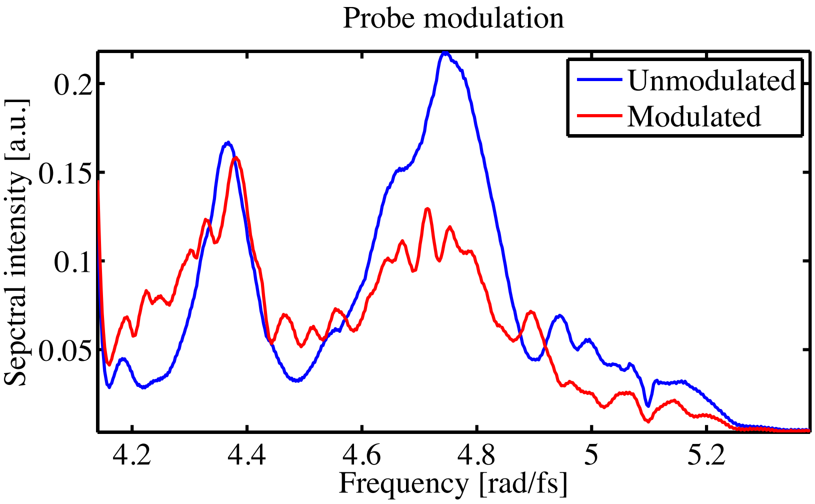

Figure 5.9: Probe spectral modulation: averaged over the post-selected data, comparison between the negative delay case (blue curve — probe comes first, no coherence preparation) and the positive delay case (red curve — probe comes last, after coherence preparation). For the positive delay a hint of an interference pattern is visible.

previous implementation of the ARNIEMPM technique the extent of the bandwidths involved, both in terms of Raman energy shift and pulse spectra, allowed one to neglect any phase-matching constraints between the generated material coherence and the probe pulse propagation through the sample[31]. Moreover, that approach was not using any waveguide, thus the interaction length was estimated to be limted to the Rayleigh range of the beams involved (a few centimetres), making any phase matching problem even less relevant. My implementation of the ARINEMPM technique is radically different in this and linear dispersion is what was identified as a potential main protagonist for poor vibrational modulation on the probe. This becomes even more relevant with the use of a HCF to increase the interaction length of the Raman phase modulation phenomenon, strongly limiting the usefullness of this approach. The phase-matching condition between the 400 nm probe and the Raman coherence generated by a 800 nm pulse can be characterized by the phase-slip length, i.e. the propagation distance over which the fields and material coherence fall out of phase. We follow the approach already used in the initial ARNIEMPM implementation by Bustard[31], which relates to the work of Nazarkin *et al.*[49] and Yariv[50]. This model provides the basic calculations for a probe with fixed propagation speed inside a medium with a fixed coherence amplitude. Relating to Equation 2.59, i.e. the slow varying envelope quantity $Q_{ij}(z,t)$ defined for the ARNIEMPM model in Chapter 2.3 to define the molecular coherence, one can assign a wave vector to the excitation as $k_{\mathrm{Q}} = k_{\mathrm{pu}} - k_{\mathrm{S}}$, with the pump and Stokes fields having different phase velocities in presence of dispersion. The above-mentioned approach by Nazarkin gives the Raman medium excitation between two levels (1 and 2) as

$$\rho_{12}(z,t) = -i|Q_0|e^{i[\Omega t - k_{\mathrm{Q}} z]} \tag{5.5}$$

where Q_0 is the maximum coherence value and Ω is the vibrational frequency shift. The probe wave-equation is

$$\left(\partial_z + \frac{1}{v_{\mathrm{pr}}\partial_t}\right) A_{\mathrm{pr}} = i\beta_{\mathrm{pr}}\mathrm{sin}\left[\Omega t - k_{\mathrm{Q}} z\right] A_{\mathrm{pr}}, \tag{5.6}$$

where v_{pr} is the group velocity of the probe in the molecular medium and $\beta_{\mathrm{pr}} = \frac{N\alpha_{12}\omega_{\mathrm{pr}}|Q_0|}{2\epsilon_0 v_{\mathrm{pr}}}$. After transforming coordinates $(z', \eta_{\mathrm{pr}}) = (z, t - \frac{z}{v_{\mathrm{pr}}})$ equation 5.6 can be integrated to give

$$A_{\mathrm{pr}}\left(L, \eta_{\mathrm{pr}}\right) = A_{\mathrm{pr}}\left(0, \eta_{\mathrm{pr}}\right) \exp\left\{i\delta^{\mathrm{mod}}\left(L, \Delta k\right) \sin\left[\eta_{\mathrm{pr}}\Omega + \frac{\Delta k}{2}\right]\right\}, \tag{5.7}$$

where

$$\delta^{\mathrm{mod}}(L, \Delta k) = \beta_{\mathrm{pr}} L \mathrm{sinc}\left(\frac{\Delta k L}{2}\right). \tag{5.8}$$

The wave-vector mismatch is

$$\Delta k = \frac{\Omega}{v_{\mathrm{pr}}} - k_{\mathrm{Q}}. \tag{5.9}$$

Equation 5.7 shows how the modulation depth δ^{mod} is now a function of the wave-vector mismatch[2]. A characteristic quantity can be identified, the phase-slip length, $L_{\mathrm{slip}} = 2\pi/\Delta k$. This quantity defines the length range over which phase modulation will take place efficiently and plays a central role when using a waveguide to increase the interaction range, as in my experiment. The presence of the waveguide adds also a contribution to the wave-vector mismatch. Follwing Korn *et al.*[51], a plasma-like (i.e. negative) term can be added when calculating a field wave vector to account for this contribution, so that the total wave vector for a generic spectral component can be written as

$$k(\omega) = k_0(\omega) + k_{\mathrm{n}}(\omega) - k_{\mathrm{w}}(\omega). \tag{5.10}$$

The three elements in 5.10 represent respectively the vacuum contribution ($k_0(\omega) = \omega/c$); the medium contribution

$$k_{\mathrm{n}}(\omega) = \frac{\omega}{c}(\omega) N\alpha(\omega), \tag{5.11}$$

where N is the molecular density and $\alpha(\omega)$ the polarizability; and the waveguide contribution

$$k_{\mathrm{w}}(\omega) = \frac{u_{11}^2}{\pi D^2}\frac{2\pi c}{\omega}, \tag{5.12}$$

---

[2] the sinc(x) function is defined as $\sin(x)/x$

where u_{11} is the first root of the Bessel J_0 function and D is the waveguide diameter. Including the wavelength contribution in 5.9, the phase-slip length has been calculated for my experiment for a gas pressure range of 1 to 4 bar, as the Raman HCF system has a pressure differential from 0 to 4 bar over the 1 m length of the capillary. Figure 5.10 shows the calculated phase-slip length for the current experimental setup with waveguide diameter of 200 μm and a hypothetical 35 μm diameter fibre The red and blue probe case are shown, comparing the case in which the waveguide contribution is taken into account or neglected. It can be seen how a smaller diameter could potentially cancel any detrimental effect of the dispersion on the Raman modulation process, setting the phase mismatch to zero for a given pressure.

The calculation of the phase-slip length, especially for higher pressure, seems to suggest an efficient interaction region limited to a few cm, which would render the HCF almost useless. The dispersion seems to have a larger detrimental effect on the shorter wavelengths, thus it should affect the blue probe case more. This is in agreement with the experimental results, where the modulation in the blue probe case is weaker than the red probe case. Two further elements should be considered. Following Bustard's calculations[31] we know that most of the Raman modulation takes place towards the end of the interaction region. This coincides with the higher pressure part of the capillary (thanks to differential pumping), where we expect the vibrational Raman effect to be dominant over the rotational. Considering these, one can expect the dispersion effect on the vibrational modulation depth to be mitigated by the presence of the capillary. In general, the waveguide contribution could be used to reduce and possibly counterbalance the dispersion detrimental effect simply thanks to the term $k_{\mathrm{w}}(\omega)$ sign in Equation 5.10, but in my case the core diameter is still too large

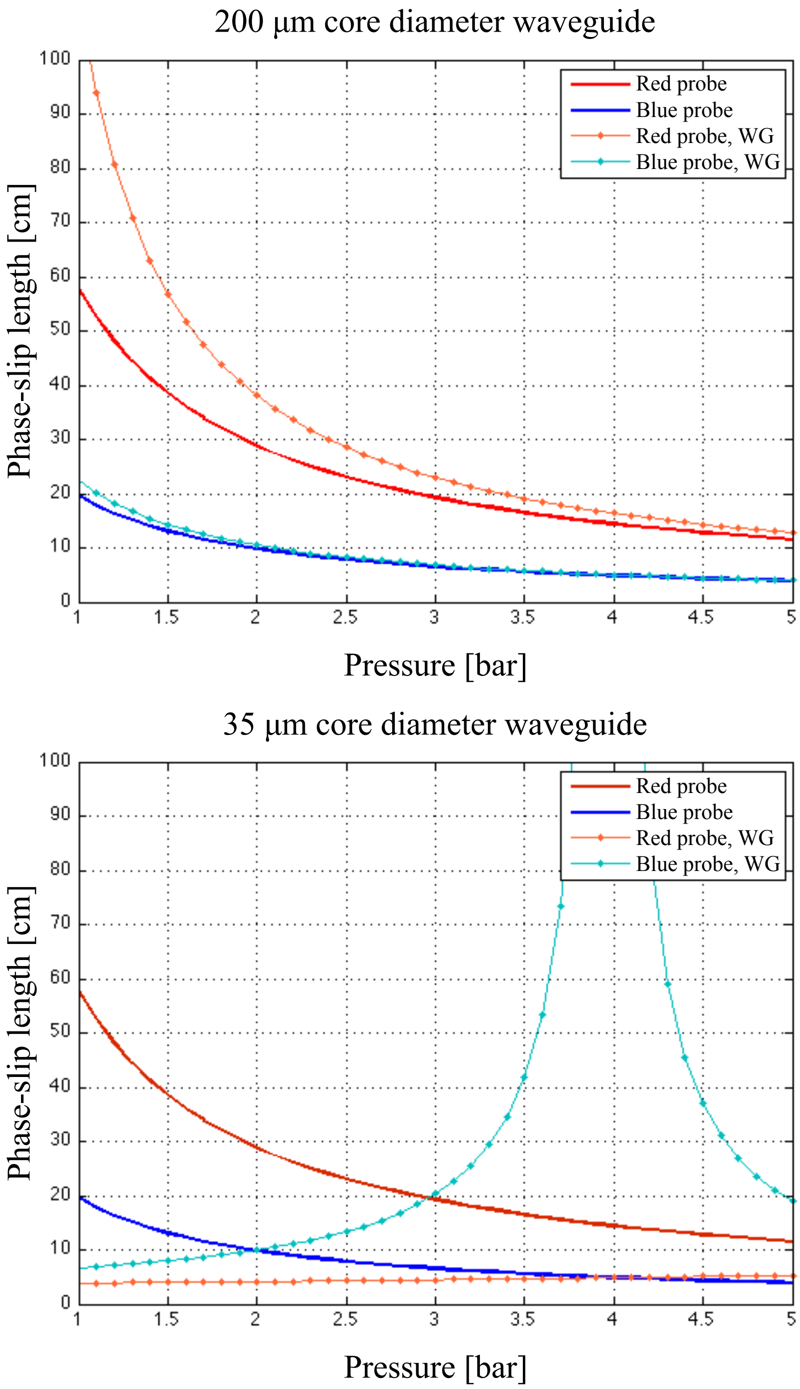

Figure 5.10: Phase-slip length calculations: the phase-slip-length has been calculated for the red and blue probe cases, assuming a pump centred around 800 nm, for a 200 μm core diameter, similar to the experimental case (top) and an hypothetical 35 μm core fibre (bottom). The solid-dotted lines refer to when the waveguide contribution is taken into account, while the solid-smooth lines account for equation 5.9 only.

to play a relevant role. By using smaller waveguide core diameters ($< 50\,\mu$m diameter for example) one could obtain a more drastic impact, but exploring this option was beyond the scope of this thesis. It should also be noted that other problems will arise in this case, linked to the intrinsically lossy guiding mechanism of a hollow-core guide and the resulting limited throughput efficiency for the pulses used.

In conclusion, in this chapter I presented the experimental evidence of vibrational molecular phase modulation of broadband probe pulses centred around 800nm, using a degenerate interferometric detection scheme, after the coherence preparation investigation presented in the previous chapter. Experimental results indicates that there could be modulation of broadband probe pulses centred at 400nm too, but the data quality is too poor to be able to confirm that. This is due to experimental limitations inherent to the chosen setup and available parameter space. Dispersion effects are considered to be the main limiting factor in reducing the effective interaction between the blue probes and the coherently moving molecular medium, but the calculations presented show that it should be possible to easily overcome this by using different waveguides of smaller inner core diameter.

Chapter 6

Arbitrary waveform characterization

The Raman interaction between pulses and matter is an active tool in the field of ultrafast optics, enabling the delivery of tailored laser probes for the investigation of ultrafast dynamics in atoms, molecules and solids through spectral modulation and broadening[14].

In time-resolved spectroscopic studies of these ultrafast phenomena, equally important to the generation of the correct probes is the ability to fully characterize them. The electric field, as a fundamental element of Maxwell's theory of electro-magnetism, contains all the information of classical fields in free space. In the case of ultrafast spectroscopy the electric field time variation is faster than the electronic response of any available detector and thus needs to be retrieved by other means.

Historically, a toolbox of techniques has been developed to characterize ultrashort pulses indirectly, reconstructing the pulse time structure by measuring it in the more accessible Fourier domain (i.e. the spectral one). By measuring the pulse spectral intensity and phase, a pulse can be reconstructed via Fourier transform. Various strategies, based on interferometric, spectrographic, sonographic and tomographic methods have been developed over the years, playing a pivotal role in the development of ultrafast sources and their application. Walmsley *et al.* wrote a comprehensive review of pulse characterization, which will provide the reader with a structured overview of these methods[52].

Among the numerous approaches to determine the pulse mode structure of light, the most successful are probably the interferometric Spectral Phase Interferometry for Direct Electric-field Reconstruction (SPIDER)[47,53] and the spectrographic Frequency-Resolved Optical Gating (FROG)[54,55]. The SPIDER technique is based on encoding the spectral phase of the pulse in the spectral interference pattern generated by two delayed copies of the initial pulse, to which a small frequency shift is typically added by sum-frequency generation (SFG) in a medium possessing a $\chi^{(2)}$ nonlinearity. The Takeda algorithm[56] is then used to extract the spectral phase from the measured interferogram, allowing a deterministic reconstruction of the pulse temporal profile via Fourier transform. The FROG technique is based on obtaining a spectrogram of the pulse by SFG in a nonlinear medium of two replicas of the input pulse while scanning their relative delay. An iterative process based on the principal component generalized projection algorithm (PCPGA)[57,58] is used to retrieve the pulse which best matches the measured spectrogram.

Multiple implementations of these and other techniques exist for dealing with a wide range of experimental conditions, but they possess some intrinsic limitations:

- none of these directly measures the electric field, with no information for example on the Carrier-Envelope Phase (CEP);
- they all usually require a nonlinear medium to act as a time-nonstationary filter, which limits the bandwidth and sensitivity for broadband pulses;

- they are unable to characterize pulses with large spectral gaps (larger than any isolated spectral section);
- they are not performed *in situ* (i.e. the location of the pulse interaction with a medium, for example) but at a different location; the additional propagation from the light-matter interaction needs to numerically be accounted for when retrieving the real pulse at the measurement location.

These issues are even more detrimental when considering pulses which are manipulated by interaction with Raman-active media. The capability to synthesize complex pulses and waveforms is directly linked to the large (hundreds of THz) bandwidths involved (as in the work presented in this thesis) and could involve the stimulation of isolated Raman sidebands over a wide wavelength range[38]. The synthesis of complex pulses has recently been a widespread push in the field of ultrafast optics[26,59,60], putting the requirements for pulse characterization beyond reach of the mentioned techniques.

A different approach consists of directly measuring the electric field, accessing all the available information about the pulse and overcoming most of the issues associated with indirect approaches. Two techniques exist at the moment with this capability, attosecond-streaking[61–63] and the petahertz optical oscilloscope[64]. Both techniques rely on high-harmonic generation (HHG) as a temporal gate which is fast enough to sample the electric field variation, directly in time.

Attosecond streaking is based on using an attosecond pulse to generate photoelectrons and shifting their momentum (streaking) with the field of the pulse to be measured (the "test pulse"). A temporal delay scan of the two pulses maps the test pulse electric field onto the momentum shift, allowing its reconstruction.

The petahertz optical oscilloscope, developed by Kim *et al.*, is an all-optical technique based on measuring a pulse by crossing it at an angle with an intense pulse driving HHG. This results in the spatial deflection of the generated extreme-UV (XUV) field in a macroscopic sample according to the field of the test pulse. A temporal scan of the pulses relative delay maps the test pulse electric field inside a macroscopic sample to this deflection, allowing the test pulse reconstruction.

In this chapter a I will present a novel technique developed in collaboration with the groups of Prof. J. Marangos and Prof. J. Tisch from Imperial College, London. This technique is called Attosecond Resolved Interferometric Electric-field Sampling (ARIES). It is an all-optical technique and presents some advantages with respect to the work developed by Kim *et al.*, namely: the beams are collinear; it exploits a single atom response instead of a macroscopic effect; it does not require a spatially-resolving detector to track the XUV light deflection; it uses the HHG spectral intensity only. The technique is based on generating a HHG spectrum from the superposition of an intense HHG driving field, which is identified as the "probe pulse" (PP) and the pulse to be measured, identified as the "test pulse" (TP). By scanning the relative delay between the two pulses, the instantaneous field is destructively or constructively modified. This variation is mapped directly to the highest energy generated by the HHG process and can be tracked to reconstruct the field of the test pulse.

In the remainder of the chapter I will present the basics of HHG necessary to understand our technique; the ARIES approach; the experimental setup used in its first implementation; the experimental results and some numerical insight to better understand the technique.

My involvement in this work was mainly focussed on the experimental campaign performed at Imperial College, the results discussion and paper preparation. Multiple people collaborated to this project: the initial idea was developed by Dr. A. S. Wyatt; the experimental work was performed by myself and Dr. A. S Wyatt from Oxford, and D. Fabris and Dr. T. Witting from Imperial College. The data analysis, simulation and plotting code was developed by Dr. A. S. Wyatt. Further theoretical in-depth analysis has been developed by Dr. A. S. Wyatt and Prof. J. W. G. Tisch. Prof. I. A. Walmsley, Prof. J. P. Marangos and Prof. J. W. G. Tisch provided supervision.

6.1 High-harmonic generation basic principles

Initially a complementary of Raman scattering-based techniques[17,49,65] in the quest for the generation of attosecond pulses, HHG has imposed itself as the standard technique both to provide the shortest laser probes available (80 as) and as a way to access atomic and molecular dynamics at this unprecedented timescale by studying the generated radiation.

HHG is the result of the interaction between an extremely short and intense laser field with an atomic gas (or less commonly a molecular gas, a plasma or a solid). The process takes place outside the perturbative regime of nonlinear optics, acting on the outer bound electrons through a highly nonlinear process. Many approaches are used to describe HHG. The basic concept underlying this phenomenon can be understood with the simple semi-classical model developed by Corkum[66], depicted in Figure 6.1. This is commonly known as the three step model: *1)* an intense ($10^{13} - 10^{15}$Wcm^{-2}) optical pulse modifies the atomic potential enough to allow the bound electron to tunnel through (or directly pass over) the binding potential barrier; *2)* the electron is freed from the atomic potential and can be considered a classical free particle, which oscillates in the applied optical field, increasing its energy; *3)* the electron, still driven by the field, may return to the parent ion and recollide, generating radiation proportional to the sum of the energy gained during the excursion in the continuum and the ionization energy. More rigorous approaches take into account quantum mechanical models and the macroscopic propagation of the field, but the simplicity of the ARIES allows for the use of the simple semi-classical model of Corkum. A more detailed approach, based on the single atom response and known in the literature as the Strong Field Approximation (SFA) will be briefly illustrated in the last section of this chapter, when a deeper understanding of the ARIES technique is sought.

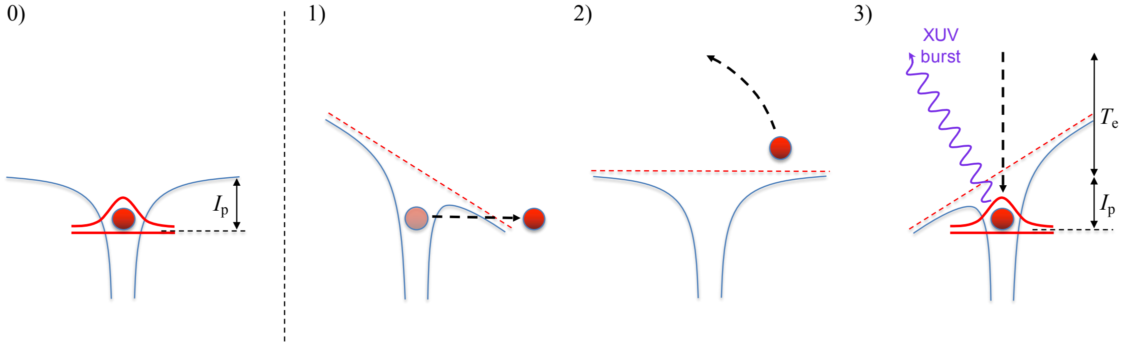

Figure 6.1: Three step model for HHG: 0) inital situation: bound electron (red) and atomic binding potential (blue), with the ionization energy I_p; **1)** Step 1: an eternal electric field is applied (red dashed line). This allows electron tunneling through the distorted potential barrier; **2)** Step 2: the electron, now free from the atomic potential, is accelerated away from the atom by the electric field; **3)** Step 3: the applied field sign inversion causes the electron to recollide with the parent ion, producing a high energy burst of radiation corresponding to the sum of the initial ionization energy (I_p) plus the kinetic energy gained in the continuum (T_e).

On top of this simplified picture, it is worth considering one more aspect useful to understand the ARIES approach, that is the spectral structure of the generated HHG. Figure 6.2 shows a typical HHG spectrum. Only the odd harmonic orders are present:

this is due to the generation process being anti-symmetric with respect to the driving field direction, as the light bursts are emitted at recombination events every half cycle of the driving field, causing the even harmonic order to destructively interfere. Considering the macroscopic structure of the spectrum, three distinct areas can be identified: a first one, which contains the low harmonic orders, belonging to the perturbative regime, where the intensity follows from the initial field; a second long and fairly flat area, known as the "plateau"; an abrupt cut-off where HHG quickly vanishes.

Following this model via classical mechanics means one can calculate the maximum energy of the recolliding electron, obtaining what is known as the cut-off law, stating the maximum energy of the generated radiation, such that

$$\omega_{\text{cut-off}} = \frac{I_p + 3.17U_p}{\hbar}, \tag{6.1}$$

where U_p is the ponderomotive energy of the electron oscillating in the laser field, equal to $U_p = E_0^2/(4\omega^2)$ (E_0 and ω identify the maximum amplitude and frequency of the driving field respectively) and I_p the ionization energy. In the case of a few-cycle driving pulse with zero CEP, a single dominating cycle of the electric field has a larger amplitude than the others, resulting in a single contribution to the cut-off energies. In this case, the cut-off region of the spectrum has a smooth and continuous profile. This feature will be exploited by ARIES to map the electric field of the pulse under measurement to the cut-off energy shift.

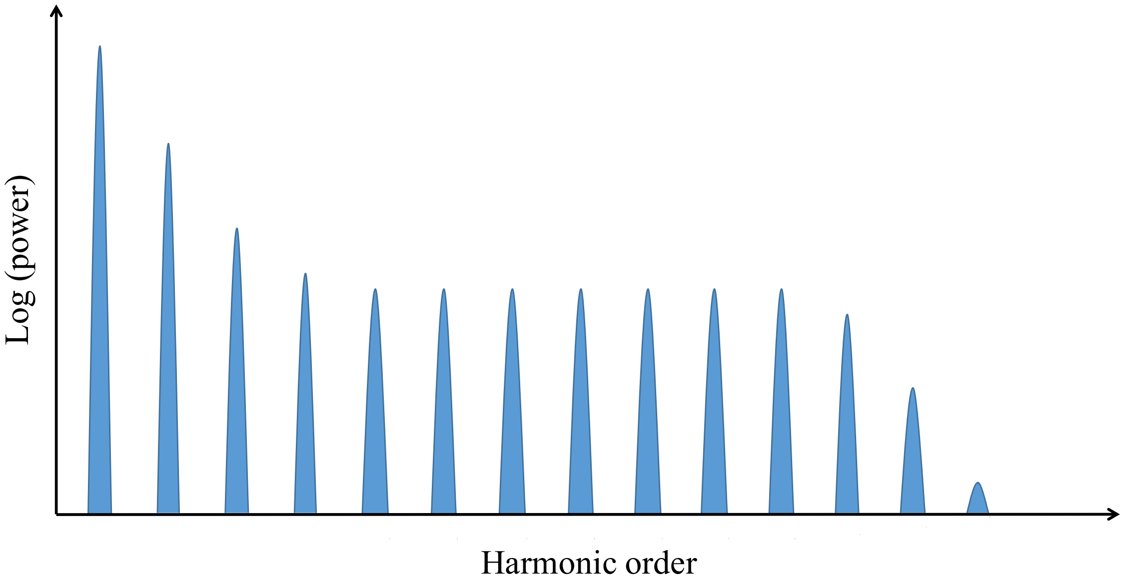

Figure 6.2: HHG spectral structure: three structures can be identified: a first area, with lower order harmonics, following the perturbative behaviour; a long plateau; a quick cut-off.

6.2 ARIES concept

The ARIES technique is based on mapping the TP electric field onto the generated HHG spectrum cut-off. This modulation shifts the energy cut-off of HHG from a driving few-cycle PP, making it an easy feature to track. The total field that drives the HHG is the sum of PP and TP:

$$E(t) = E_{\mathrm{PP}}(t) + E_{\mathrm{TP}}(t - \tau) \tag{6.2}$$

with PP being the intense few-cycle driving field, TP the weaker field (with a factor of $100 - 1000$ reduction in intensity), τ the pulse relative delay.

Figure 6.3 illustrates the ARIES concept: the few cycle, zero CEP cosine PP (6.3.a) generates a HHG spectrum with a continuous cut-off (grey area) (6.3.b); when the weak TP is added it can constructively (6.3.c) or destructively (6.3.e) add to the driving field, causing a shift in the generated HHG spectrum cut-off energy (6.3.d and 6.3.f). Tracking this shift while scanning the pulses' relative delay allows for the reconstruction of the TP waveform. Figure 6.3.f presents a more refined simulation of the ARIES trace (cut-off spectral area only) based on the strong-field approximation (SFA) approach, for a complex test waveform (superimposed black dotted line), showing its efficient mapping to the cut-off shift.

Following the semiclassical approach presented in the previous section, the photon energy generated at recollision is equal to the electron kinetic energy and ionization potential. Via purely classical mechanics one can calculate the electron velocity at recollision as

$$v = -\frac{e}{m}\int_{t_i}^{t_r} \left(E_{\text{pp}}(t) + E_{\text{tp}}(t-\tau)\right) dt = v_{\text{pp}} + v_{\text{tp}}, \tag{6.3}$$

where e and m are respectively the electron charge and mass, t_i and t_r the ionization and recollision times. Here the PP and TP fields as

$$E_{pp} = \hat{E}_{\text{pp}} \cos \omega_{\text{pp}} t, \tag{6.4}$$

$$E_{tp} = \hat{E}_{\text{tp}} \cos(\omega_{\text{tp}} t + \phi) \tag{6.5}$$

with $\hat{E}_{\text{pp}}$, $\hat{E}_{\text{tp}}$ and ω_{pp}, ω_{tp} respectively the amplitudes and frequencies of the PP and TP fields, from 6.3 one obtains $v_{\text{pp}} \propto \hat{E}_{\text{pp}}/\omega_{\text{pp}}$ and $v_{\text{tp}} \propto \hat{E}_{\text{tp}}/\omega_{\text{tp}}$.

Keeping in mind that $\hat{E}_{\text{tp}} \ll \hat{E}_{\text{pp}}$, the kinetic energy of the electron at recollision can then be written as

$$\epsilon = \frac{1}{2}m(v_{\text{pp}} + v_{\text{tp}})^2 \approx \frac{1}{2}mv_{\text{pp}}^2 + mv_{\text{pp}}v_{\text{tp}}, \tag{6.6}$$

neglecting the term $\frac{1}{2}mv_{\text{tp}}^2$.

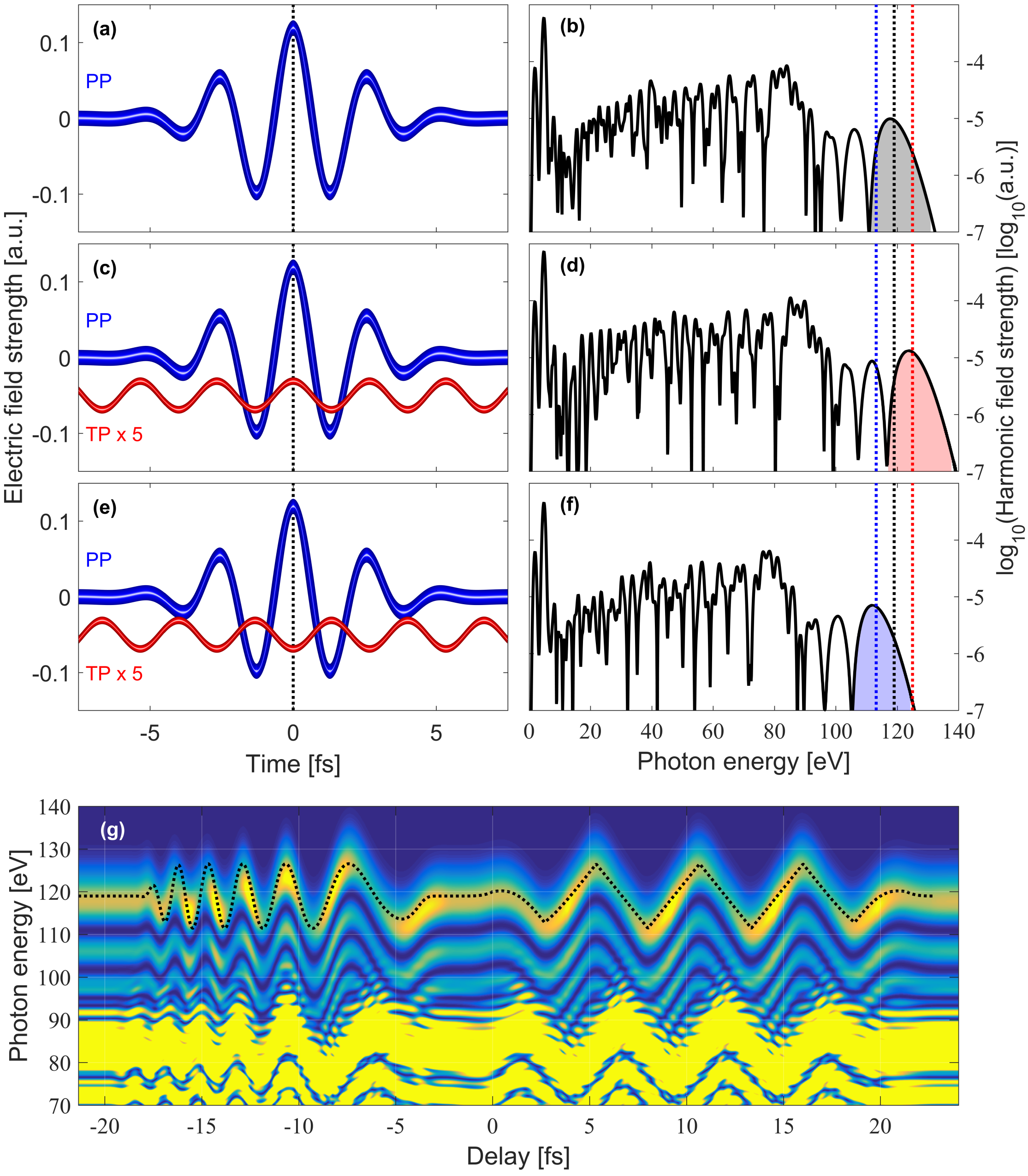

Figure 6.3: ARIES concept: for a 3.5 fs PP centred at 800 nm, peak intensity 5×10^{14} Wcm^{-2} (blue line) and CW test pulse centred at 800 nm, with relative intensity $I_tp/I_pp = 0.1\%$ (red line, magnified by a factor of 5 for clarity); **(a)** PP driving HHG and **(b)** generated spectrum, calculated via SFA; **(c)** constructive and **(e)** destructive interference, with resulting HHG spectra **(d)** and **(f)**. **(g)** Simulated ARIES for an artificially complex pulse, comprising a linear chirp section with a frequency sweep $\omega_{tp} = 0.05\omega_{pp} - 1.0\omega_{pp}$ and a saw-tooth section with frequency $\omega_{tp} = 0.5\omega_{pp}$ (superimposed dotted black line). The HHG spectrum is shown only for the area near the cut-off region.

By considering the PP only case, there is a trajectory with a certain ionization and recollision time for which the energy of the electron upon recombination with the parent ion is maximized. For these times $t_i = t_{\mathrm{i,pp}}^{(max)}$, $t_r = t_{\mathrm{r,pp}}^{(max)}$ and the corresponding energy $\epsilon_{\mathrm{pp}}^{(max)}$, we can identify a maximum cut-off emitted photon energy equal to $I_p + \epsilon_{\mathrm{pp}}^{(max)}$.

If we make the assumption that the weak TP modification to the ionization and recollision times is negligible, from 6.6 one obtains an expression for the maximum cut-off energy shift with respect to $\epsilon_{pp}^{(max)}$:

$$\Delta\epsilon_{max} \approx m v_{\mathrm{pp}} v_{\mathrm{tp}} \propto \frac{\hat{E}_{\mathrm{pp}}\hat{E}_{\mathrm{tp}}}{\omega_{\mathrm{pp}}\omega_{\mathrm{tp}}}. \tag{6.7}$$

A similar situation has been already considered theoretically in the literature, with a weak control pulse used to extend the cut-off region of a generated HHG spectrum[67]. These calculations, which simulate HHG by numerically integrating the time-dependent Schrödinger equation in the case of pulsed fields, proved that the linear relation 6.7 between the TP field and the cut-off shift is still valid beyond the semiclassical analysis used in this case. The ARIES technique utilizes equation 6.7 to reconstruct the TP waveform as a function of the pulses relative delays.

6.3 Experimental setup and measurements

The ARIES technique has been tested experimentally at Imperial College, London.

The setup is depicted in figure 6.4. The measurements have been performed with TP and PP both centred at 800 nm, derived from the same source. The laser system comprises a Ti:sapphire amplifier with CEP stabilization followed by a home-built HCF system, differentially pumped. A set of chirped mirrors and fused silica (FS) wedges are used to fine tune the pulse compression [45,68]. The output of the HCF system is measured to be 3.5 fs using a home-built SEA-F-SPIDER[1] [69], with energy 0.5 mJ at 1 kHz.

The TP and PP were obtained through a Mach-Zehnder interferometer, using broadband 10% reflection beam splitters. The TP is reflected from both, while the PP is transmitted. This gives an intensity ratio $\sim 1\%$ in between the TP and PP, with further adjustment achieved with an iris on the TP arm, reaching intensity ratios as low as $\sim 0.1\%$.

Two measurements were performed, aimed at reconstructing a CEP variation and a chirp variation inserted on the TP. To achieve this, a pair of thin FS wedges was inserted on the TP arm of the interferometer. The inserted dispersion was characterized by spectral interferometry. Delay between the two pulses was controlled by a motorized double stage system, comprising a DC motor stage (200 nm step size, 25 mm travel range) and a piezo stage (50 nm step size, 38 μm travel range) mounted on top of each other. This geometry (TP reflected with wedges, PP transmitted) allowed for balanced dispersion for a particular wedge setting, but could still be compensated for with the chirped mirrors.

Both pulses were sent to a vacuum chamber and focussed ($f = 75$ cm) into a Ne gas target, 1 mm long with density $\sim 10^{17}\,\mathrm{cm}^{-3}$. The generated HHG radiation was measured with a flat-field XUV spectrometer [70] incorporating a micro-channel plate (MCP) detector overimposed to a charge-coupled device (CCD) camera. The recorded spectra covered the $15-150$ eV range.

The first measurement we performed concerned the CEP variation on the TP, to prove that ARIES is effectively sensitive to the field waveform and not the pulse intensity. One of

---

[1] Spatially Encoded Arrangement Filter SPIDER

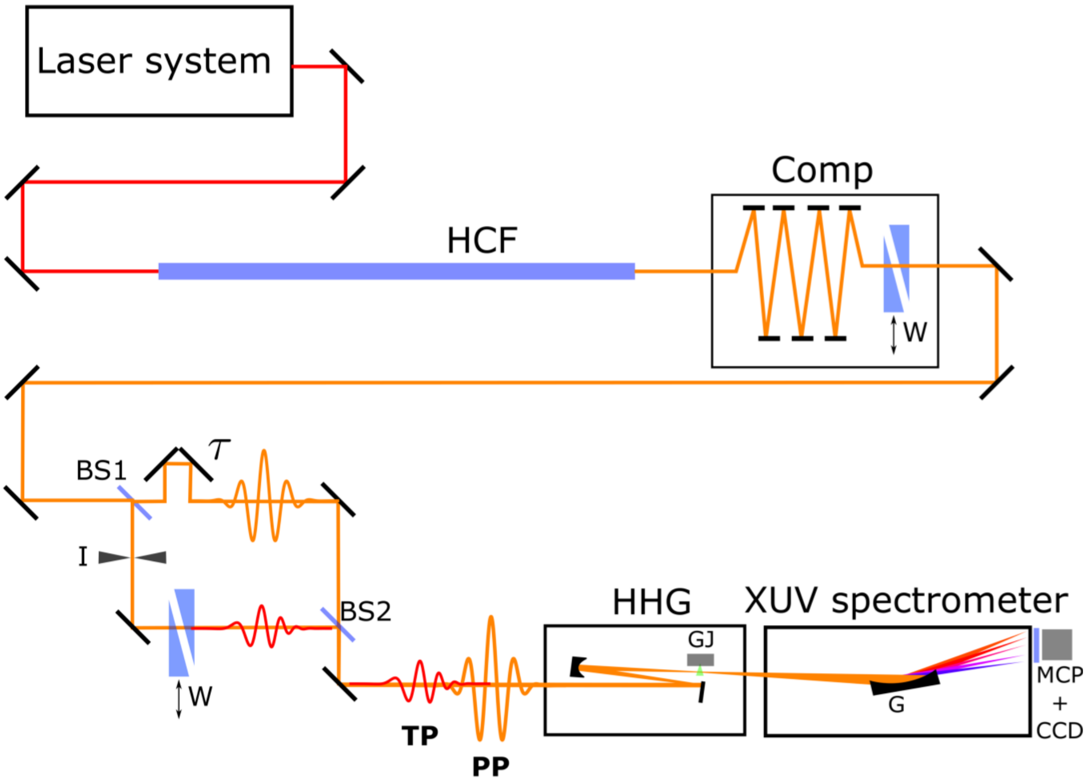

Figure 6.4: ARIES experimental setup: CEP stable, few-cycle pulses are obtained from an amplifier plus HCF system; the output compression (Comp) is tuned with a set of chirped mirrors and two FS wedges (W). A Mach-Zehnder interferometer is used to generate the TP and PP from the same pulse, with two broadband beamsplitters (BS1, BS2) with a reflection of 10%; an iris (I) is used to fine tune the TP/PP relative intensity in the $0.1 - 1\%$ range. Two FS wedges (W) are used to insert a CEP variation and additional dispersion on the TP. Both beams are sent collinearly to the HHG chamber and focussed on a Ne gas jet (GJ). The generated radiation is collected with a flat-field XUV spectrometer comprising a grating (G) and an MCP+CCD detector.

the wedges on the TP arm of the interferometer was moved to vary the CEP over a range of about 2π, while the PP was kept unchanged. Both the pulses had a duration of 3.5 fs. The intensities were approximatively 5×10^{14}Wcm^{-2} and 5×10^{11}Wcm^{-2} ($I_{tp}/I_{pp} \approx 0.1\%$) for the PP and TP, respectively.

Figure 6.5 presents the results obtained, showing the measured cut-off region of the HHG spectrum while scanning the pulses relative delay for various CEP values (a, c, e, g, i) and the reconstructed TP waveforms and pulse envelopes (blue and red lines respectively) (b, d, f, h, j). The black lines superimposed on the ARIES traces follow the centre of mass of the cut-off shift in the frequency domain: plotting the centre of mass shift in function of the PP-TP delay is the only analysis step necessary to extract the TP waveform from the data (this process will be referred to as "ARIES reconstruction" in the remaindeer of this chapter). The CEP variation is clearly evident and confirms the ability of ARIES to retrieve the TP waveform. In figure 6.5.k the retrieved CEP values as a function of the full wedge insertion range are plotted, with the green dots corresponding to the ARIES scans showed in figure 6.5.a, c, e, g and i. The retrieved value for the inverse slope fitted to the data (red line) is $48.5 \pm 0.7\,\mu$m$/2\pi$ rad, which has an excellent agreement with the theoretical value of $49.1\,\mu$m$/2\pi$ rad for FS.

The second measurement performed was focussed on retrieving a large time-bandwidth product TP, in this case a heavily chirped TP with a much longer duration than the one used in the CEP measurement. The wedges used in the previous measurement were used here to control the inserted chirp, scanning over a wider range of material, corresponding to ~ 1 mm of additional FS. The PP was again kept unchanged. Figure 6.6 illustrates the results of the ARIES reconstruction. Figure 6.6.a shows the retrieved waveforms for

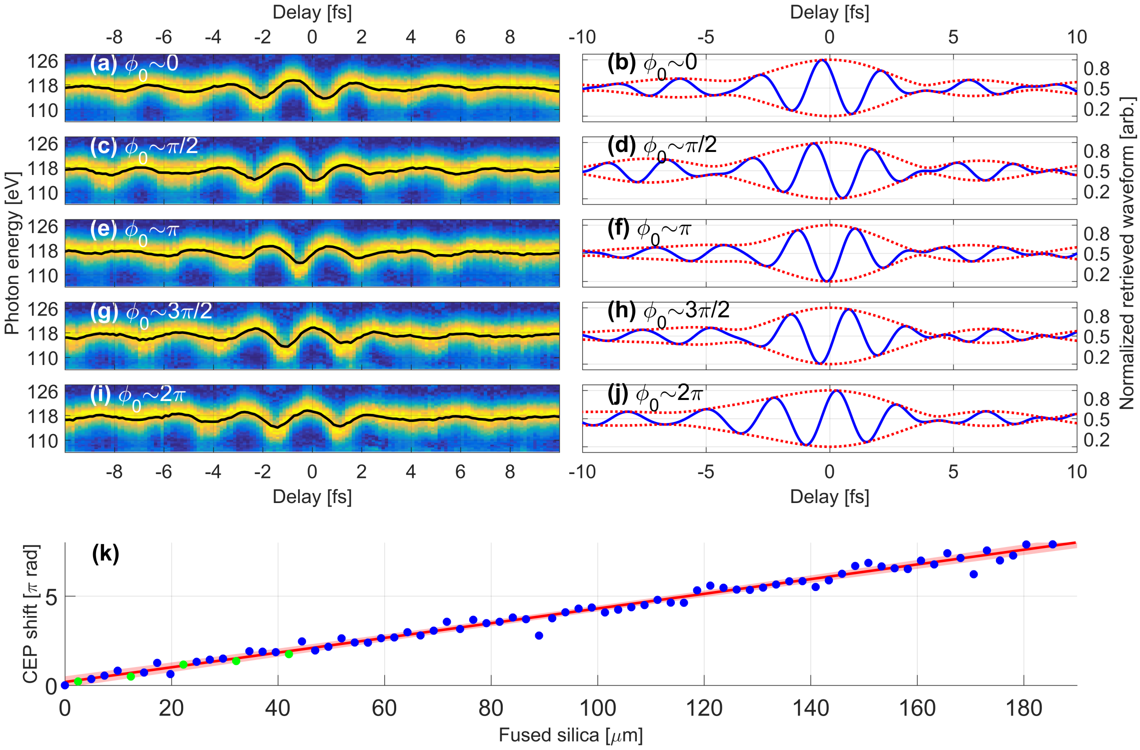

Figure 6.5: ARIES CEP reconstruction: measurements of few-cycle test pulse waveforms with varying CEP, demonstrating the field sensitivity of the ARIES technique. (a,c,e,g,i) present the cut-off part of the spectrum in function of the PP-TP delay, obtained for five different CEP values for the TP over a range of approximatively 2π. The superimposed black lines represent the centre of mass of the cut-off part of the spectrum as a function of delay. These are replotted as the retrieved fields in (b,d,f,h,j) respectively as thick blue curves with the pulse envelopes as dotted red lines. (k) shows the CEP values of the retrieved fields over a range of $\approx 8\pi$ as a function of the inserted FS. The solid line is a linear fit to the data, where the shaded region represents the 95% confidence interval. The green points represent the values of the CEP corresponding to the plots (b,d,f,h,j). The CEP was defined as the mean wavelength times the temporal difference between the peaks of the envelope and electric field.

different chirp values: (I-II) show a positive chirp, (III) is nearly compressed and (IV-VIII) show negative chirp. In figure 6.6.c the thin red curve is the average of the waveforms in (a), after numerical compensation of the known inserted dispersion. Figure 6.6.b shows directly the measured spectral phase after subtracting the FTL phase of the TP represented in (III), comparing the retrieved chirps (solid lines) with the theoretical ones (dashed lines) calculated for FS, showing an excellent agreement. Figure 6.6.d presents the retrieved spectrum from the ARIES measurement in comparison with an independent measurement performed with a broadband spectrometer.

We can conclude that ARIES can efficiently retrieve the waveform of the TP with a very good agreement with the expected theoretical values of inserted CEP and temporal dispersion.

6.4 A deeper look: numerical simulations

A deeper understanding of the ARIES technique can be achieved by refining its theoretical modelling beyond the simple semi-classical picture used so far. In particular, we expanded the theoretical approach to understand the role of the TP during HHG. Considering the HHG cut-off law $\omega_{\text{cut-off}} = (I_p + 3.17U_p)/\hbar$, a shift in $\omega_{\text{cut-off}}$ could take place by affecting: (i) the ionization energy I_p, (ii) the ponderomotive energy gained by the electron in the driving field U_p or (iii) a combination of both.

To understand this, we compared semi-classical approach with a quantum mechanical one, the SFA as presented by Lewenstein[71]. The main conceptual difference between the two approaches is the role of ionization: in the semi-classical case it is neglected and only

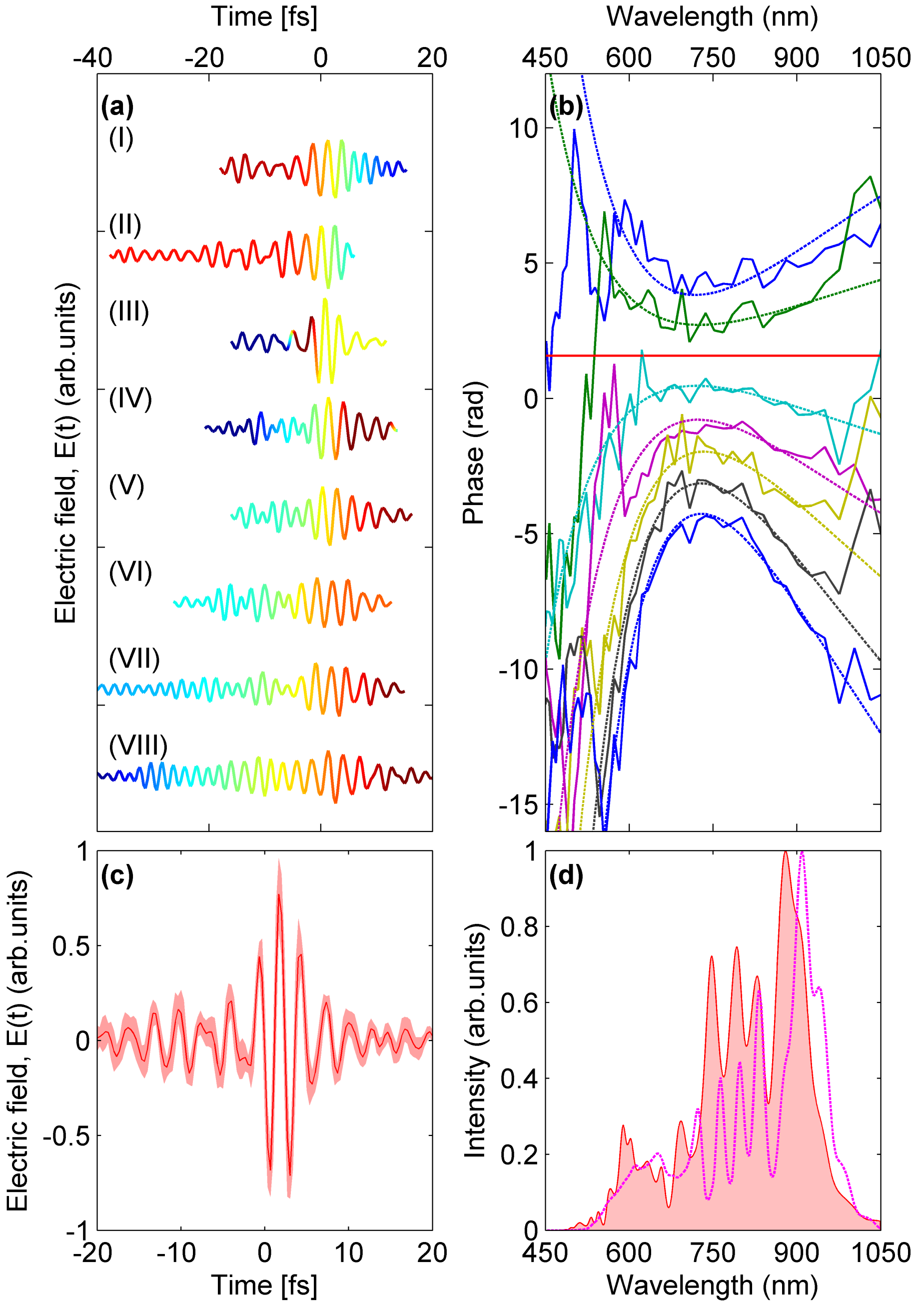

Figure 6.6: ARIES chirp measurement: (a) TP waveforms retrieved from ARIES measurements for different chirp values: (I-VIII) wedge insertion from +0.30 mm to −0.75 mm, 0.15 mm steps. **(b)** measured spectral phases after subtracting the FTL pulse phase from a(III) (solid lines) and calculated phase from material insertion (dashed lines), corresponding to (I-VIII). **(c)** plotted waveforms from (I-VIII) after numerical compensation of the known dispersion inserted. **(d)** Retrieved TP spectrum from ARIES (red-filled black line) compared with TP spectrum measured with a line spectrometer (blue dotted line).

the field effect on the already free electron is accounted for; in the quantum mechanical treatment the full HHG process is considered, hence ionization is included.

The two approaches have been employed in calculating the spectral response of the ARIES technique, i.e. the cut-off modulation amplitude response for different carrier frequencies of the TP. This response plays a fundamental role when dealing with broadband fields and diverse wavelength ranges. This is even more true when considering a Raman-based modulator with a large molecular energy shift like in the ARNIEMPM study presented in the previous chapters. The ARIES technique could be used to reconstruct probe pulses as well as study isolated Raman sidebands (like the pump pulse S1, centred at 1200 nm) ranging from the UV to the mid-IR (MIR) wavelength region, overcoming most of the problems commonly encountered by normal characterization methods (e.g. the need of a nonlinear medium, the inability to cover larg spectral gaps and other delineated at the beginning of this chapter).

In the semi-classical approach, one can approximate the maximum cut-off energy shift of the HHG, $\Delta\epsilon_{max} \approx m v_{\mathrm{pp}}^{(max)} v_{\mathrm{tp}}^{(max)}$, with $v_{\mathrm{pp}}^{(max)}$ and $v_{\mathrm{tp}}^{(max)}$ the maximum recollision velocities for PP and TP separately, obtaining

$$\Delta\epsilon_{max} \approx 2\epsilon_{pp}^{(max)} \frac{\hat{E}_{\mathrm{pp}}\hat{E}_{\mathrm{tp}}}{\omega_{\mathrm{pp}}\omega_{\mathrm{tp}}} \tag{6.8}$$

as a scaling relationship as a function of the TP frequency (ω_{pp}) for a fixed PP frequency (ω_{tp}); here $\hat{E}_{\mathrm{pp}}$ and $\hat{E}_{\mathrm{pp}}$ refer to the field amplitude of TP and PP respectively. This is the simplest approach we can utilize in the semi-classical scenario to calculate the spectral response of ARIES, taking into account the field contribution on the free electron trajectory only.

Conversely, the SFA [71] is a fully quantum mechanical approach and would take into account the ionization contribution. To explain this model of HHG, one can start from the time dependent Schrödinger equation (TDSE) for the atom-field interaction:

$$i\frac{\partial}{\partial t}\left|\Psi(\boldsymbol{r},t)\right\rangle = \left[\frac{\boldsymbol{p}^2}{2} + V(r) + \boldsymbol{\xi}(t)\cdot\mathbf{r}\right]\left|\Psi(\mathbf{r},t)\right\rangle, \tag{6.9}$$

where $V(\boldsymbol{r})$ is the atomic potential, $\boldsymbol{\xi}(t)$ the laser electric field and $\boldsymbol{p} = -i\nabla$ the momentum operator, all in atomic units ($\hbar = 1$, $e = 1$, $m_e = 1$, $a_0 = 1$) and the time is scaled by the central frequency, i.e. in units of radians. The ponderomotive energy is then $U_p = \xi_0/4\omega^2$.

Three assumptions are made: (i) only the ground states contributes to the HHG emission; (ii) depletion of the ground state is negligible; (iii) the actual strong-field approximation, which is pivotal in this approach: the electron in the field is considered a free particle, thus the atomic potential influence is neglected in the continuum. One can exactly write the expectation value of the dipole operator $x_{\hat{n}}(t) = \left\langle\Psi(x,t)\right| x_{\hat{n}}(t) \left|\Psi(x,t)\right\rangle$ as

$$\begin{aligned} x_{\hat{n}}(t) = i\int_0^t dt' \int_{\infty}^{\infty} d^3\boldsymbol{p}\hat{\boldsymbol{n}}\cdot\boldsymbol{d}^*(\boldsymbol{p}-\boldsymbol{A}(t)) \\ \times\, \boldsymbol{\xi}(t')\cdot\boldsymbol{d}(\boldsymbol{p}-\boldsymbol{A}(t'))e^{iS(\boldsymbol{p},t,t')} + \text{c.c.} \end{aligned}, \tag{6.10}$$

where

$$S(\boldsymbol{p},t,t') = \int_t^{\prime t} dt'' \left(\frac{[\boldsymbol{p}-\boldsymbol{A}(t'')]^2}{2} + I_p\right) \tag{6.11}$$

is the quasi-classical action and $\boldsymbol{d}(\boldsymbol{p}-\boldsymbol{A}(t')$ is the dipole matrix element. The canonical momentum as a function of the laser field vector potential $\boldsymbol{A}(t) = -\int_{-\infty}^{t} dt'\boldsymbol{\xi}(t')$ and the electron velocity $\boldsymbol{v}$ has been introduced as

$$\boldsymbol{p} = \boldsymbol{v} + \boldsymbol{A}(t) \tag{6.12}$$

and it represents phenomenologically the SFA condition, i.e. the electron momentum can change only in relation to the laser field, the atomic potential has no role.

Equation 6.10 can be intuitively interpreted in physical terms: (i) the scalar product $\boldsymbol{\xi}(t') \cdot \boldsymbol{d}(\boldsymbol{p} - \boldsymbol{A}(t'))$ represents the probability amplitude for an electron to transition to the continuum at time t' with a momentum $\boldsymbol{p}$; (ii) the electron is propagated in the continuum until time t, acquiring a phase equal to the quasi-classical action $S(\boldsymbol{p}, t, t')$, equation 6.11; (iii) the electron recombines with the parent ion at time t with a probability amplitude equal to $\boldsymbol{d}^*(\boldsymbol{p} - \boldsymbol{A}(t))$.

Via a stationary phase approximation (SPA), equation 6.10 can be simplified. For a $(t - t')$ of the order of one laser period only, the quasi-classical action variation is much greater than the other factors in 6.10. The stationary points $\Delta_{\boldsymbol{p}} S(\boldsymbol{p}, t, t') = 0$ of the semi-classical action become the dominant terms in the $\boldsymbol{p}$ integration. These correspond to momenta $\boldsymbol{p}$ for which the electron born at t' returns to the same position at t. In terms of physical interpretation this means that the dominant contribution to the HHG radiation emission is caused by the electrons that tunnel away from the nucleus and then recollide with it while oscillating in the applied electric field, confirming the validity of one basic aspect of the three step model. By substituting the stationary action obtained by applying the SPA, one can obtain the simplified version of 6.10 in the case of linearly polarized light

($\boldsymbol{\xi}(t) = E_x(t)$, $\boldsymbol{d}(\boldsymbol{p}) = d_x(\boldsymbol{p})$) and extending the integration to infinity as

$$x^{st}(t) = i \int_0^{\infty} d\tau \left(\frac{\pi}{\epsilon + i\tau/2} \right)^{3/2} d_x^*(p_x^{st}(t,\tau) - A_x(t)) \\ \times d_x(p_x^{st}(t,\tau) - A_x(t-\tau)) E_x(t-\tau) e^{-iS^{st}(t,\tau)} + \text{c.c.} \quad (6.13)$$

where the factor $[\pi/(\epsilon + i\tau/2)]^{3/2}$ is due to the SPA and represents the electron wave packet diffusion in three dimensions.

Equation 6.13 has been used to simulate the ARIES trace (i.e. the cut-off shift in function of the TP-PP delay) for a range of TP frequencies and retrieve the spectral response in function of the ARIES amplitude modulation. Figure 6.7 reports the result of ARIES traces in the SFA case, obtained by calculating equation 6.13 for the case of a continuous wave (CW) test pulse with different wavelengths. The left and central columns show the cut-off region of the simulated ARIES traces for TP wavelengths of 300 nm, 500 nm and 1500 nm (top to bottom), for an unmodified intensity (left) and normalized intensity (centre). The right column shows the retrieved field amplitude as a function of the TP frequency, with respect to TP and PP relative delay (top) and with respect to a delay scaled by a full TP field oscillation (bottom). It can be seen how the magnitude of the cut-off modulation decreases as the frequency of TP is increased.

This can be compared with the ARIES traces obtained in the same scenario with the semi-classical approach, solving 6.3 with $x(t_r, t_i) = 0$. Figure 6.8 presents the retrieved field amplitude as a function of a CW test pulse for various frequencies, for a pulse delay scaled by a full TP field oscillation, for the two models used: the SFA (left) and the semi-classical approach (right). The two figures show a very good agreement in terms of cut-off shift,

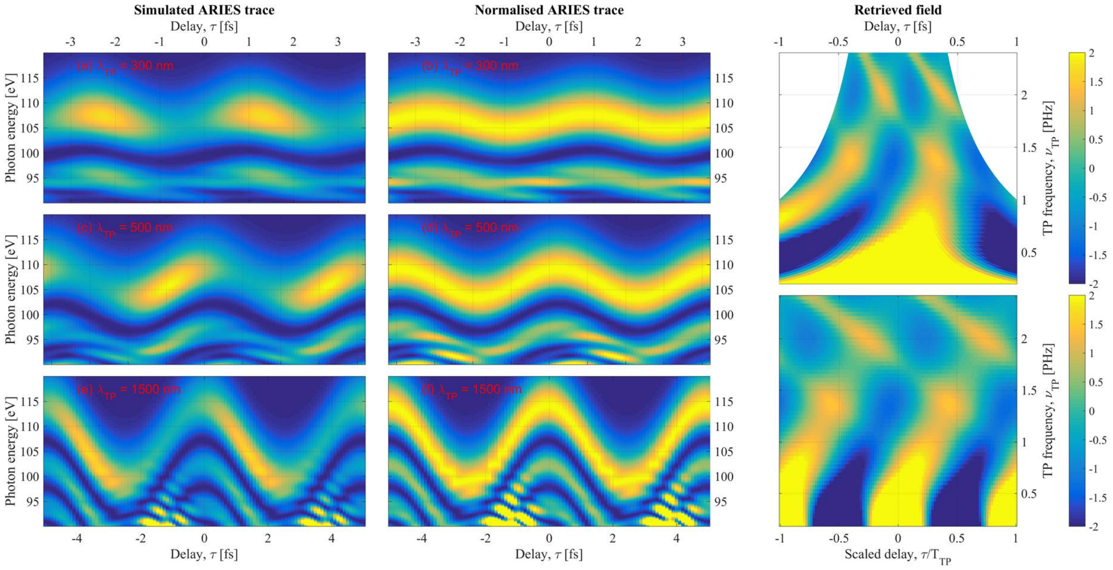

Figure 6.7: SFA simulation of ARIES: numerical simulation of the cut-off amplitude modulation for a CW TP with different frequencies. Left column: simulated ARIES traces, cut-off region only. Central column: simulated ARIES traces, cut-off region only, normalized in intensity. Right column: cut-off amplitude modulation as a function of TP CW frequency, plotted against the TP delay (top) and against the TP delay scaled by one full field oscillation (bottom).

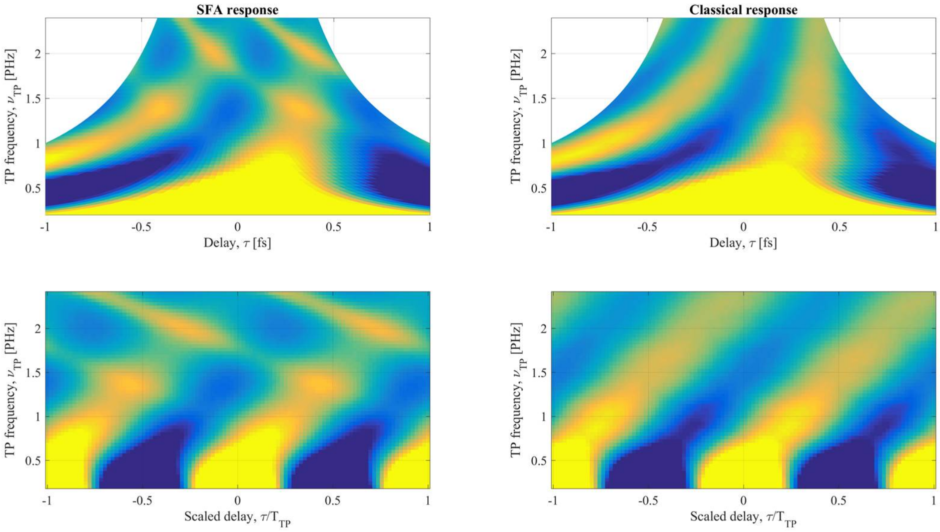

Figure 6.8: SFA VS semiclassical modulation: ARIES cut-off amplitude modulation as a funtion of the TP CW frequency. Left: SFA simulation. Right: semiclassical approximation. Plotted in scaled time with a full TP field oscillation.

with a difference in spectral intensity only. Considering that the fundamental difference between the SFA case and the semi-classical is the inclusion of the ionization contribution, one can conclude that the shift in the cut-off energy caused by the TP field takes place during the electron excursion in the continuum, free from the atomic potential influence. The semi-classical approach is then a valid model for the technique.

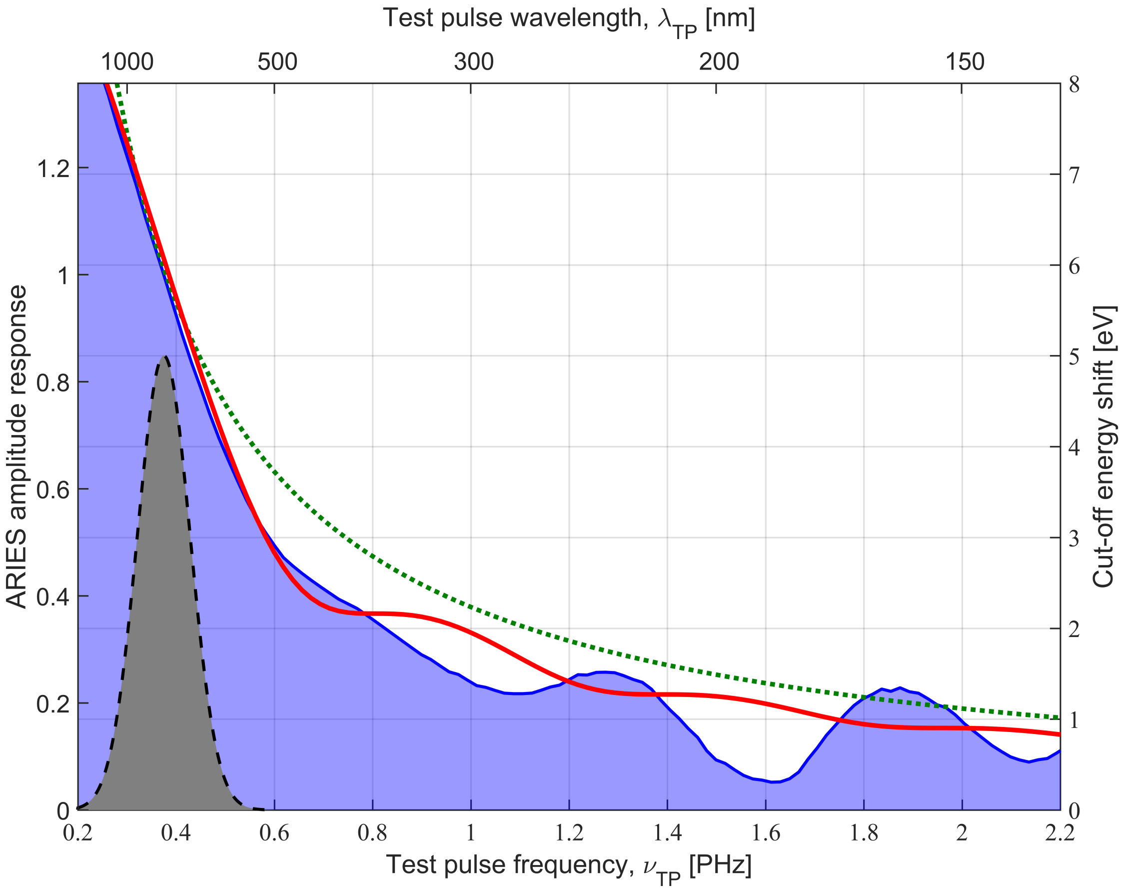

Figure 6.9: ARIES amplitude response: calculated for a 5×10^{14} Wcm^{-2}, 3.5 fs, 800 nm PP, with the TP substituted by a CW waveform with intensity $I_{tp}/I_{pp} = 0.1\%$, as a function of the TP frequency. **Dotted green curve:** classical approximation from equation 6.8. **Red curve:** numerical integration of classical equation of motion 6.3. **Filled blue curve:** calculated from SFA simulations.

Figure 6.9 compares the ARIES calculated spectral response for the SFA case (filled blue curve) with two implementations of the semi-lcassical approach: the simplest case, by using equation 6.8 (dotted green curve), or the integration of (6.3), with no assumption on the ionization and recollision times (solid red curve). The simplest case causes a slight overestimation of the spectral response, but there is an overall good agreement between the three cases. The calculated response function allows ARIES to measure a very large spectral range, up to four times the chosen fundamental frequency ω_0. We observe from figures 6.7 and 6.8 a linear shift in the timing of the reconstructed field as a function of the TP frequency. From this we know that the response function for ARIES is a complex quantity.

We concluded that the cut-off shift is due to the classical contribution to the electron acceleration in the driving field. However, ionization still plays a role, as can be seen in figures 6.7 and 6.8. The TP field instantaneously alters the ionization energy as a function of the pulse delay, resulting in an intensity modulation of the generated HHG radiation. This is visible in figure 6.7 (left column). The simulated SFA cut-off intensity oscillates at the same period of the cut-off modulation, thus following the TP waveform. The ionization contribution is also visible in figure 6.8 as an intensity modulation superimposed to the main frequency contribution, which is absent in the classical case. This intensity oscillation could be used to reconstruct the TP field by integrating the cut-off region at each time and tracking the intensity variation. Such a strategy could improve the resolution of the ARIES technique, as the ionization, which replaces the classical contribution as a temporal gate, has a much shorter response than the basic ARIES technique, which lies in the 1 fs regime. This potentially enables ARIES to characterize higher TP frequencies. However, the response is nonlinear and measuring intensity modulations is more susceptible to noise.

From the measurements presented in this chapter we can conclude that the ARIES technique is an effective method for the direct characterization of ultrashort pulses, being able to reconstruct arbitrary waveforms with attosecond resolution. The presented investigation suggests that the measurement is governed by the classical contribution given by the electron motion in the driving field during the HHG process. Numerical simulations indicate a wide range of applicability as the ARIES technique shows a good spectral response that ranges from the MIR to the deep UV regions of the electro-magnetic spectrum, covering up to 4 octaves of a typical Ti:Sa 800 nm emission.

Chapter 7

Conclusions

The main achievement of my work is the demonstration of vibrational phase modulation of broadband pulses in molecular hydrogen.

Using the ARNIEMPM technique, I impulsively prepared the material coherence via ISRS by using a few-cycle NIR pulse, then amplified the seeded coherence with a long, powerful pump pulse via SRS. This preparation was then used to phase modulate a broadband probe pulse.

An individual laser source was used to derive all three pulses required for the ARNIEMPM technique, considerably reducing the requirements in terms of experimental resources necessary for such an approach. A hollow-core waveguide was used to enhance the Raman gain of the process by increasing the interaction length by an order of magnitude.

I investigated experimentally the feasibility of using the ARNIEMPM approach with chirped seed and probe pulses with sufficient bandwidth to impulsively initiate and probe the dynamics, but with durations an order of magnitude longer than the molecular motion period.

In chapter 4 I studied the response of the material by monitoring sideband generation on the pump pulse, showing how they responded to pump power, seed delay and bandwidth. The pump depletion was used as a way to monitor the efficiency of the amplification step, as the Stokes sidebands were in an inaccessible spectral region for my detection scheme. The pump spectrum is depleted transferring energy to its sidebands: as the seed delay is varied, I show how the seed preceding the pump causes a response which endures after both pulses are gone, in agreement with the expected ns dephasing time of the vibrational coherence. For a seed whose bandwidth falls below the vibrational level splitting of H_2 the initiated dynamics are seen to vanish, confirming the impulsive aspect of the seeding step.

In chapter 5 I illustrate the modulating effect that such a prepared coherence has on a broadband probe pulse propagating through a material. Two probe choices are used, centred at 800 nm and 400 nm wavelength, respectively. The effect of the modulation is detected in a degenerate scheme which takes advantage of the chirped nature of the probe pulse. This creates a fringe pattern over the whole spectrum of the probe pulse, originating from interference between the chirped probe and the instantaneously generated discrete sidebands. The red probe shows a clear interference pattern which is dependent on the presence of the seed and the ordering of the three pulses, confirming it originates from the seeding. The fringe period is consistent with the experimentally measured chirp rate of the seed pulse and the vibrational energy shift of hydrogen, confirming the previously prepared material coherence is acting as a 125 THz phase modulator for the probe. In the blue case, there is an indication that the same is happening, but the limited energy of the blue probe and an unrefined detection scheme prevented me from obtaining clear results. Chromatic dispersion is also expected to play a role, especially in the blue case, limiting the Raman gain by restricting the interaction length, and hence a lower efficiency was to be expected.

In chapter 6 I presented a novel technique called ARIES for the direct characterization of arbitrary optical waveforms. I presented the results of the experimental work carried out at Imperial College, London, in collaboration with the local groups of Prof. Marangos and Prof. Tisch. The technique demonstrated the ability to retrieve the field of few-cycle pulses, for example by reconstructing a varying CEP imposed on the pulse by dispersive material. The technique relies on using HHG as a temporal gate, exploiting the classical trajectories of ionized electrons to track a test field superimposed onto the HHG driving field, as a function of their relative delay. The harmonic cut-off energy is modulated by an amount proportional to the applied test pulse field, allowing a straightforward reconstruction of the test waveform. A numerical investigation of the ARIES approach showed how the technique is based on the classical trajectories of ionized electrons, defining the temporal resolution to be $\sim 1\,\mathrm{fs}$. The ARIES spectral response was calculated for a wide range of frequencies, demonstrating the broad applicability of ARIES to high frequency test pulses in the UV regime.

7.0.1 Note on pulse experimental parameters

The model presented for ARNIEMPM in chapter 2 is based on certain assumptions that are not completely applicable in my experimental approach due to practical limitations in the dispersion management of broadband pulses and in the available energy. The impulsive condition on the seed is understood in terms of bandwidth, but a pulse which interacts with a molecular medium exhibits a second order spectral phase component. In my case this results in a chirped pulse duration approximatively ten times longer than the vibrational period.

Another assumption regards the pump pulse, which is considered undepleted throughout the amplification process. In chapter 4 I showed how the pump spectrum undergoes a certain degree of depletion and how I actually used this as an indication of the amplification efficiency as a function of several parameters. The probe pulse (similarly to the seed) is also chirped to a duration of $\sim 150\,\mathrm{fs}$, which prevents any considerable broadening from occurring in the impulsive regime.

The work presented in this thesis is an experimental investigation into the feasibility of using vibrating hydrogen as a phase modulator for UV broadband pulses. A theoretical refinement of the ARNIEMPM model to account for my experimental parameters is beyond the scope of this thesis. My investigation (see chapters 4 and 5) has shown how the seed pulse is still fulfilling its role, together with the pump, to prepare a vibrational coherence in the medium that can be exploited to modulate the probe. The temporal chirp on the probe became a resource that I used to my advantage to make it simpler to detect any signature of phase modulation driven by vibrating hydrogen.

7.1 Future developments

Future developments are mainly focussed on improving the experimental setup in several aspects.

The detection scheme relied on a purely spectral measurement. The limited time-frame available for this experiment prevented the implementation of more complex detection schemes. The spectral approach provided proof of impulsive molecular phase modulation on the probe, but this is not the ideal approach for a detailed investigation as it yelds no information for example on the spectral phase and thus the temporal structure. An improved approach would involve temporally gating the modulated probe and isolating it from the rest of the pulse train, reducing the detrimental effects of the pump sidebands background, which proved particularly disturbing in my work. A subsequent full reconstruction of the modulated probe, via ARIES or a suitably tailored version of the SPIDER technique would enable the complete extraction the information regarding the molecular dynamics and their effect on the probe.

The choice of using a single laser to generate all three pulses is certainly advantageous in terms of resources, but created detection problems as the pulse spectra overlaps with each other or their Raman sidebands. The ARNIEMPM technique does not require any phase relation between the seed and pump pulses, as already demonstrated by Bustard[19]. The latest developments in fibre laser technology provide much more powerful and rather inexpensive pump lasers with picosecond duration that could be perfectly suited to the task. The increased energy and the use of a short wavelength would strongly increase the Raman gain and thus the efficiency of the process.

The waveguide proved to be a winning strategy, by increasing the efficiency of the process, but its contribution is limited by phase-matching difficulties. A waveguide itself can mitigate the effect of dispersion by adding a plasma-like term in the phase mismatch calculation, but the one used here has a core diameter that is too large to have any meaningful effect. A possible way forward is the use of hollow-core photonic crystal fibres or other microstructured waveguide to compensate for the dispersion with their small core dimensions.

Overall, I am convinced that vibrating hydrogen is an accessible tool that can be used to phase modulate broadband pulses over dramatically large bandwidths. By exploiting the latest developments in laser technology, it would be possible to use it to generate isolated, bright UV few-cycle pulses.

Bibliography

[1] T. H. Maiman. Stimulated Optical Radiation in Ruby. *Nature*, 187(4736):493–494, August 1960.

[2] Willis E. Lamb. Theory of an Optical Maser. *Physical Review*, 134(6A):A1429–A1450, June 1964.

[3] L. E. Hargrove, R. L. Fork, and M. A. Pollack. LOCKING OF HeNe LASER MODES INDUCED BY SYNCHRONOUS INTRACAVITY MODULATION. *Applied Physics Letters*, 5(1):4–5, July 1964.

[4] A. H. Zewail. Laser Femtochemistry. *Science*, 242(4886):1645–1653, December 1988.

[5] M. Nisoli, S. De Silvestri, and O. Svelto. Generation of high energy 10 fs pulses by a new pulse compression technique. *Applied Physics Letters*, 68(20):2793–2795, May 1996.

[6] M. Nisoli, S. De Silvestri, O. Svelto, R. Szipöcs, K. Ferencz, Ch Spielmann, S. Sartania, and F. Krausz. Compression of high-energy laser pulses below 5 fs. *Optics Letters*, 22(8):522–524, April 1997.

[7] A Mysyrowicz, A Couairon, and U Keller. Self-compression of optical laser pulses by filamentation. *New Journal of Physics*, 10(2):025023, 2008.

[8] Charles G. Durfee, Sterling Backus, Henry C. Kapteyn, and Margaret M. Murnane. Intense 8-fs pulse generation in the deep ultraviolet. *Optics Letters*, 24(10):697–699, May 1999.

[9] Kun Zhao, Qi Zhang, Michael Chini, Yi Wu, Xiaowei Wang, and Zenghu Chang. Tailoring a 67 attosecond pulse through advantageous phase-mismatch. *Optics Letters*, 37(18):3891–3893, September 2012.

[10] Thomas Brabec and Ferenc Krausz. Intense few-cycle laser fields: Frontiers of nonlinear optics. *Reviews of Modern Physics*, 72(2):545–591, April 2000.

[11] Ferenc Krausz and Misha Ivanov. Attosecond physics. *Reviews of Modern Physics*, 81(1):163–234, February 2009.

[12] P. B. Corkum and Ferenc Krausz. Attosecond science. *Nat Phys*, 3(6):381–387, June 2007.

[13] M. Uiberacker, Th Uphues, M. Schultze, A. J. Verhoef, V. Yakovlev, M. F. Kling, J. Rauschenberger, N. M. Kabachnik, H. Schroder, M. Lezius, K. L. Kompa, H. G. Muller, M. J. J. Vrakking, S. Hendel, U. Kleineberg, U. Heinzmann, M. Drescher, and F. Krausz. Attosecond real-time observation of electron tunnelling in atoms. *Nature*, 446(7136):627–632, April 2007.

[14] S. Baker, I. A. Walmsley, J. W. G. Tisch, and J. P. Marangos. Femtosecond to attosecond light pulses from a molecular modulator. *Nature Photonics*, 5(11):664–671, November 2011.

[15] C. V. Raman and K. S. Krishnan. A new type of secondary radiation. *Nature*, 121:501–502, March 1928.

[16] E. J. Woodbury and W. K. Ng. Ruby operation in the Near IR. *Proc. Inst. Radio Eng.*, 50:2367+, 1962.

[17] N. Zhavoronkov and G. Korn. Generation of Single Intense Short Optical Pulses by Ultrafast Molecular Phase Modulation. *Physical Review Letters*, 88(20), May 2002.

[18] Wei-Jan Chen, Zhi-Ming Hsieh, Shu W. Huang, Hao-Yu Su, Chien-Jen Lai, Tsung-Ta Tang, Chuan-Hsien Lin, Chao-Kuei Lee, Ru-Pin Pan, Ci-Ling Pan, and A. H. Kung. Sub-Single-Cycle Optical Pulse Train with Constant Carrier Envelope Phase. *Physical Review Letters*, 100(16):163906+, April 2008.

[19] Philip J. Bustard, Benjamin J. Sussman, and Ian A. Walmsley. Amplification of Impulsively Excited Molecular Rotational Coherence. *Physical Review Letters*, 104(19):193902+, May 2010.

[20] N. Bloembergen. The Stimulated Raman Effect. *American Journal of Physics*, 35:989–1023, November 1967.

[21] C. V. Raman. A new radiation. *Indian Journal of Physics*, 2:387–398, 1928.

[22] R. Bartels, S. Backus, E. Zeek, L. Misoguti, G. Vdovin, I. P. Christov, M. M. Murnane, and H. C. Kapteyn. Shaped-pulse optimization of coherent emission of high-harmonic soft X-rays. *Nature*, 406(6792):164–166, July 2000.

[23] A. Paul, R. A. Bartels, R. Tobey, H. Green, S. Weiman, I. P. Christov, M. M. Murnane, H. C. Kapteyn, and S. Backus. Quasi-phase-matched generation of coherent extreme-ultraviolet light. *Nature*, 421(6918):51–54, January 2003.

[24] Matt Landreman, Kevin O'Keeffe, Tom Robinson, Matt Zepf, Brendan Dromey, and Simon M. Hooker. Comparison of parallel and perpendicular polarized counterpropagating light for suppressing high harmonic generation. *Journal of the Optical Society of America B*, 24(9):2421–2427, September 2007.

[25] L. E. Chipperfield, J. S. Robinson, J. W. G. Tisch, and J. P. Marangos. Ideal Waveform to Generate the Maximum Possible Electron Recollision Energy for Any Given Oscillation Period. *Physical Review Letters*, 102(6):063003+, February 2009.

[26] H. S. Chan, Z. M. Hsieh, W. H. Liang, A. H. Kung, C. K. Lee, C. J. Lai, R. P. Pan, and L. H. Peng. Synthesis and Measurement of Ultrafast Waveforms from Five Discrete Optical Harmonics. *Science*, 331(6021):1165–1168, January 2011.

[27] F. T. Arecchi and R. Bonifacio. Theory of optical maser amplifiers. *J. Quantum Electron.*, 4(1):169 – 178, 1965.

[28] R. W. Boyd. *Nonlinear Optics*. Academic Press, 1992.

[29] Berge Tatian. Fitting refractive-index data with the Sellmeier dispersion formula. *Applied Optics*, 23(24):4477+, December 1984.

[30] M. Abramowitz and I. A. Stegun. *Handbook of Mathematical Functions with Formulas, Graphs, and Mathematical Tables.* Dover, 1964.

[31] P. J. Bustard. *Phase-stable Amplication of Coherent Molecular Rotational Dynamics for Molecular Phase Modulation.* PhD thesis, University of Oxford, 2010.

[32] M. Raymer and I. A. Walmsley. Progress in Optics. volume 28, pages 121+, 1990.

[33] M. G. Raymer and J. Mostowski. Stimulated Raman scattering: Unified treatment of spontaneous initiation and spatial propagation. *Physical Review A*, 24(4):1980–1993, October 1981.

[34] M. Belsley, D. T. Smithey, K. Wedding, and M. G. Raymer. Observation of extreme sensitivity to induced molecular coherence in stimulated Raman scattering. *Physical Review A*, 48(2):1514–1525, August 1993.

[35] M. O. Scully and M. S. Zubairy. *Quantum Optics.* Cambridge University Press, 1997.

[36] Benjamin J. Sussman, Jonathan G. Underwood, R. Lausten, Misha Y. Ivanov, and Albert Stolow. Quantum control via the dynamic Stark effect: Application to switched rotational wave packets and molecular axis alignment. *Physical Review A*, 73(5):053403+, May 2006.

[37] Henrik Stapelfeldt and Tamar Seideman. Colloquium : Aligning molecules with strong laser pulses. *Reviews of Modern Physics*, 75(2):543–557, April 2003.

[38] A. V. Sokolov, D. R. Walker, D. D. Yavuz, G. Y. Yin, and S. E. Harris. Raman Generation by Phased and Antiphased Molecular States. *Physical Review Letters*, 85(3):562–565, July 2000.

[39] A. V. Sokolov and S. E. Harris. Ultrashort pulse generation by molecular modulation. *Journal of Optics B: Quantum and Semiclassical Optics*, 5(1):R1–R26, February 2003.

[40] M. G. Raymer, I. A. Walmsley, J. Mostowski, and B. Sobolewska. Quantum theory of spatial and temporal coherence properties of stimulated Raman scattering. *Physical Review A*, 32(1):332–344, July 1985.

[41] G. B. Arfken and H. J. Weber. *Mathematical Methods for Physicists.* Academic Press; 6th edition, 2005.

[42] William K. Bischel and Mark J. Dyer. Wavelength dependence of the absolute Raman gain coefficient for the Q (1) transition in H_2. *Journal of the Optical Society of America B*, 3(5):677–682, May 1986.

[43] L. S. Meng. *Continuous-wave Raman Laser in H_2: Semiclassical Theory and Diode-pumping Experiments.* PhD thesis, Montana State University, 2002.

[44] Sandro De Silvestri. Few-Cycle Pulses by External Compression. In Franz X. Kärtner, editor, *Few-Cycle Laser Pulse Generation and Its Applications*, chapter 2. Springer, 2004.

[45] Tobias Witting, Felix Frank, Christopher A. Arrell, William A. Okell, Jonathan P. Marangos, and John W. G. Tisch. Characterization of high-intensity sub-4-fs laser pulses using spatially encoded spectral shearing interferometry. *Optics Letters*, 36(9):1680–1682, April 2011.

[46] Minorsky. Directional stability of automatically steered bodies. *Journal of the American Society for Naval Engineers*, 34(2):280–309, May 1922.

[47] Chris Iaconis and Ian A. Walmsley. Self-referencing spectral interferometry for measuring ultrashort optical pulses. *Quantum Electronics, IEEE Journal of*, 35(4):501–509, April 1999.

[48] Adam S. Wyatt, Ian A. Walmsley, Gero Stibenz, and Günter Steinmeyer. Sub-10 fs pulse characterization using spatially encoded arrangement for spectral phase interferometry for direct electric field reconstruction. *Optics Letters*, 31(12):1914+, 2006.

[49] A. Nazarkin, G. Korn, M. Wittmann, and T. Elsaesser. Generation of Multiple Phase-Locked Stokes and Anti-Stokes Components in an Impulsively Excited Raman Medium. *Physical Review Letters*, 83(13):2560–2563, September 1999.

[50] A. Yariv. *Optical Electronics in Modern Communications.* Oxford University Press, 1997.

[51] A. Nazarkin, G. Korn, M. Wittmann, and T. Elsaesser. Group-velocity-matched interactions in hollow waveguides: Enhanced high-order raman scattering by impulsively excited molecular vibrations. *Phys. Rev. A*, 65:041802, Apr 2002.

[52] Ian A. Walmsley and Christophe Dorrer. Characterization of ultrashort electromagnetic pulses. *Advances in Optics and Photonics*, 1(2):308–437, April 2009.

[53] C. Iaconis and I. A. Walmsley. Spectral phase interferometry for direct electric-field reconstruction of ultrashort optical pulses. *Optics Letters*, 23(10):792+, May 1998.

[54] Xun Gu, Lin Xu, Mark Kimmel, Erik Zeek, Patrick O'Shea, Aparna P. Shreenath, Rick Trebino, and Robert S. Windeler. Frequency-resolved optical gating and single-shot spectral measurements reveal fine structure in microstructure-fiber continuum. *Optics letters*, 27(13):1174–1176, July 2002.

[55] R. Trebino. *Frequency-Resolved Optical Gating: The Measurement of Ultrashort Laser Pulses.* Kluwer Academic, 2002.

[56] Mitsuo Takeda, Hideki Ina, and Seiji Kobayashi. Fourier-transform method of fringe-pattern analysis for computer-based topography and interferometry. *Journal of the Optical Society of America*, 72(1):156–160, January 1982.

[57] Daniel J. Kane, G. Rodriguez, A. J. Taylor, and Tracy S. Clement. Simultaneous measurement of two ultrashort laser pulses from a single spectrogram in a single shot. *Journal of the Optical Society of America B*, 14(4):935+, April 1997.

[58] Daniel K. Kane. Recent progress toward real-time measurement of ultrashort laser pulses. *Quantum Electronics, IEEE Journal of*, 35(4):421–431, April 1999.

[59] A. Wirth, M. T. Hassan, I. Grguras, J. Gagnon, A. Moulet, T. T. Luu, S. Pabst, R. Santra, Z. A. Alahmed, A. M. Azzeer, V. S. Yakovlev, V. Pervak, F. Krausz, and E. Goulielmakis. Synthesized Light Transients. *Science*, 334(6053):195–200, September 2011.

[60] Cristian Manzoni, Oliver D. Mücke, Giovanni Cirmi, Shaobo Fang, Jeffrey Moses, Shu-Wei Huang, Kyung-Han Hong, Giulio Cerullo, and Franz X. Kärtner. Coherent pulse synthesis: towards sub-cycle optical waveforms. *Laser & Photonics Reviews*, 9(2):129–171, March 2015.

[61] J. Itatani, F. Quéré, G. L. Yudin, Ivanov, F. Krausz, and P. B. Corkum. Attosecond Streak Camera. *Physical Review Letters*, 88(17):173903+, April 2002.

[62] Y. Mairesse and F. Quéré. Frequency-resolved optical gating for complete reconstruction of attosecond bursts. *Physical Review A*, 71(1):011401+, January 2005.

[63] E. Goulielmakis. Direct Measurement of Light Waves. *Science*, 305(5688):1267–1269, August 2004.

[64] Kyung T. Kim, Chunmei Zhang, Andrew D. Shiner, Bruno E. Schmidt, Francois Legare, D. M. Villeneuve, and P. B. Corkum. Petahertz optical oscilloscope. *Nature Photonics*, 7(12):958–962, November 2013.

[65] M. Wittmann, A. Nazarkin, and G. Korn. fs-Pulse Synthesis Using Phase Modulation by Impulsively Excited Molecular Vibrations. *Physical Review Letters*, 84(24):5508–5511, June 2000.

[66] P. B. Corkum. Plasma perspective on strong field multiphoton ionization. *Physical Review Letters*, 71(13):1994–1997, September 1993.

[67] Thomas Pfeifer, Lukas Gallmann, Mark J. Abel, Phillip M. Nagel, Daniel M. Neumark, and Stephen R. Leone. Heterodyne Mixing of Laser Fields for Temporal Gating of High-Order Harmonic Generation. *Physical Review Letters*, 97(16), October 2006.

[68] F. Frank, C. Arrell, T. Witting, W. A. Okell, J. McKenna, J. S. Robinson, C. A. Haworth, D. Austin, H. Teng, I. A. Walmsley, J. P. Marangos, and J. W. G. Tisch. Invited Review Article: Technology for Attosecond Science. *Review of Scientific Instruments*, 83(7):071101+, July 2012.

[69] Tobias Witting, Dane R. Austin, and Ian A. Walmsley. Improved ancilla preparation in spectral shearing interferometry for accurate ultrafast pulse characterization. *Optics Letters*, 34(7):881–883, March 2009.

[70] Noboru Nakano, Hiroto Kuroda, Toshiaki Kita, and Tatsuo Harada. Development of a flat-field grazing-incidence XUV spectrometer and its application in picosecond XUV spectroscopy. *Applied Optics*, 23(14):2386–2392, July 1984.

[71] M. Lewenstein, Ph Balcou, Ivanov, Anne L'Huillier, and P. B. Corkum. Theory of high-harmonic generation by low-frequency laser fields. *Physical Review A*, 49(3):2117–2132, March 1994.